Phil. Trans. R. Soc. Lond. A **329**, 415–502 (1989) [415]
Printed in Great Britain

GEOMAGNETIC SECULAR VARIATION

By J. BLOXHAM[1], D. GUBBINS[2] AND A. JACKSON[3]

[1] *Department of Earth and Planetary Sciences, Harvard University,* 20 *Oxford Street, Cambridge, Massachusetts* 02138, *U.S.A.*

[2] *Department of Earth Sciences, University of Leeds, Leeds LS*6 9*JT, U.K.*

[3] *Bullard Laboratories, University of Cambridge, Madingley Road, Cambridge CB*3 0*EZ, U.K.*

(*Communicated by D. P. McKenzie, F.R.S. – Received* 10 *June* 1988 – *Revised* 20 *February* 1989)

[Plates 1–4]

CONTENTS

We analyse over 175000 magnetic observations from an interval spanning 1695–1980 to produce a sequence of maps of the magnetic field at the core–mantle boundary; we find that even the earlier data enable us to determine reliable maps. We produce these maps at approximately 60-year intervals through the eighteenth and nineteenth centuries, and at 10-year intervals in the twentieth century. This span of maps is long enough to render straightforward the distinction between static and drifting features in the field: we observe that some features show no sign whatsoever of drift over the entire 285-year time interval, although others drift westwards. In particular, we observe that the secular variation is very low beneath the Pacific ocean, but beneath southern Africa and the South Atlantic ocean we observe rapid secular variation. We interpret the morphology of the static field in terms of a simple model of the dynamo, and conjecture that interactions between the core and the mantle are an important element of the process. As part of the static field we identify four main concentrations of flux, two in each hemisphere, at high latitudes: these features largely account for the Earth's axial dipole moment. We find unequivocal evidence that magnetic flux has not remained frozen over the time span of our models; much of the diffusive behaviour that we identify is associated with the formation of a pair of flux spots (a 'core spot') beneath southern Africa, early in this century. Nevertheless, we are able to construct maps that satisfy a set of necessary conditions for frozen-flux, and use these maps to construct maps of the core surface fluid flow, based on the steady flow hypothesis. Although we find no strong evidence against the steady flow hypothesis, we do find some grounds on which to doubt the validity of the flow maps.

1. INTRODUCTION

1.1. *Secular variation*

Our concern in this paper is the secular variation of the Earth's magnetic field, by which we mean its slow change with time over periods of years to centuries. We use the term secular variation to apply to the change of the entire field $\boldsymbol{B}$, not some particular part of it such as the non-dipole component. Secular variation originates in the core of the Earth; any external sources causing long-term changes in the field will contribute to the observed field variations but not to our definition of secular change.

Our ultimate goal is to elucidate the motions of the fluid in the core that, to a large extent, cause the secular variation, and thence to understand its dynamics. Although secular variation takes place on a timescale short compared with that of geomagnetic polarity reversals or the regeneration of the field by the dynamo process, there is every hope that these processes are linked and that an understanding of secular change will shed light on the others. It is instructive to consider an analogy with meteorology. Typical velocities in the atmosphere are 10 m s^{-1}, whereas those in the core are $5 \times 10^{-4} \text{ m s}^{-1}$: in terms of timescales, one day in the atmosphere is equivalent to roughly 50 years in the core. Previous studies of the secular variation of the field at the core–mantle boundary (also referred to as the CMB) have used, at most, 20 years of data, equivalent to attempting to understand changes in the weather with only 10 hours of data. In this paper we use longer timespans of data, giving the equivalent of almost a week of meteorological observations.

To this end we have mapped $\boldsymbol{B}$ at the core–mantle boundary as far back in time as historical magnetic measurements allow. The oldest measurements we have used date from A.D. 1695. We plot $\boldsymbol{B}$ at discrete epochs, times that are determined by availability of data. The field models are based on wholly independent data-sets; traits running through several models may therefore be trusted as real features of the field. We would not be so sure of features appearing in field models that averaged data from a wide range of times. A method for solving for a continuously varying $\boldsymbol{B}(t)$ has been devised by Bloxham (1987) and will ultimately be applied to the entire data-set described in this paper to produce a field and secular variation model for use in determining core motions (see Bloxham & Jackson 1989).

The maps in §4 are of core field rather than secular variation. Changes in the core field can be followed by comparing maps at different epochs. Maps of secular change are too noisy for easy interpretation. Appealing again to the analogy with meteorology, the weather forecaster plots maps of barometric pressure rather than its rate of change because the time derivative is inaccurate; we plot field rather than secular change for the same reason.

Often it is remarked that secular change is determined solely at observatories because ordinary survey measurements are influenced by the short-wavelength field of the magnetized crust which differs by 200–300 nT even between nearby sites (see, for example, Malin *et al.* 1983), as well as by external fields. We have not found this to be the case because satellite data are not much affected by short wavelengths, survey measurements in general are so much more numerous that observatory annual means that they contribute more, overall, to the field models despite the lower weight given to each individual reading, and during the very long time span of the present study (1695–1980) the secular change is sufficiently great to be constrained even by inaccurate survey data. Observatory annual means may well contribute proportionately more to models of short-term secular variation such as those studied by Malin *et al.* (1983).

1.2. *Main field modelling*

We follow the usual geomagnetic notation for representing the Earth's field, which in this context is called the 'main field'. A review of recent work in main field modelling is given by Langel (1987).

The volume outside the Earth's surface is assumed to be an electrical insulator so the magnetic field can be expressed as the gradient of a potential,

$$\boldsymbol{B} = -\nabla V, \tag{1.1}$$

where

$$\nabla^2 V = 0, \tag{1.2}$$

and

$$V \sim r^{-2} \quad \text{as} \quad r \rightarrow \infty, \tag{1.3}$$

because there are no sources at infinity. V can be expanded in a spherical harmonic series

$$V = a \sum_{l=1}^{\infty} \sum_{m=0}^{l} \left(\frac{a}{r}\right)^{l+1} (g_l^m \cos m\phi + h_l^m \sin m\phi)\, P_l^m(\cos\theta), \tag{1.4}$$

where (r, θ, ϕ) are spherical polar coordinates, $a = 6371.2$ km is the Earth's mean radius, the $\{P_l^m\}$ are Schmidt quasi-normalized associated Legendre functions defined such that

$$\int (P_l^m)^2 \sin^2 m\phi \, \mathrm{d}\Omega = \int (P_l^m)^2 \cos^2 m\phi \, \mathrm{d}\Omega = \int P_l^2 \, \mathrm{d}\Omega = \frac{4\pi}{2l+1}, \tag{1.5}$$

where the integral is taken over the surface of the unit sphere, and the constants $\{g_l^m ; h_l^m\}$, which have the dimensions of $\boldsymbol{B}$, are the geomagnetic coefficients.

The geomagnetic coefficients are defined relative to a sphere but the Earth's surface is closer to a spheroid. All measurements except those from satellites are made in geodetic coordinates (r', θ', ϕ); we take due account of this change in coordinate system by using the procedure of Barraclough & Malin (1971), based on a spheroid with equatorial radius 6378.16 km and ellipticity 1/298.25. The interested reader is referred to their paper and FORTRAN subroutines for further details.

The measured components of magnetic field used as data in this paper (in a few cases they are not measured directly but calculated from other measured components) are of seven types; conventional geomagnetic notation defines them as follows:

$$\text{north:} \quad X = -B_\theta = r^{-1} \partial V/\partial\theta, \tag{1.6a}$$

$$\text{east:} \quad Y = B_\phi = -(r \sin\theta)^{-1} \partial V/\partial\phi, \tag{1.6b}$$

$$\text{down:} \quad Z = -B_r = \partial V/\partial r, \tag{1.6c}$$

$$\text{horizontal:} \quad H = (X^2 + Y^2)^{\frac{1}{2}}, \tag{1.6d}$$

$$\text{total:} \quad F = (X^2 + Y^2 + Z^2)^{\frac{1}{2}}, \tag{1.6e}$$

$$\text{inclination:} \quad I = \arctan(Z/H), \quad -\tfrac{1}{2}\pi \leqslant I \leqslant \tfrac{1}{2}\pi, \tag{1.6f}$$

$$\text{declination:} \quad D = \arctan(Y/X), \quad -\pi \leqslant D \leqslant \pi, \tag{1.6g}$$

where (B_r, B_θ, B_ϕ) are components of $\boldsymbol{B}$ in spherical polar coordinates.

The conventional method for determining geomagnetic coefficients is to truncate the series

(1.4) at some degree N (usually $4 \leqslant N \leqslant 13$) and to fit the coefficients to the observations by least squares parameter estimation. Equations (1.6*a–c*) have linear relations between X, Y, Z and the geomagnetic coefficients; (1.6*d–g*) nonlinear. The solution proceeds iteratively for nonlinear data from some starting model for $\{g_l^m; h_l^m\}$.

Let $\boldsymbol{m}$ be a P-vector of model parameters, where $P = N(N+2)$ is the number of model parameters, and $\boldsymbol{\gamma}$ a D-vector of measurements, where D is the number of data. Equations (1.6*a–c*) and (1.4) then give linear relations between $\boldsymbol{\gamma}$ and $\boldsymbol{m}$

$$\boldsymbol{\gamma} = A\boldsymbol{m}+\boldsymbol{e}, \tag{1.7}$$

the equations of condition for the least squares analysis, where $\boldsymbol{e}$ is an error vector. Equations (1.6*d–g*) must first be linearized, and a solution sought iteratively. We shall not describe the least squares solution to (1.7), which is standard. Our approach is designed to determine the field at the core–mantle boundary; it follows from (1.7) and is described in §3. Conventional solutions to (1.7) have been produced for different epochs by individual researchers and national agencies. A summary of main field models to date is given by Barraclough (1978), but these models are not suitable for our purpose. Many are based on small data-sets and have severely truncated series; in many cases the same data contributes to more than one model. Differences in the analyses cause large spurious changes in the core fields.

International geomagnetic reference field (IGRF) models are internationally agreed models for mapping. The agreement usually requires averaging of different national models: IGRFs are not therefore in any statistical sense 'best' models. They also contain a predictive element because data are drawn from several years prior to their epoch. Definitive geomagnetic reference field (DGRF) models are based on data straddling the central epoch. The main problem with IGRF, DGRF, or any of the models in Barraclough (1978), is that they are designed for surface mapping rather than core studies. New analyses are needed to determine the field consistently at the core–mantle boundary.

1.3. *Downward continuation to the core–mantle boundary*

Having found the geomagnetic coefficients we obtain the field at the core–mantle boundary by differentiating (1.4) and setting $r = c$, the core radius. We take $c = 3485$ km. This process (downward continuation) is unstable because the factor $(a/c)^{l+1}$ appearing in (1.4) increases with increasing l; the short wavelengths are enhanced and uncertainties in the high-degree coefficients are amplified. In fact (1.4) may not converge uniformly on the boundary of the insulating region, in this case the core–mantle boundary; extrapolation to depths beneath the core–mantle boundary is not possible. A truncated series with imperfectly known geomagnetic coefficients will contain large and inaccurate short wavelengths.

This instability is inherent to the calculation and cannot be avoided. We can, however, satisfy the observations with a minimum of short-wavelength information in the core field. The resulting solution is only one possible model, but it is unlikely to contain misleading or spurious short-wavelength information. The methods used in this paper, described in §3, have been developed over several years (Whaler & Gubbins 1981; Shure *et al.* 1982; Gubbins & Bloxham 1985). The important additional information built into the models is the core radius, the origin of the field within the core, and the insulating mantle. The core radius is well known from seismology but the other two conditions need qualification.

The second condition, that the field originates entirely within the core, fails because of electric currents in the ionosphere and magnetosphere, and because of crustal magnetization. The satellites *POGO* and *Magsat* flew through field-aligned currents in the polar regions. These currents are not believed to affect F seriously and are ignored in the *POGO* data. Of the *Magsat* data, we used only Z north of 50° magnetic latitude. It might have been better to use F there (Lowes & Martin 1987), but Z is similar to F in these high latitudes. Other external fields, probably associated with the ring current, were removed from the *Magsat* data by Langel & Estes (1985) by solving for external terms correlated with the *Dst* index.

The main external sources influencing ground-based data are magnetic storms, tides and seasonal effects. Observatory data is combined into an annual mean so diurnal, seasonal and storm effects should have been averaged out. This leaves an oscillation of a few nanoteslas, correlated with the sunspot cycle, that is certainly external in origin. Part of the signal remaining in the 1–20 year band may also be of external origin. We do not attempt to separate it.

Repeat stations may have been occupied for long enough to allow removal of the diurnal variation, but ordinary survey sites would not have been. We assume twentieth century surveys would not have been made during magnetic storms. Diurnal variations amount to 100 nT, storms to several thousand nanoteslas. These effects must be taken into account when estimating the overall accuracy of a measurement (§2).

Another source of field external to the core is crustal magnetization. Magnetized rocks typically contribute 200 nT to a magnetic measurement, much more in volcanic areas, predominantly in the short wavelengths (roughly less than 100 km). We regard this as noise, but long wavelength crustal anomalies will be mapped as core field.

The third condition requires zero electrical conductivity in the mantle. The electrical conductivity of the mantle is an interesting object of study in its own right. External fields induce currents to flow in the upper mantle, which is a poor conductor, and these induced currents influence the measured field. It is a secondary effect and we shall ignore it. More important is the effect of the deep mantle, which may be a better conductor, on the secular variation itself. The subject has been reviewed recently by Gubbins & Roberts (1987). There are two main effects. Time variations are delayed, so that they appear at the surface later than at the core–mantle boundary, and the more rapid variations are attenuated. The mantle is said to 'screen' rapid secular variation. It used to be thought that variations with periods less than about five years would be entirely external (Currie 1967), but recent observations of geomagnetic 'jerks', which take place over a year or so and are believed to be of internal origin, have provided tighter constraints on lower mantle conductivity (Ducruix *et al.* 1980). The effect on the secular variation depends on the integrated conductivity with depth. It is therefore sensitive to the thickness of the conducting layer at the bottom of the mantle, as well as its conductivity. Here we shall ignore the effects of mantle conductivity completely. This may be a poor approximation for rapid secular change, but is probably good for the decade and longer variations that concern us here (see, for example, Benton & Whaler 1983).

1.4. *Interpreting secular variation as core motions*

Edmund Halley, as early as 1692, recognized that rapid changes in the Earth's magnetic field implied mass motion inside the Earth. He thought the field originated from magnetized rocks rather than a dynamo. The induction process, whereby secular variation is generated from magnetic field by motion, $\boldsymbol{u}$, of a fluid conductor is governed by the well-known induction equation

$$\partial_t \boldsymbol{B} = \nabla \times (\boldsymbol{u} \times \boldsymbol{B}) + \eta \nabla^2 \boldsymbol{B}, \tag{1.8}$$

where

$$\eta = (\mu_0 \sigma)^{-1} \tag{1.9}$$

is the electrical diffusivity. It is a straightforward matter to calculate $\partial_t \boldsymbol{B}$ from (1.8) given $\boldsymbol{u}$, $\boldsymbol{B}$, their derivatives and suitable boundary conditions. We are concerned with the inverse problem of calculating $\boldsymbol{u}$ given $\partial_t \boldsymbol{B}$ and $\boldsymbol{B}$, which is not so straightforward.

Roberts & Scott (1965) suggested that in studies of the secular variation it should be possible to neglect the effects of diffusion in (1.8), in other words to set $\eta = 0$. In this approximation the fluid is taken to be perfectly conducting and so, by Alfvén's theorem, the field lines are frozen to the fluid and may be used as tracers for the flow. The hypothesis that this approximation is justified is usually called the frozen-flux hypothesis. Roberts & Scott did not pursue their idea for want of good core-field models. The theory was developed by Backus (1968), who showed the data must satisfy certain conditions to be consistent with the hypothesis, among which are

$$F_i = \int_{S_i} \partial_t B_r \, \mathrm{d}S = 0, \tag{1.10}$$

where S_i is a patch on the core surface bounded by a contour of zero radial field, i.e. $B_r = 0$ on ∂S_i. Such curves are called null-flux curves.

Taking the radial component of (1.8) with $\eta = 0$ and $u_r = 0$ at the core–mantle boundary we obtain

$$\partial_t B_r = -\nabla_{\mathrm{h}} \cdot (\boldsymbol{u} B_r) = -\boldsymbol{u} \cdot \nabla_{\mathrm{h}} B_r - B_r \nabla_{\mathrm{h}} \cdot \boldsymbol{u}, \tag{1.11}$$

where the horizontal gradient operator is given in spherical polar coordinates by

$$c\nabla_{\mathrm{h}} = \left(0, \frac{\partial}{\partial \theta}, \frac{1}{\sin \theta} \frac{\partial}{\partial \phi}\right). \tag{1.12}$$

Backus (1968) showed that the horizontal components of (1.8) give no additional information for $\boldsymbol{u}$ even when $\partial_t \boldsymbol{B}$ and $\boldsymbol{B}$ are perfectly known, although they do contain information on $\partial \boldsymbol{u}/\partial r$.

Most work to date has been done using (1.11) alone, but it does not determine $\boldsymbol{u}$ uniquely. On a null-flux curve it is easily seen, from the second form of (1.11) with $B_r = 0$, that u_n, the component of $\boldsymbol{u}$ along $\nabla_{\mathrm{h}} B_r$ (normal to the contour) can be found but u_t, the component along the contour, cannot. $\boldsymbol{u}$ is also ambiguous elsewhere on the core–mantle boundary.

Recent work has concentrated on resolving the non-uniqueness by imposing constraints on the fluid flow. Steady (Voorhies & Backus 1985) and geostrophic (LeMouël *et al.* 1985) motions may both be found uniquely, at least on certain patches of the core surface, and toroidal motions may be found uniquely when horizontal components of (1.8) are used (Lloyd & Gubbins 1989).

Typical values of η for the core give a diffusion time of 10^4 years for the dipole. Roberts & Scott (1965) pointed out that this was much longer than the timescale for secular variation, and thereby justified their neglect of diffusion. The diffusion time decreases with the square of the wavelength and therefore a feature with predominant spherical harmonic degree $l = 10$ (corresponding to wavelength 1000 km) would have a diffusion time of 10^2 years; the field models in this paper would then span three diffusion times. We must bear in mind the uncertainty in η and the unknown radial length scale of $\boldsymbol{B}$, but it seems unlikely the frozen-flux hypothesis will hold throughout. Indeed, Bloxham & Gubbins (1986) have found significant changes in some of the constraints (1.10). At best we can hope the frozen-flux hypothesis will give a first approximation to the core flows.

There must be a boundary layer at the top of the core, no matter how weak the diffusion. In applying the frozen-flux hypothesis we assume continuity of B_r across the boundary layer and regard $\boldsymbol{u}$ as the flow at the top of the free stream, immediately beneath the boundary layer. The boundary layer may contain a current sheet parallel to the interface. This would not affect the continuity of B_r but would produce a discontinuity in B_θ and B_ϕ, for which reason little use has been made of them. Hide & Stewartson (1972) argued that the boundary layer dynamics would be dominated by magnetic and Coriolis forces and deduced a quite negligible discontinuity in $\boldsymbol{B}_{\mathrm{h}}$ of a few nanoteslas. Furthermore, recent observations appear to satisfy consistency conditions for continuity of $\boldsymbol{B}_{\mathrm{h}}$ (Barraclough *et al.* 1989). Braginsky (1984) gives a different analysis from that of Hide & Stewartson (1972), assuming a much thicker boundary layer.

We shall proceed by using the frozen-flux hypothesis as a guide to core motions and in the future try to develop better approximations including the effects of diffusion and mantle conductivity. At present there are no quantitative theories for determining core motions from secular variation measurements in the presence of diffusion, but we make some qualitative interpretations in §8 below.

1.5. *Content of the paper*

The field models and their interpretation described in this paper are the result of several years of research and some of the models have already appeared in print elsewhere. In such cases we have included brief descriptions of the data and method to ensure continuity, and referred the reader to the relevant earlier paper for details.

We describe the data that we have used in this study in §2 and the method of inversion to obtain geomagnetic coefficients for individual epochs in §3. We describe the results of the inversion in §4. These results are in the form of maps of the magnetic field at the core–mantle boundary, together with a few relevant statistical parameters. At this stage we discuss the maps with a view to assessing their internal consistency and accuracy, but make no attempt to place any physical interpretation on them.

We interpret the maps in four stages in §§5–8. First, in §5 we describe the morphology of the core field and its time evolution. The discussion is limited to phenomena such as westward drift (or lack of it), the morphology of stationary features and other time-dependent behaviour. In §6 we assess the validity of the frozen-flux hypothesis, and use it in §7 to derive core motions. These calculations are limited by the absence of diffusion, and some features observed on the maps cannot be so accounted for, but they provide a first step to quantitative interpretation. In §8 we include diffusion and give a more qualitative interpretation of the core fields, and comment on the implications for the Earth's dynamo.

2. DATA

2.1. *Introduction*

Our earliest magnetic measurements are from A.D. 1695. The beginning of the eighteenth century saw a considerable effort in magnetic charting, prompted by the need for improved navigation, making it the natural starting date for our study. We shall refer to data from the period 1695–1900 as the 'historical data' (they had to be researched in libraries in the same way that an historian searches archives, so the term historical is appropriate). We chose four time-windows to coincide with particularly intense periods of mapping. These were 1695–1735, which includes Edmund Halley's declination data from the Atlantic (although by no means was he the only contributor to the data-set); 1760–90, which includes the voyages of Captain James Cook; 1830–60, which includes the British magnetic survey of the southern ocean, and also the earliest measurements of magnetic intensity, made by the method devised in 1832 by C. F. Gauss; and 1860–1900, which includes the *Challenger* expedition of 1872–76, which made measurements of all three components of field throughout the world's oceans. Data-sets for the first three periods have been described in full by Bloxham (1986*a*); that for 1860–1900 has not been published previously. The intervening periods 1735–60 and 1790–1830 contain rather less data and have not been studied. These will be included in a subsequent calculation of a time-dependent field model.

The four historical models presented in this paper are derived directly from observations of the field: all previous models of the historical geomagnetic field (as reviewed by Barraclough 1978) have been derived from data either from charts or from the catalogue of Veinberg & Shibaev (1969), in which the original observations have been averaged to produce data at regular grid points at fixed epochs, losing much of the fine detail of the original observations. Charts, which until very recently were produced by hand, are similarly inadequate owing to the effects of smoothing and interpolation of the original observations.

In the late nineteenth and twentieth centuries there are long-running magnetic observatories (for which it is possible to make a correction for the unwanted effect of the magnetization of the crust), a wealth of survey data and satellites. We used survey data from 1900.5 to 1960.5 together with observatory annual means to produce models for every decade from 1905.5 to 1955.5; data from observatories and the satellite *POGO-2* for 1966.0; and *Magsat* data for 1980.0. The *Magsat* model has been published before (Gubbins & Bloxham 1985) and we repeat it here only for comparison. All other twentieth-century field models described here are new. Bloxham & Gubbins (1986) and Gubbins & Bloxham (1985) present models for epochs 1959.5 and 1969.5 respectively. These models are not reported here; the 1959.5 model contains some data in common with that of the 1955.5 model described here, but the 1969.5 model is quite independent. No two models reported in this paper contain any common data so they can be regarded as independent except through their dependence on secular variation corrections, which for 1860–1900 used models for 1842.5 and 1905.5, and for the twentieth century used observatory annual means.

Each measurement must be accompanied by an estimate of its error for weighting in the analysis (described in §3). Four components comprise these errors:

(1) short wavelength crustal fields;
(2) observational errors;
(3) external fields;
(4) inaccurate secular variation corrections within the data window.

For historical data we took 200 nT per cartesian component (X, Y and Z) as representative of the magnitude of crustal magnetization at short wavelength; the observational errors varied with date and type of instrument used, and are discussed under each relevant subsection below. We ignored errors due to external fields. We did not make any secular variation corrections for the earliest two models because rates of change at that time are virtually unknown; a typical secular variation of 75 nT a^{-1} in each of the cartesian components was used to estimate the contribution to the error of a particular measurement. The combined error used for weighting amounted to about 300 nT per cartesian component. Full details are in Bloxham (1986*a*).

It is rather naïve to assign equal error contributions to each cartesian component when the error is a consequence of crustal magnetization. A more sophisticated weighting could be derived by considering the detailed nature of the magnetization of typical crust, which R. A. Langel (personal communication) is endeavouring to do for satellite data. We have experimented with different weighting schemes and found that they have very little effect on the final model. Therefore, we are content to retain the initial choice of weighting.

Angular measurements require special attention: the effect of crustal sources on declination is inversely proportional to the horizontal field intensity, and on inclination is inversely proportional to the total field intensity. We expect the observational errors to have a similar dependence on the field strength (for example, one might expect a better declination observation where the horizontal field strength is high (Cain *et al.* 1967)). To a rather crude approximation the secular variation of declination and inclination is also inversely proportional to the horizontal field strength and total field strength respectively. Equivalently, we approximate that regions of high secular variation of declination lie near the poles, and of inclination near the equator. Accordingly, we weight all observations of declination and inclination errors inversely proportional to the appropriate field strength. The constant of proportionality is based upon our estimates of the crustal field, the effects of uncorrected secular variation and our estimate of the observational errors.

2.2. *The interval* 1695–1860

All the data for this period have been published by Bloxham (1986*a*) along with the corresponding field models. We include them here for comparison with the new, later models to show the long-term trends. The reader is referred to Bloxham (1986*a*) for full details of the data preparation, here we present a brief review of the data distribution and quality.

2.2.1. 1695–1735 *data-set*

During this earliest period there was no reliable method for determining longitude at sea and the reported positions at which observations were made were often in considerable error. Many of these errors are easily recognized when the observation points are plotted; extensive corrections, sometimes amounting to over 10° in longitude, were made to this data set, in some cases after consulting the relevant ships' logs (see Bloxham 1986*a*).

The distribution for declination data is shown in figure 1 (there are 2575 observations in all). Inclinations were used from the voyages of Cunningham (1704) and Feuillée (Musschenbroek 1729; Feuillée 1714). 142 observations of inclination were used, and these are plotted in figure 2. The inclination data is very sparse and might be thought inadequate for a global field model. However, Gubbins (1986) has shown that a unique field can be obtained from dense declination measurements plus horizontal intensities (or equivalently total intensities and inclinations) made along a line joining the dip-poles. The inclination measurements in figure 2 span a good range of latitudes. Therefore, if we had total intensity measurements in addition to the inclinations, we would expect to obtain a good model.

The absence of intensity data poses a different question of uniqueness that has been studied

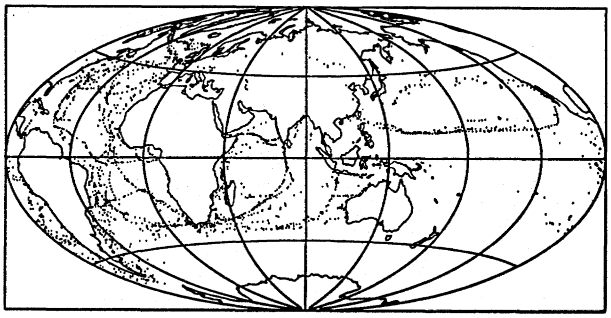

Figure 1. Data distribution on Aitoff equal-area projection, for 1715 declination observations.

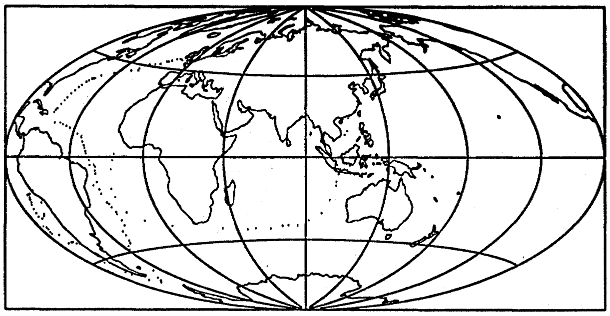

Figure 2. Data distribution for 1715 inclination observations.

by Proctor & Gubbins (1989), who conjecture that directional data can provide a unique solution, apart from a constant scalar factor, provided the field itself contains no more than two dip-poles. They provide no formal proof of this, but we hoped the conjecture implied our meagre inclination data-set would produce an adequate model. This hope was borne out by the results for this period (the model has greatly improved by the late addition of Feuillée's inclination data). We determined the constant scalar factor by setting the first coefficient g_1^0 equal to an arbitrary value, as described in §4.1.

We estimated observational errors as 1° for both declination and inclination, with the exceptions of the observations of Halley (Barraclough 1985) for which we estimated errors of 30 min arc, and the observations of the inclination at London (Malin & Bullard 1981) for which we estimated errors of 10 min arc. We made no allowance for residual navigational errors.

2.2.2. 1760–90 *data-set*

As a result of improved navigation, we found that much less correction of the observation points was necessary for this period. A large amount of this data came from the catalogue of Hansteen (1819). The voyages of James Cook gave good global coverage of inclination as well as declination (4733 observations of declination and 1382 of inclination were used). The distribution of this data is shown in figure 3 (declination) and figure 4 (inclination). We estimated observational errors 30 min arc for each measurement.

2.2.3. 1830–60 *data-set*

In 1832 Gauss devised an instrument for measuring magnetic intensity (Gauss 1833). His method was rapidly adopted at magnetic observatories and as a baseline for relative intensity

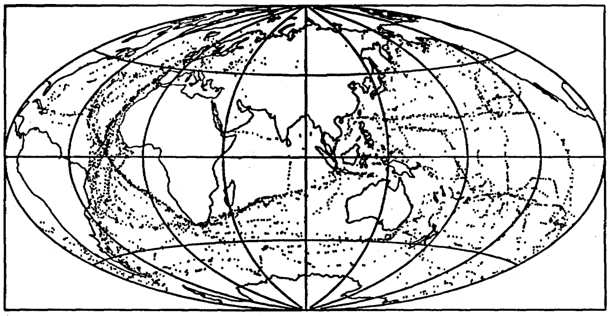

FIGURE 3. Data distribution for 1777 declination observations.

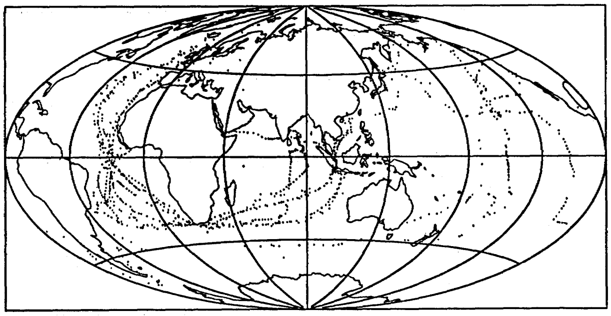

FIGURE 4. Data distribution for 1777 inclination observations.

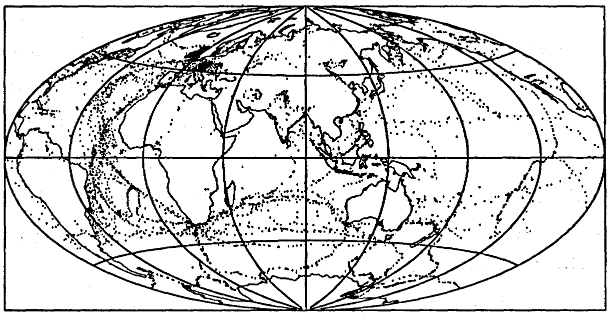

FIGURE 5. Data distribution for all 1842 observations.

measurements in surveys, and widespread intensity data became available shortly thereafter. We drew all data for this interval from the catalogue of Sabine (1868, 1870, 1872, 1875, 1877). No navigation corrections were needed. We applied secular variation corrections, where given by Sabine, to reduce the data to the central epoch 1842.5 (3170 observations of the total field intensity, 4725 observations of the inclination and 4503 of the declination were used). The data distribution is shown in figure 5, and each point represents a site where at least one measurement was made. We estimated observational errors as 500 nT for the total intensity and 15 min arc for I and D. We considered Sabine's corrections for secular variation to be accurate to within 25% and accordingly applied an error contribution of 25% of 75 nT a^{-1}.

2.3. *The interval* 1860–1900

Data from this period has not been the subject of any catalogue and therefore required considerable effort to extract from the original sources. Neither data nor the corresponding field model have been published before. The main expeditions of the period were the voyages of *HMS Challenger* and a German ship, *SMS Gazelle*. These two voyages alone ensured adequate global coverage with 3-component data. This was also a time of increasing activity in land surveys, and a surge in Arctic exploration. Naval measurements at sea increased, and charts of D were produced more frequently. Several high-quality magnetic observatories were also operating. The data collection is described in detail in the Appendix.

In total we used 10573 data (see table 3). The data distribution is shown in figure 6. The coverage is good in almost all oceanic areas, mostly from naval declination data. The U.S.A. and eastern Europe are covered by intense surveys, as are Indonesia and the Far East. Note that the Antarctic is almost devoid of measurements, in contrast to the Arctic. This is reflected directly in the error estimates on the core field, discussed in §4.4.

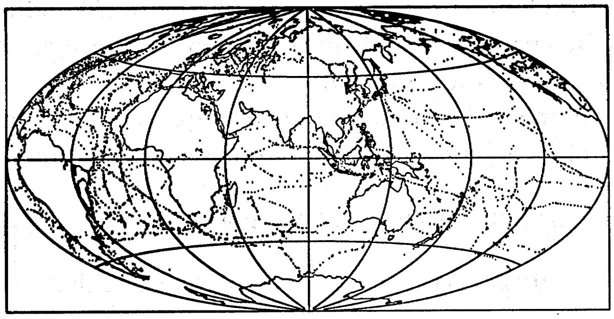

FIGURE 6. Data distribution for all 1882 observations.

We estimated errors as in §2.2.3, but with observational errors of 400 nT for F (a reduction on the 500 nT used in 1842.5) and 100 nT for H (reflecting the intrinsic accuracy of land observations of H), and 30 min arc for measurements of I at sea. We applied a secular variation correction using the difference between the 1905.5 and 1842.5 models (these models had been computed before the 1860–1900 analysis was started). We applied an error of 25% of the corresponding secular variation correction to each datum.

2.4. *Twentieth-century survey and satellite data*

A comprehensive set of twentieth-century magnetic survey data had been compiled and put onto punched cards by the Magnetic Division of the U.S. Coast and Geodetic Survey in preparation for the construction of the U.S. 1965 World Magnetic Charts (Hendricks & Cain 1963). The set was updated to include measurements to about 1970, and supplied to us on three magnetic tapes by the World Digital Data Centre C1 at Edinburgh. The cut-off date for this data-set had been arbitrarily set at 1900. It includes land, marine and aeromagnetic surveys, and repeat stations. We did not consult original sources for any of this data. A second set of tapes containing data from project *Magnet*, an airborne survey run by the U.S. Navy starting in about 1955, was also supplied by WDDC-C1 Edinburgh.

Careful study of small parts of this data-set revealed some errors that were obviously because of mispunching: '8' in place of '3', or an incorrect sign for the latitude, for example. Additionally, all data from the ship *Carnegie* were coded as 'land' data. None of these errors was serious enough to impair the inversion: we detected large isolated errors by routine inspection of the residuals from calculated field models and removed all measurements from such sites.

We assigned an error of 200 nT per cartesian component to the twentieth-century survey data. These measurements are inherently more accurate than those in the historical data-set because of improved measuring techniques and a better secular variation correction based on global analyses of magnetic observatory annual means. The crustal magnetization therefore dominates the error term.

It is essential for our modelling that errors in this data be, at least approximately, normally distributed. This would not be the case, for example, if we were to sample repeatedly a highly magnetic piece of terrain (a seamount, for example). This is a very real problem for land survey data because the tapes contain some densely spaced measurements. Consider an area with a crustal contribution of 200 nT, just one standard deviation. Ten measurements sampling the same crustal anomaly would register a systematic error of 200 nT: they would have an equivalent effect in the inversion of a single measurement with assigned error $(200/\sqrt{10})$ nT, much too small for the error in the core field.

We eliminated measurements less than about 0.2° apart to avoid highly correlated data. This culling was accomplished by accepting only one set of measurements in any one tessera defined by

$$\left.\begin{aligned} n/900 \leqslant \sin\theta \leqslant (n+1)/900, \quad 0 \leqslant n < 899, \\ 0.2m \leqslant \phi \leqslant 0.2(m+1), \quad 0 \leqslant m \leqslant 1799. \end{aligned}\right\} \tag{2.1}$$

These tesserae are approximate squares of side 0.2° at the equator. Larger tesserae, equivalent to 1° squares at the equator, were used for project *Magnet* data. This procedure left a few closely spaced data to be weeded out individually. We did no averaging of observations, only actual measurements were used.

A related problem arises when more than three components are measured at the same site (for example D, I, F and Z). Each measurement on the tapes was coded according to whether it was measured or derived from other components. Project *Magnet* and the ship *Zarya* reported four measured components although this may have been a punching error (see Hendricks & Cain 1963). The measurements of the fourth component contains the same crustal contribution as the other three and the major part of the error will therefore be correlated (for derived components all of the error will be correlated). It is essential to avoid this correlation so no more than three measurements were used for any one site.

We sought to detect erroneous data by studying the residuals to calculated field models. Some of the procedures we used are described in §3. Elimination of these errors turned out to be quite straightforward and reliable, and we did not consider it worthwhile searching the entire data-set for isolated punching errors; large crustal signals of several thousand nanoteslas were a more frequent occurrence.

Sufficient data remained after culling to allow production of a model for each decade to 1960.5. Data from 10 year windows (1900.5–1910.5, 1910.5–1920.5, etc.) were separated and corrected to the central epoch (1905.5, 1915.5, etc.) using secular variation and field models based on magnetic observatory data, produced by Langel *et al.* (1986). Numbers of data for each window are given in table 3. The survey data distributions for each decade are shown in figures 7–12.

The distribution for 1905.5 (figure 7) is a mixture of fairly good global coverage and some

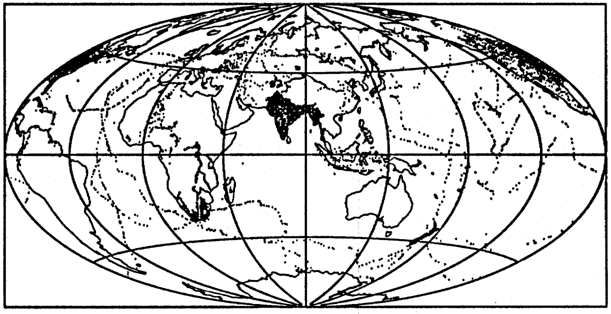

FIGURE 7. Data distribution for all 1905 observations.

intensive land surveys (India and North America for example). The uneven distribution should not have an adverse effect on the field models provided the errors remain normally distributed and do not contain a systematic bias due to crustal magnetization. This mixture of global coverage and a few regions of dense sampling is probably a good combination for field modelling because the local surveys add control for the short-wavelength fields. The distribution for 1915.5 (figure 8) is even better because of the ship *Carnegie*, which operated throughout the decade. That for 1925.5 (figure 9) is also good, apart from the southern and Atlantic Oceans.

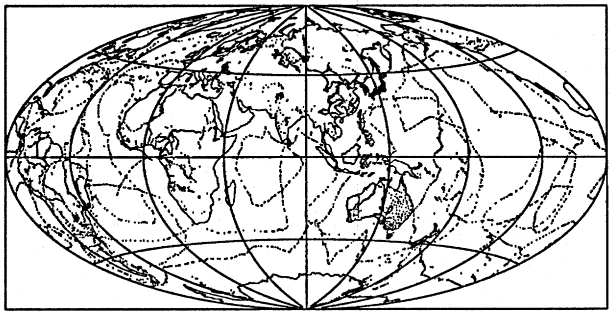

FIGURE 8. Data distribution for all 1915 observations.

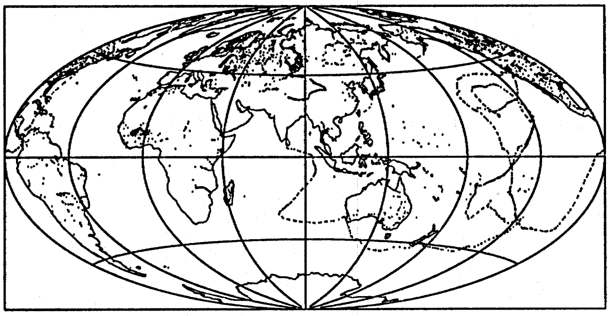

FIGURE 9. Data distribution for all 1925 observations.

As mentioned by Hendricks & Cain (1963) there is very little marine data for the two decades 1930.5–1950.5, and the data distribution maps (figures 10 and 11) are dominated by land surveys. The Soviet survey data in figure 11 probably contained a secular change correction made at source; most of the data appear to have been corrected to epoch 1940. This is undesirable, but we do not have access to the raw data. Figure 12 shows the excellent

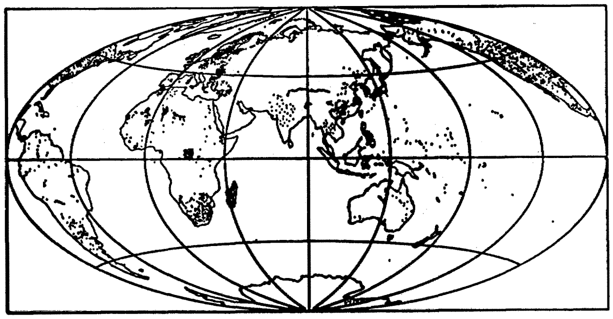

FIGURE 10. Data distribution for all 1935 observations.

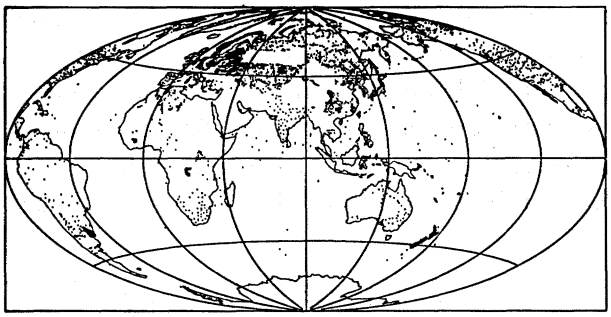

FIGURE 11. Data distribution for all 1945 observations.

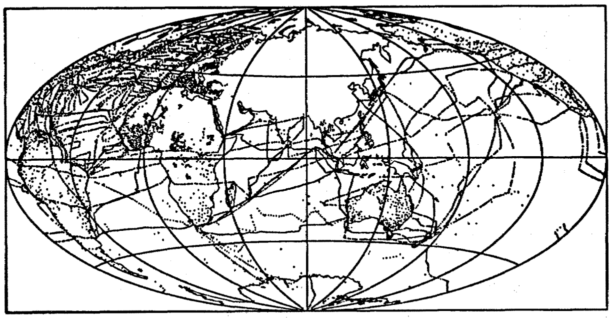

FIGURE 12. Data distribution for all 1955 observations.

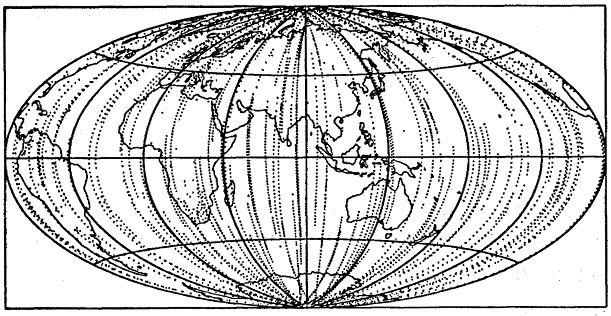

FIGURE 13. Data distribution for all 1966 observations.

coverage available for 1955.5, except for the U.S.S.R. thanks to the ship *Zarya* and project *Magnet*.

The 1966.0 model was based largely on data from the satellite *POGO-2*, which observed the total field intensity *F*. We used only quiet-time data, selected to achieve an almost equal-area distribution of observations, and assigned errors of 6 nT. Figure 13 shows the resultant data distribution.

Data for the 1980 model came from the satellite *Magsat*, as described by Gubbins & Bloxham (1985, p. 702). Again, we used only quiet-time data, and applied a *Dst* correction to remove external fields; we used only *Z*-data above 50° magnetic latitude, and assigned errors of 10 nT per cartesian component.

2.5. *Magnetic observatory data*

The contribution of the magnetized crust to the measured field at an observatory is known variously as the crustal correction, anomaly or bias. We use these terms interchangeably. To calculate the crustal corrections at each observatory we adopted the same procedure as in the previous study (Gubbins & Bloxham 1985). We used the *Magsat*-based model to define the core field in 1980. The difference between it and the observatory annual mean we then defined to be the crustal correction. We calculated an anomaly for each of the components *X*, *Y* and *Z* for each observatory. We used this approach in preference to simultaneous solution for the anomalies with the core field, as used by Langel *et al.* (1982), which suffers from trade-offs between the core field model and the anomalies (Lowes 1985), and is more complicated to apply. We corrected observatory annual means at earlier epochs for crustal magnetization by subtracting the appropriate crustal anomaly.

Many observatories did not run in 1980.0 and we had to calculate crustal corrections from other epochs. The crustal anomalies were based on the most accurate model available, preferably one of the most recent models, which are based on satellite data. For observatories that ceased operation before 1966.0 it was not possible to use a satellite model; in these cases we calculated crustal anomalies at every possible decade, using preliminary core field models, and then averaged. We then used average anomalies to produce the final core field models. We used corrected annual means either in calculating anomalies or in calculating core field, but never both.

Long running observatories with a crustal correction contribute most weight to the field models. In many cases an observatory suffered a site change, usually because nearby buildings made the old site unacceptably noisy. Even a small site change of less than one kilometre can cause a baseline change of several hundred nanoteslas, comparable with the crustal correction, and destroy the continuity of the measurement. Sometimes the observers made continuous recordings at both sites to establish the site correction, at other times they did not. We have used measured site corrections whenever possible, otherwise we devised our own corrections by interpolating across the recording gap to produce a smooth curve in each of the components *D*, *H* and *I*. In several cases a site correction could not be made: either the gap in recording was too long or the measurements were disrupted at the time of the change.

An example of a continuous record that was pieced together from three separate sites is shown in figure 14. The modern observatory on this site is at Irkutsk in Moscow. There were site changes at 1915 and 1959. Each composite set of measurements was attributed to the site that was occupied by the observatory at the date of calculation of the crustal anomalies. The

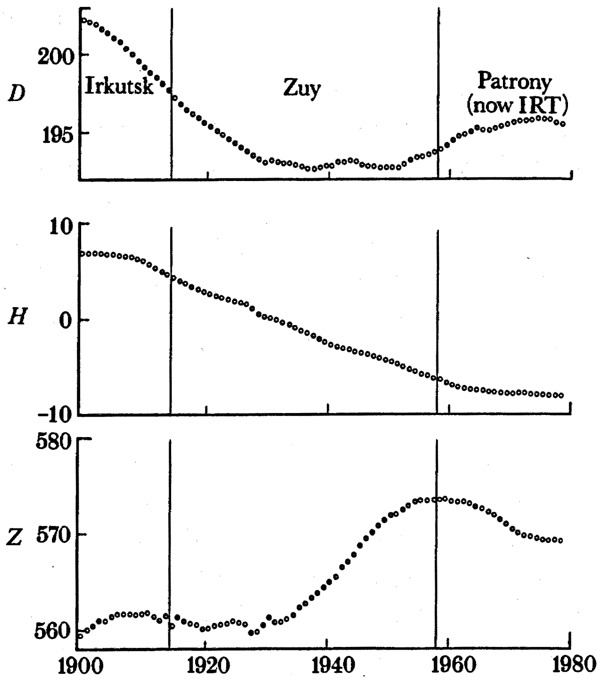

FIGURE 14. Example of a composite observatory record, produced from measurements at three different sites. Site changes occurred in 1915 and 1959. Scale for *D* is hundredths of degrees, for *H* and *Z* is hundreds of nanoteslas.

composite record was given a two-letter code to avoid confusion with the three-letter codes used by the current observatories. A list of all codes, and the observatories used to make up the composite, and the years used, are given in table 1, together with their crustal anomaly and the field models used in their calculation. Maps showing their locations are shown in figures 15 and 16. In making these composite records we have assumed that secular variation is smooth in space and we can shift site without incurring substantial errors. Some site changes were large enough for the change in core field at the site to be appreciable, making it essential that we retain just one site for each continuous recording.

We assigned to most observatories an error of magnitude 50 nT in each component. This is broadly representative of the accuracy with which the absolute baseline could be kept over several decades. Experience has shown the more sophisticated weighting used in the previous study (Gubbins & Bloxham 1985) was not worth the effort. We examined plots of each record and assigned a larger error if they appeared noisy. Some records were extrapolated by up to three years; these were given errors of 100 or 200 nT, depending on the reliability of the extrapolation. Observatories for which no crustal anomalies were available were treated as survey data.

For the 1882.5 model we used 23 observatories with crustal corrections based on our 1905.5 model. We assigned errors, as before, of 50 nT per cartesian component, but inspection of plots of *Z* shows considerable scatter for some observatories; this scatter was used to assign larger error estimates. We extrapolated some observatories by up to four years, and increased the error accordingly. We have extended the series back to 1870 for Mauritius observatory using Claxton (1899), to 1864 for Lisbon using observatory yearbooks and to 1858 for Melbourne using data supplied by Mr A. McEwin of the Bureau of Mineral Resources, Canberra. These data are not true annual means, being based on measurements made daily, or as infrequently

TABLE 1. PERMANENT MAGNETIC OBSERVATORIES USED IN THIS STUDY

(When small changes of site occurred we have joined records together and formed a composite record. The two-letter code in column 1 is our code for the composite record; the three-letter code in column 7 is the IAGA code for the most recent member of the composite set. Column 2 contains the most recent name for the contributing observatories; column 8 the names of other observatories contributing to the composite record. Columns 3, 4 and 5 contain the location of the site at which the crustal anomaly was calculated. Column 6 gives the time span of the individual observatories; at most three observatories contributed to any one record. In some cases an observatory changed its site by too great a distance to allow us to join the records together; at others a hiatus prevented joining the records. Abinger (AB) and Greenwich (GW) are an example of the former; Amberley (AM) and Eyrewell (not used) an example of the latter. Crustal anomalies were calculated by subtracting field model values from the appropriate annual mean as described in §2. Columns 9, 10 and 11 give the anomalies and column 12 gives the date of the field model used to calculate them. Some observatories did not operate in the satellite era (after 1966 for present purposes); for these an average anomaly was used from all available earlier field models. These anomalies are denoted by (—) in column 12. Blanks in this column indicate no satisfactory anomaly could be found.)

code	name	latitude deg	longitude deg	height	years used	code	former names	X	Y	Z	
AA	Addis Ababa	9.033	38.767	2.442	1958–80	AAE	—	437	−8	31	(69)
AB	Abinger	51.183	359.616	0.244	1925–57	ABN	—	76	−97	71	(—)
AE	Almeria	36.850	357.533	0.065	1955–80	ALM	—	−12	49	−4	(80)
AG	Agincourt	43.783	280.733	0.175	1900–68	AGN	—	−43	180	−157	(66)
AI	Abisko	68.367	18.817	0.380	1921–80	ABK	—	−16	74	17	(80)
AK	Ashkhabad	37.950	58.100	0.000	1959–80	ASH	—	134	99	57	(80)
AL	Alibag	18.633	72.867	0.010	1900–04, 04–80	ABG	Colaba	−243	468	613	(80)
AM	Amberley	−43.150	172.717	0.040	1902–28, 29–77	AML	Christchurch	−27	−8	57	(69)
AN	Annamalainagar	11.367	79.683	0.000	1957–80	ANN	—	122	−82	−29	(80)
AO	Muntinlupa	14.383	121.017	0.062	1900–04, 10–40, 51–80	MUT	Antipolo/Manila	−40	−64	34	(80)
AP	Apia	−13.800	188.233	0.002	1905–80	API	—	−52	218	−878	(80)
AQ	L'Aquila	42.383	13.317	0.682	1960–80	AQU	—	−19	55	−27	(80)
AR	Faraday	−65.250	295.750	0.010	1957–80	AIA	Argentine Island	59	−81	538	(80)
BA	Bangui	4.433	18.567	0.390	1952–80	BNG	—	−186	25	231	(80)
BE	Belsk	51.833	20.800	0.180	1960–80	BEL	—	108	159	313	(80)
BI	Binza	−4.267	15.367	0.300	1953–73	BIN	—	−88	−126	−119	(69)
BL	Baker Lake	64.333	263.967	0.030	1951–80	BLC	—	167	−66	−128	(80)
BO	Boulder	40.133	254.767	1.650	1964–80	BOU	—	−43	29	−253	(80)
BT	Heiss Island	80.617	58.050	0.010	1932–58, 59–79	HIS	Tikhaya Bay	72	−659	1174	(69)
BW	Baldwin	38.783	264.833	0.340	1900–09	BAL	—	—	—	—	—
BX	Bear Island	74.517	19.200	0.080	1933–80	BJN	—	−105	63	13	(80)
BZ	Bouzareah	36.800	3.017	0.340	1900–50	BZR	—	183	37	−65	(—)
CA	Genova Castellaccio	44.433	8.933	0.350	1933–69	GEN	—	12	−195	−232	(—)
CC	Cape Chelyuskin	77.717	104.283	0.010	1937–79	CCS	—	−55	−82	−67	(69)
CF	Chambon la Foret	48.017	2.267	0.133	1901–36, 36–80	CLF	Val Joyeux	−83	1	99	(80)
CI	Coimbra	40.217	351.583	0.140	1926–80	COI	—	26	20	1	(80)
CL	Clausthal	51.800	10.333	0.000	1900–18	CLZ	—	—	—	—	—
CO	College	64.867	212.167	0.200	1933–45, 48–80	CMO	—	−2	−68	−95	(80)
CQ	Cha Pa	22.350	103.833	1.550	1957–78	CPA	—	−61	−97	−97	(69)

30-2

TABLE 1. (*cont.*)

code	name	latitude deg	longitude deg	height	years used	code	former names	X	Y	Z	
CY	Capodimonte	40.867	14.250	0.160	1900–21	CPD	—	—	—	—	—
DB	Dourbes	50.100	4.600	0.208	1952–80	DOU	—	0	6	69	(80)
DD	Sabhawala	30.367	77.800	0.498	1964–80	SAB	—	−55	−61	21	(80)
DE	Dehra Dun	30.317	78.050	0.680	1903–43	DDI	—	−70	−71	−70	(—)
DI	Dikson	73.550	80.567	0.020	1933–80	DIK	—	−103	−116	−261	(80)
DO	Dombas	62.067	9.117	0.660	1916–51, 52–80	DOB	—	−103	−51	−252	(80)
DS	Dallas	32.983	263.250	0.210	1964–74	DAL	—	−14	9	−97	(69)
DU	Dumont Durville	−66.667	140.000	0.040	1957–80	DR	—	−171	−399	−2817	(80)
DV	Scott Base	−77.850	166.783	0.015	1957–79	SBA	—	−2274	−947	−3794	(69)
EB	Ebro	40.817	0.500	0.050	1905–79	EBR	—	−3	2	−16	(69)
ES	Eskdalemuir	55.317	356.800	0.245	1908–80	ESK	—	2	−21	−70	(80)
ET	Etah	78.317	287.267	0.000	1908–47	—	—	−224	113	19	(25)
FQ	Fuquene	5.467	286.267	2.543	1954–79	FUQ	—	47	−114	140	(69)
FR	Fredericksburg	38.200	282.633	0.069	1900–56, 56–80	FRD	Cheltenham	50	−87	57	(80)
FU	Furstenfeldbruck	48.167	11.283	0.572	1900–26, 27–32, 39–80	FUR	Maisach/Munich	−28	14	−6	(80)
GC	Grocka	44.633	20.767	0.231	1958–76	GCK	—	−54	−53	−71	(69)
GO	Godhavn	69.233	306.483	0.008	1903–80	GDH	—	231	−247	495	(80)
GU	Guam	13.583	144.867	0.150	1957–80	GUA	—	125	87	56	(80)
GW	Greenwich	51.483	0.000	0.050	1900–25	GRW	—	48	−35	41	(—)
HA	Hartland	51.000	355.517	0.095	1957–80	HAD	—	−44	38	46	(80)
HB	Hurbanova	47.867	18.183	0.120	1900–37, 38–79	HRB	O'Gyalla	−13	−17	−51	(69)
HF	Hermsdorf	50.767	16.233	0.000	1901–29	HDF	—	—	—	—	—
HI	Heard Island	−53.033	73.367	0.000	1948–54	HII	—	—	—	—	—
HK	Hong Kong	22.450	114.050	0.030	1900–28	HKC	—	−15	22	245	(—)
HL	Hel	54.617	18.817	0.004	1934–79	HLP	—	34	−148	−82	(69)
HO	Honolulu	21.300	201.900	0.004	1902–80	HON	—	−191	87	−335	(80)
HR	Hermanus	−34.417	19.233	0.026	1932–40, 41–80	HER	Cape Town	−14	32	71	(80)
HU	Huancayo	−12.050	284.667	3.313	1922–80	HUA	—	−8	3	34	(80)
HY	Halley Bay	−75.517	333.400	0.030	1957–75	HBA	—	−164	165	76	(60)
IB	Ibadan	7.433	35.683	0.300	1956–75	IBD	—	−3244	−3908	467	(69)
IK	Kandilli	41.067	29.067	0.130	1946–79	ISK	—	132	113	−68	(69)
JA	Jassy	47.183	27.533	0.140	1931–71	JSS	—	122	−27	152	(—)
KA	Kakioka	36.233	140.183	0.028	1900–12, 13–80	KAK	Tokyo	−17	13	−100	(80)
KC	Karavia	−11.650	27.467	1.250	1932–57, 58–61	KVA	Elizabethville	38	−69	147	(—)
KG	Port aux Francais	−49.350	70.200	0.050	1957–80	KGL	—	178	194	677	(80)
KN	Zaimishche	55.833	48.850	0.080	1914–74	KZN	Kazan	−299	−298	−249	(69)

KO	Kodaikanal	10.233	77.467	2.323	1900–80	KOD	—	−621	295	−28	(80)
KS	Ksara	33.817	35.883	0.920	1930–68	KSA	—	−66	69	−94	(66)
KV	Kiev	50.717	30.300	0.100	1958–63	KIV	—	−71	210	159	(60)
KW	Kew	51.467	359.683	0.010	1900–24	KEW	—	16	−101	115	(—)
KY	Kanoya	31.417	130.883	0.105	1958–80	KNY	—	−30	33	−44	(80)
KZ	Kanozan	35.250	139.967	0.342	1961–78	KNZ	—	−70	54	−46	(69)
LE	Lerwick	60.133	358.817	0.105	1923–80	LER	—	−131	201	26	(80)
LF	Langenberg	51.367	7.100	0.000	1900–34	BOC	—	—	—	—	—
LG	Logrono	42.450	357.500	0.445	1957–76	LGR	—	−18	4	47	(69)
LM	Maputo	−25.917	32.583	0.040	1957–80	LMM	—	311	58	−85	(80)
LN	Voeikovo	59.950	30.700	0.070	1900–44, 47–80	LNN	Slutsk	51	35	−236	(80)
LO	Lovo	59.350	17.833	0.025	1928–80	LOV	—	27	27	19	(80)
LQ	La Quiaca	−22.100	294.400	3.464	1920–80	LQA	—	15	−20	53	(69)
LR	Lwiro	−2.200	28.800	1.680	1958–70	LWI	—	206	55	13	(69)
LS	Lhasa	29.633	91.033	0.000	1957–74	LSA	—	84	21	38	(69)
LU	Luanda Capelo	−8.817	13.217	0.053	1900–19	LUA	—	290	−9	214	(80)
LU	Luanda Golf	−8.917	13.167	0.053	1954–55, 56–80	LUA	—	290	−9	214	(80)
LV	Lvov	49.900	23.750	0.400	1952–80	LVV	—	149	145	149	(80)
LY	Loparskaya	68.250	33.083	0.200	1961–80	MMK	—	64	337	−565	(80)
MA	Manhay	50.300	5.683	0.440	1932–71	MAB	—	−6	−1	201	(69)
MB	M'Bour	14.400	343.050	0.010	1952–80	MBO	—	104	70	−3	(80)
MC	Moca	3.350	8.667	1.949	1958–71	MFP	—	−74	−7	255	(69)
ME	Meanook	54.617	246.667	0.686	1916–80	MEA	—	116	1	−163	(80)
MI	Macquarie Island	−54.500	158.950	0.000	1911–80	MCQ	—	229	5	315	(80)
MJ	Mould Bay	76.200	240.600	0.150	1962–80	MBC	—	−20	−23	−88	(80)
ML	Helwan	29.867	31.350	0.120	1903–59	HLW	—	102	0	−369	(69)
MO	Krasnaya Pakhra	55.467	37.317	0.190	1930–79	MOS	—	100	−3	251	(69)
MR	Plaisance	−20.433	57.683	0.050	1900–65, 66–76	PLS	Mauritius	339	218	742	(69)
MS	Matochkin Shar	73.267	56.400	0.000	1923–53	MSR	—	132	−15	61	(—)
MT	Memembetsu	43.917	144.200	0.039	1950–80	MMB	—	−253	139	62	(80)
MW	Mawson	−67.600	62.883	0.006	1955–80	MAW	—	10	61	189	(69)
MY	Mirny	−66.550	93.017	0.020	1956–79	MIR	—	−124	38	−457	(69)
N1	Nantes	47.250	358.433	0.035	1938–58	NTS	—	39	−21	53	(—)
NG	Nagycenk	47.633	16.717	0.160	1961–80	NCK	—	8	17	−82	(80)
NI	Neimegk	52.067	12.683	0.078	1900–07, 08–31, 32–80	NCK	Sedden/Potsdam	−35	27	−75	(80)
NL	Novolazarevskaya	−70.767	11.817	0.460	1960, 61–79	NVL	—	−334	70	55	(69)
NR	Nairobi	−1.333	36.817	1.673	1964–78	NAI	—	11	0	−78	(69)
NS	Sanae	−70.300	357.633	0.080	1962–70, 71–78, 79–80	SNA	—	−42	8	44	(80)
NU	Nurmijarvi	60.517	24.650	0.105	1953–80	NUR	—	253	−80	124	(80)
NY	New Year Island	−54.650	295.850	0.000	1902–16	NYI	—	−22	−77	171	(—)
OD	Stepanovka	46.783	30.883	0.140	1936–81	ODE	Odessa	−107	−685	58	(80)
OM	Otomari	46.650	142.767	0.000	1923–43	OTM	—	—	—	—	—
OR	Orcadas del Sur	−60.733	315.217	0.004	1905–62	ORC	—	175	−52	−241	(—)

TABLE 1. (*cont.*)

code	name	latitude deg	longitude deg	height	years used	code	former names	X	Y	Z	
OS	Oslo	59.917	10.717	0.000	1900–30	QSL	—	677	−178	0	(—)
P1	Pendeli	38.050	23.867	0.110	1900–08, 35–39, 59–60	PEG	Dekelia/Athens	−6	61	184	(—)
PA	Paramaribo	5.817	304.783	0.002	1958–74	PAB	—	−6	5	4	(69)
PB	Barrow	71.300	203.250	0.000	1933–80	BRW	—	−34	−63	−25	(80)
PE	Peking	40.033	116.183	0.000	1961–74	PEK	—	549	−241	439	(69)
PI	Pilar	−31.667	296.116	0.336	1905–80	PIL	—	−46	−35	−3	(80)
PM	Port Moresby	−9.400	147.150	0.080	1957–80	PMG	—	−21	44	242	(80)
PN	Panagyurishte	42.517	24.183	0.556	1948–78	PAG	—	−215	−175	−210	(69)
PR	Pruhonice	49.983	14.550	0.329	1946–72	PRU	—	−55	25	−75	(69)
PX	Pola	44.867	13.850	0.030	1900–22	POL	—	−16	132	−123	(—)
PY	Patrony	52.167	104.450	0.500	1900–14, 15–58, 59–79	IRT	Zuy/Irkutsk	−17	44	−83	(69)
PZ	Pleshchenitzi	54.500	27.883	0.200	1961–80	MNK	—	277	195	195	(80)
QU	Quetta	30.183	66.950	1.737	1953–80	QUE	—	−64	96	−91	(80)
RB	Resolute Bay	74.700	265.100	0.030	1952–80	RES	—	66	14	20	(80)
RE	Regensberg	47.483	8.450	0.605	1931–75	REG	—	−7	37	−51	(69)
RS	Rude Skov	55.850	12.450	0.048	1907–80	RSV	—	25	25	−42	(80)
RY	Leirvogur	64.183	338.300	0.030	1957–80	LRV	—	−263	615	−497	(80)
SC	Tenerife	28.483	343.717	0.310	1959–79	SZT	—	−429	110	−1029	(69)
SF	San Fernando	36.467	353.800	0.028	1900–78	SFS	—	46	29	−15	(69)
SI	Sitka	57.067	224.683	0.022	1902–39, 40–80	SIT	—	6	−20	−87	(80)
SJ	San Juan	18.383	293.883	0.100	1903–24, 26–54, 65–80	SJG	Vieques	−29	179	−158	(80)
SM	San Miguel	37.767	334.350	0.175	1911–77	SMG	—	688	409	1712	(69)
SO	Sodankyla	67.367	26.633	0.178	1914–44, 46–80	SOD	—	−196	−98	−592	(80)
SP	South Pole	−90.000	346.683	2.800	1959–71	SPA	—	−1356	−2130	222	(60)
SR	Srednikan	62.433	152.167	0.061	1936–66	SRE	—	89	33	50	(66)
SS	Simosato	33.583	135.933	0.059	1946–53, 54–77	SSO	Kattuura	−60	50	2	(69)
ST	Stonyhurst	53.850	357.533	0.000	1900–67	STO	—	−10	17	−73	(66)
SU	Surlari	44.683	26.250	0.084	1949–80	SUA	—	3	−19	−80	(80)
SV	Sverdlovsk	56.733	61.067	0.290	1900–31, 32–76	SVD	Dubrava Vyskova	−309	−111	−497	(69)
SW	Swider	52.117	21.250	0.100	1921–74	SWI	—	−330	−100	230	(69)
SX	Santiago	−33.450	289.300	0.000	1900–09	SNT	—	—	—	—	—
TA	Tamanrasset	22.800	5.533	1.380	1933–80	TAM	—	8	−198	−96	(80)
TE	Teoloyucan	19.750	260.817	2.280	1914–75	TEO	—	−140	−18	18	(69)
TF	Dusheti	42.083	44.700	0.982	1900–05, 05–34, 38–80	TFS	Karsani/Tiflis	−283	32	−125	(80)
TG	Tangerang	−6.033	106.733	0.014	1900–44, 49–62, 64–76	TNG	Kuyper/Batavia	57	128	−70	(—)

TH	Thule	77.483	290.833	0.057	1933–80	THL	—	–31	130	21	(80)
TI	Tiksi	71.583	129.000	0.004	1944–79	TIK	—	–104	–196	–18	(—)
TK	Yangi Bazar	41.417	69.200	0.500	1900–35, 36–63, 64–80	TKT	Keles/Tashkent	–229	25	–121	(80)
TL	Toledo	39.883	355.950	0.501	1947–80	TOL	—	8	33	–21	(80)
TM	Tomsk	56.467	84.933	0.200	1958–69	TMK	—	–48	–66	–254	(69)
TN	Tananarive	–18.917	47.550	1.375	1900–76	TAN	—	327	–15	–432	(69)
TO	Toolangi	–37.533	145.467	0.457	1900–21, 22–79	TOO	Melbourne	–38	–15	68	(69)
TP	Teheran	35.733	51.383	1.367	1960–73	TEH	—	–162	40	–165	(69)
TQ	Toungoo	18.933	96.450	0.300	1905–23	TGO	—	–20	–59	3	(—)
TR	Tromso	69.667	18.950	0.112	1930–80	TRO	—	90	–397	104	(80)
TT	Tatuoca	–1.200	311.483	0.010	1957–71	TTB	—	52	–156	128	(69)
TU	Tucson	32.250	249.167	0.770	1910–80	TUC	—	–106	–82	78	(80)
TV	Trivandrum	8.483	76.950	0.300	1957–80	TRD	—	241	208	241	(80)
TW	Trelew	–43.250	294.683	0.030	1957–70	TRW	—	134	23	6	(69)
TX	Tai Pei	25.033	121.517	0.000	1919–40, 51–67	TAP	Taihoku	—	—	—	—
TY	Tihany	46.900	17.900	0.187	1949–55. 55–80	THY	Budakeszi	–24	30	–60	(80)
UA	Tsingtao	36.067	120.317	0.080	1906–36	TSI	—	–171	30	–219	(—)
UC	Uccle	50.800	4.367	0.100	1900–31	UCC	—	26	–5	130	(—)
VA	Vassouras	–22.400	316.350	0.457	1900–10, 15–80	VSS	Rio de Janeiro	–22	–77	–112	(80)
VI	Victoria	48.517	236.583	0.185	1956–80	VIC	—	19	–18	–336	(80)
VK	Gornotayozhnaya	43.683	132.167	0.200	1936–48, 51–57, 58–80	VLA	Voroshilov/Vladivostok	–28	–19	–63	(80)
VL	Valentia	51.933	349.750	0.014	1900–80	VAL	—	126	–17	8	(80)
VN	Wien Kobenzl	48.267	16.317	0.400	1929–50, 55–79	WIK	Wein Auhof	8	–2	1	(69)
VO	Vostok	–78.450	105.867	3.500	1958–79	VOS	—	–151	362	4	(69)
WA	Gnangara	–31.783	115.950	0.240	1919–58, 59–80	WAT	Watheroo	–39	–131	143	(80)
WE	Uelen	66.167	190.167	0.010	1933–79	CWE	—	–108	38	–98	(69)
WI	Witteveen	52.817	6.667	0.017	1900–38, 38–80	WIT	De Bilt	20	31	–79	(80)
WK	Wilkes	–66.250	110.583	0.010	1957–66	WIL	—	535	–271	–65	(60)
WN	Wingst	53.750	9.067	0.050	1900–32, 39–80	WNG	Wilhelmshaven	52	77	–65	(80)
YA	Yakutsk	62.017	129.717	0.100	1931–79	YAK	—	29	–1188	109	(69)
YS	Syowa Base	–69.033	39.600	0.015	1958–70	SYO	—	–30	–32	6	(69)
YU	Yuzhno Sakhalinsk	46.950	142.717	0.030	1932–41, 42–80	YSK	Toyohara	–112	–67	99	(80)
ZN	Zinsen	37.483	126.633	0.050	1918–41	ZIN	—	13	–39	106	(—)
ZS	Zo-Se	31.100	121.183	0.100	1900–07, 08–33, 33–80	ZSC	Lukiaping/Zi-Ka-Wei	–275	62	236	(80)

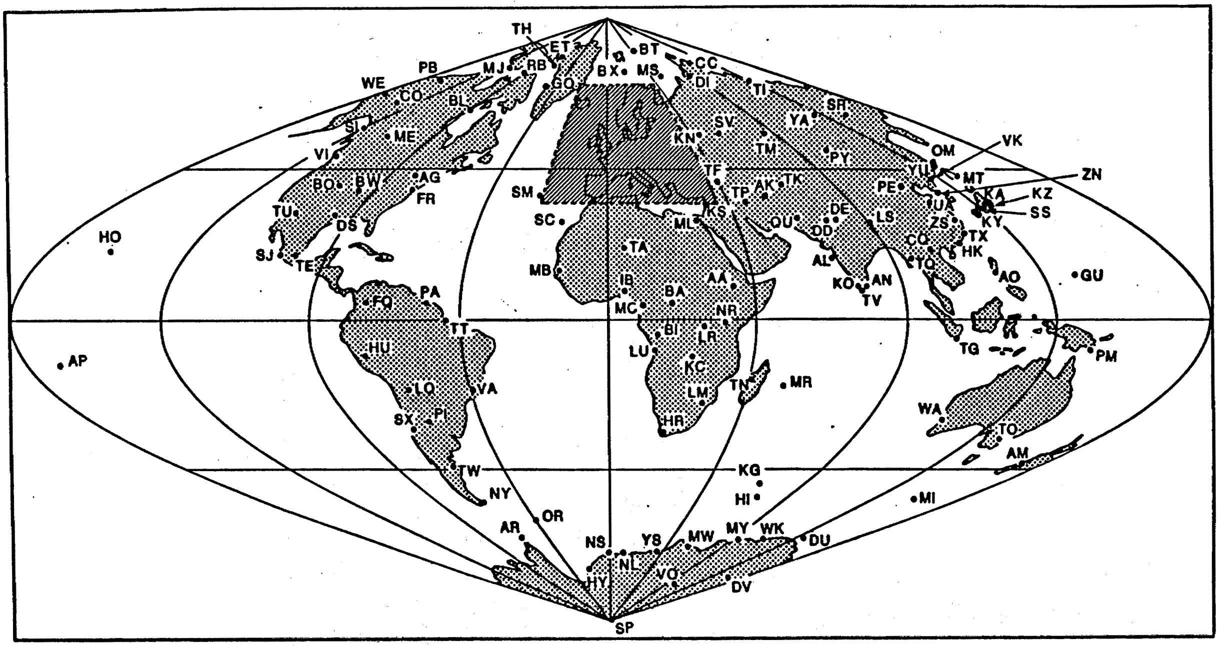

FIGURE 15. World map showing observatories used in the field modelling, together with their two-letter composite codes. The European observatories in the hatched region are shown in figure 16.

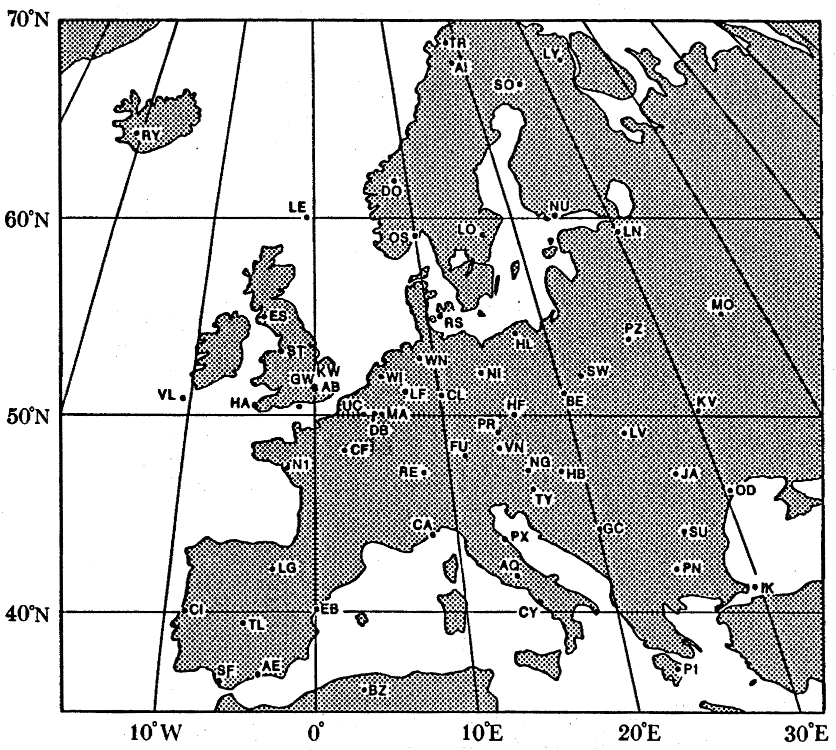

FIGURE 16. European observatories used in the field modelling, together with their two-letter composite codes.

Table 2. Observatories used in the 1882.5 analysis

(Anomalies are based on the 1905.5 model. The column entitled 'last year' indicates the year (if any) from which the data were extrapolated to obtain either an anomaly (in 1905.5) or a field value (in 1882.5).)

		anomaly			weight			last
code	name	X	Y	Z	X	Y	Z	year
LN2	St Petersburg/Slutsk	0	82	−232	50	50	150	—
OS	Oslo	659	−138	363	50	50	150	—
SV	Sverdlovsk	−237	−683	208	200	200	200	1887.5
ST	Stonyhurst	−25	−24	−119	50	50	200	—
WN	Wilhelmshaven	28	34	268	100	100	200	1884.5
IR	Irkutsk	59	113	−42	200	200	200	1887.5
KW	Kew	−32	−110	140	50	50	50	—
GW	Greenwich	7	−43	−30	50	50	50	—
PR	Prague	75	52	—	50	50	—	1904.5
VLJ	Park St Maur/Val Joyeux	−72	−96	−51	50	50	50	1883.5
FU	Munich	−2	41	−154	50	50	100	1883.5
PX	Pola	−76	52	−85	50	50	100	1883.5
AG2	Toronto/Agincourt	−17	171	−221	50	50	50	—
TF	Tiflis	−16	−45	−62	50	50	50	—
CY	Capodimonte	36	19	65	50	50	50	1884.5
CI	Coimbra	50	−39	−28	50	50	150	—
LS	Lisbon	219	−59	17	100	100	100	1900.5
ZS	Zi-ka-Wei	−231	159	−41	50	50	50	—
HK	Hong Kong	−190	88	123	100	100	100	1884.5
AL	Colaba	508	−195	−236	100	100	100	—
TG	Batavia	80	127	91	100	100	100	1884.5
MR	Mauritius	454	−238	−128	200	200	200	1883.5
TO2	Melbourne/Toolangi	−74	37	6	200	200	200	—

as once per month (e.g. Lisbon H): we increased the errors assigned to account for diurnal variations. The observatories used, together with their errors, are listed in table 2.

3. Method

3.1. *Inversion for the core field*

We determine the magnetic field at the core–mantle boundary from measurements made at or above the Earth's surface, assuming no external fields and an insulating mantle: an inverse problem with the radial component of the magnetic field at the core–mantle boundary as the model. We parametrize the model by using the spherical harmonic expansion for the magnetic potential given in equation (1.4); if the geomagnetic coefficients $\{g_l^m, h_l^m\}$ are known and the series terminates then the series can be evaluated giving the field at the core. A mathematical difficulty arises if the series does not terminate: (1.4) cannot be guaranteed to converge uniformly at the core surface, the boundary of the potential region.

We have alluded to two fundamental difficulties inherent in the inverse problem: convergence and stability. To determine the field at the core additional assumptions, or regularization conditions, must be introduced to guarantee convergence of the series (1.4) and stable downward continuation. In a conventional main field analysis, such as is used to obtain the IGRF, the series (1.4) is (in effect arbitrarily) truncated and the geomagnetic coefficients found as parameters in a least squares fit to the observations. This regularization is unnecessarily restrictive and leads to problems akin to those of truncating Fourier series

(Whaler & Gubbins 1981). We use here a different method developed for secular variation with linear (X, Y, Z) data (Gubbins 1983) and main field with nonlinear data (Gubbins & Bloxham 1985). We give a brief overview of the method along with details of its application to the new data-sets, which were discussed in §2; further details of the method are given in the earlier papers.

The magnetic field throughout the potential region is determined uniquely by the radial component on the core–mantle boundary and we need not consider the other two components. The magnetic potential V is given by the integral

$$V(\boldsymbol{r}) = -\iint_{S'} G(\boldsymbol{r}, \boldsymbol{r}')\, B_r(\boldsymbol{r}')\, \mathrm{d}S', \tag{3.1}$$

where $G(\boldsymbol{r}, \boldsymbol{r}')$ is the Green's function for Laplace's equation with Neumann boundary conditions and S' is the core–mantle boundary. Differentiating (3.1) with respect to r, θ, and ϕ and setting $\boldsymbol{r}$ equal to the position vector of a measurement site gives expressions for the three components of magnetic field. For components measured at the pole of the spherical coordinate system we have

$$Z(\theta, \phi) = -B_r = \iint_{S'} \frac{\partial G}{\partial r} B_r(\boldsymbol{r}')\, \mathrm{d}S', \tag{3.2}$$

$$H(\theta, \phi) = \iint_{S'} \frac{1}{r}\frac{\partial G}{\partial \alpha} B_r(\boldsymbol{r}')\, \mathrm{d}S'. \tag{3.3}$$

G is a function only of the angular distance, α, between the points (θ, ϕ) and (θ', ϕ') with

$$\cos\alpha = \cos\theta\cos\theta' + \cos\theta\cos\theta'\cos(\phi - \phi'), \tag{3.4}$$

$$(\partial G/\partial r)_{\boldsymbol{r}=(a,0,0)} = -b^2(1-b^2)/4\pi f^3, \tag{3.5}$$

$$\frac{1}{r}\left(\frac{\partial G}{\partial \alpha}\right)_{\boldsymbol{r}=(a,0,0)} = -\sin\theta' \frac{b}{4\pi}\left[\frac{1-2b\mu+3b^2}{f^3} + \frac{\mu}{f(f+b-\mu)} - \frac{1}{1-\mu}\right], \tag{3.6}$$

where $b = c/a$, $f = (1-2b\mu+b^2)^{\frac{1}{2}}$, $\mu = \cos\alpha$, and c is the CMB radius (Gubbins & Roberts 1983).

When measurements of only the components X, Y and Z are to be inverted the problem is linear and equations (3.5) and (3.6) can be rotated to give the data kernels for measurements of X, Y and Z at any position. They are plotted in figure 17. They represent the extent to which an observation samples part of the model. Thus Z samples the radial component of core field most strongly directly beneath the measurement site, as expected, whereas horizontal components sample it most strongly at an angular distance of approximately 23° from the site, being totally insensitive to the radial core field directly beneath the site. We can therefore expect to be able to tolerate gaps in the data distribution as large as 45° across provided we have measurements of horizontal components or some equivalent information.

The remaining four measured geomagnetic components (D, H, I, F) are related nonlinearly to B_r. The inversion for these components is carried out iteratively using a linearized form of the relation between each measurement and B_r, in exactly the same way as in the conventional approach to main field modelling. The Fréchet derivatives then give the extent to which each datum samples small changes in the core field.

We construct solutions to the inverse problem using an approach, common in geophysics, known variously as stochastic inversion or damped least squares (Hoerl & Kennard 1970; Franklin 1970; Jackson 1979; Aki & Richards 1980, ch. 12; Tarantola & Valette 1982).

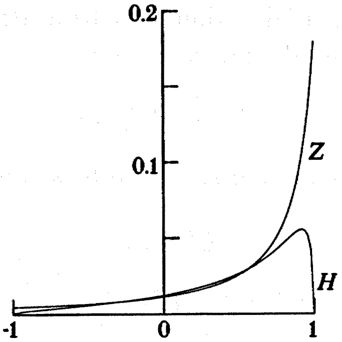

FIGURE 17. Data kernels for the vertical (Z) and horizontal (H) components of the field. The plots show how surface measurements sample the radial core field. The horizontal scale is cosine of angular distance from the point at the surface at which the field is measured. Note that although vertical field measurements sample the core field most strongly immediately beneath the measurement point, horizontal field measurements sample the radial field most strongly roughly 23° from the measurement point.

Solutions can be derived either by minimizing a norm of the model, or alternatively by specifying an *a priori* covariance matrix of model parameters in a bayesian approach. The solutions are identical in the two cases, although the underlying philosophy is different; both have the effect of regularizing the solution, resulting in convergence of the series (1.4), so that only a finite number of terms in (1.4) need be retained.

Another variant of the minimum norm solution has been given in the present context by Shure *et al.* (1982), who treat the problem in an infinite-dimensional model space, whereas we truncate the spherical harmonic series and deal with a finite-dimensional space. The latter solution converges on the former as the truncation point is increased (Gubbins 1983). It is important to distinguish between our truncation level, which is chosen for numerical convergence, and that of conventional least squares, which is chosen to fit the data appropriately. Our truncation level is set at degree 20 for all the models in this paper, which gives convergence to better than 0.1 nT in all the geomagnetic coefficients, whereas conventional analyses are based on truncation levels ranging from 4 to 13, depending on the quality of the data-set. In the method of Shure *et al.* (1982) the form of the norm is chosen so that certain infinite series of spherical harmonics can be summed to yield the elements of the Gram matrix in closed form. The solution is then free of the negligible error incurred in truncating the series but a very high price is paid: the method is restricted to specific norms; very lengthy algebra is involved every time the norm is changed; and the final numerical solution involves matrices with order equal to the number of data (30000 for one model in this paper).

The standard procedure of stochastic inversion is highly effective in the present application because the magnetic field originates in the core, and a mild constraint on the core field represents a very severe constraint on both the surface field and the geomagnetic coefficients. We are able to add additional information by introducing the hypothesis that the field originates in the Earth's core and we expect to obtain a 'better' solution because of this additional information.

Shure *et al.* (1982) were the first to suggest minimizing some norm on the core–mantle boundary, such as

$$\iint_S |\boldsymbol{B}|^2 \,\mathrm{d}S \Big/ \iint_S \mathrm{d}S. \tag{3.7}$$

Here we represent $\boldsymbol{B}$ in the potential region as a truncated spherical harmonic series with vector of coefficients $\boldsymbol{m}$ and define the norm, M, by

$$M = \boldsymbol{m}^{\mathrm{T}} C_{\mathrm{m}}^{-1} \boldsymbol{m}, \tag{3.8}$$

where C_{m} is some suitably chosen positive definite symmetric matrix, and finding $\boldsymbol{m}$ to minimize.

$$E^2 + \lambda M, \tag{3.9}$$

where λ is a damping parameter, E^2 is the sum of squares of weighted residuals,

$$E^2 = \boldsymbol{e}^{\mathrm{T}} C_{\mathrm{e}}^{-1} \boldsymbol{e}, \tag{3.10}$$

in which C_{e} is a data covariance matrix to be specified, and

$$\boldsymbol{e} = (\gamma - A\boldsymbol{m}) \tag{3.11}$$

(from equation 1.7). Adjusting λ gives a range of solutions with differing norms. M is a monotonically decreasing function of λ. The solution is called 'minimum norm' because no other solution with the same M has smaller E^2.

In the parallel approach, which has come to be known in the geomagnetic literature as stochastic inversion, $\lambda^{-1} C_{\mathrm{m}}$ is specified as an *a priori* matrix of model parameter covariances. It gives identical results for $\boldsymbol{m}$ but, in addition, allows the calculation of a covariance matrix of the estimate. As used here, the method is more correctly described as bayesian inference: Bayes' theorem is used to relate the covariances of the final estimate to the *a priori* covariances $\lambda^{-1} C_{\mathrm{m}}$. (We refer the interested reader to Backus (1988) for a more complete discussion of the philosophical distinctions between stochastic inversion and bayesian inference.) Bayesian inference was developed for the present application by Gubbins & Bloxham (1985).

Minimizing (3.9) yields the estimate

$$\hat{\boldsymbol{m}} = (A^{\mathrm{T}} C_{\mathrm{e}}^{-1} A + \lambda C_{\mathrm{m}}^{-1})^{-1} A^{\mathrm{T}} C_{\mathrm{e}}^{-1} \gamma. \tag{3.12}$$

The covariance matrix of the estimate is

$$C = \hat{\sigma}^2 (A^{\mathrm{T}} C_{\mathrm{e}}^{-1} A + \lambda C_{\mathrm{m}}^{-1})^{-1}, \tag{3.13}$$

where
$$\hat{\sigma}^2 = \boldsymbol{e}^{\mathrm{T}} C_{\mathrm{e}}^{-1} \boldsymbol{e} / [D - \operatorname{tr}(R)], \tag{3.14}$$

and
$$R = (A^{\mathrm{T}} C_{\mathrm{e}}^{-1} A + \lambda C_{\mathrm{m}}^{-1})^{-1} (A^{\mathrm{T}} C_{\mathrm{e}}^{-1} A) \tag{3.15}$$

is the resolution matrix, which relates the expected value of the estimate $\hat{\boldsymbol{m}}$ to the true model $\boldsymbol{m}$. Note that $\hat{\sigma}^2$, M and λ are dimensionless numbers, whereas the units of C_{e} and C_{m} are square nanoteslas.

In describing the properties of a particular model we shall quote the norm, M, which is a measure of the roughness of the field at the core–mantle boundary, the misfit $\hat{\sigma}$, which is a measure of how well the model fits the weighted data and should be approximately unity if the weighting is correct, the formal errors of the radial field at the core–mantle boundary calculated from the covariance matrix (3.13), and the trace of the resolution matrix, which is a measure of the number of degrees of freedom in the model (cf. table 4). Any model estimate is acceptable when taken with its resolution matrix, which relates it to the true model, and its covariance matrix. The models in this paper were all calculated with the 'dissipation' norm of Gubbins & Bloxham (1985) with

$$C_m = \operatorname{diag}\{(c/a)^{2l}(2l+1)/4\pi(l+1)^2 l^4\}, \tag{3.16}$$

which was justified by requiring an approximate estimate of the ohmic heating to be finite.

The main practical advantage of this approach lies in its close similarity to traditional methods of analysing main field: the computational procedure differs only in adding damping terms to the normal equations matrix; data measured in geographic rather than geocentric coordinates can be used; and computational aspects of the two approaches are the same when $\lambda = 0$ (the resolution matrix then becomes the identity and its trace the number of spherical harmonic coefficients). However, this last comparison is misleading, because in stochastic inversion the solution for $\lambda \neq 0$ is independent of the truncation level, except for numerical error, and the series does not converge when $\lambda = 0$.

3.2. *Procedure for finding a model*

Our observatory data consists of annual means of X, Y and Z, which are linear and produce a final model that is independent of the starting model. The survey and *POGO* data contain measurements of D, H, I and F, which are not linear and must be inverted iteratively, moving away from a starting model. For starting models we used those collected and published by Barraclough (1978) for 1715.0, 1777.5 and 1842.5; an average of our 1905.5 and 1842.5 models for 1882.5; observatory-based field models for the twentieth-century models; and IGRF 1965 for the *POGO* satellite-based model at 1966.0. We found no evidence of dependence of the final solutions on the starting models in this case. The two earliest models contain no intensity measurements (a minimum norm solution would therefore have produced a zero field!). We obtained a non-zero solution by forcing the coefficient g_1^0 to be unity, effected by replacing the first normal equation by $g_1^0 = 1$. The coefficients can be scaled to produce any desired value of g_1^0, once a solution with $g_1^0 = 1$ has been obtained.

The estimate (3.12) will only be a maximum likelihood (minimum variance) estimate if the error statistics are gaussian, which is not the case for our data (see §4.3). We adopted a simple remedy of rejecting bad data during the iterations. No datum was rejected from the first iteration; in later iterations any measurement further than 10 standard deviations from the model prediction was rejected, then the cut-off point was reduced to five standard deviations and finally to a level of three standard deviations. At each stage we examined the rejected data for the cause of the problem and studied the core field map for spurious features. The model was recalculated after identification of any bad data.

The twentieth-century observatory data were inverted separately from the survey data in the initial stages. Differences between the observatory and survey models were inspected for evidence of bad data. (Differences were usually remarkably small, even early in the century when fewer than 50 observatories were operating.) We then combined the revised data-sets and calculated a final field model by using the rejection procedure above.

The important choice of damping constant is discussed in §3.4. For each model we calculated the trace of the resolution matrix, misfit, covariance matrix and formal errors in radial field on the core–mantle boundary (see table 4).

Details of the data contributing to each of the models are given in table 3. Each model is identified by the date to which measurements were reduced by using a secular variation

TABLE 3. DETAILS OF THE DATA CONTRIBUTING TO EACH MODEL

(The model year is the epoch to which all data were reduced (except the two oldest models, for which no secular variation data were available). The data year is the average date of all the contributing survey data (excluding the observatory data). The remaining columns give the number of measurements by component; the differences in their distribution between epochs is due mainly to the availability of different instruments.)

model year	data year	data total	data rejected at 3σ	D	H	I	X	Y	Z	F
1980.0	1980.0	4178	0	0	0	0	1262	1262	1654	0
1966.0	1966.0	11040	21	424	392	117	146	146	460	9334
1955.5	1957.4	30732	319	9335	4168	6754	136	135	2963	6922
1945.5	1945.5	16208	367	7079	4290	3135	86	86	1084	81
1935.5	1936.1	16700	506	8154	4089	2477	96	96	1282	0
1925.5	1924.4	23210	554	10711	6028	5567	62	62	225	0
1915.5	1914.8	24865	393	9812	7489	7040	51	51	56	0
1905.5	1905.4	20203	267	7639	6029	6106	47	47	47	0
1882.5	1880.0	10573	534	5214	1529	2601	39	39	37	585
1842.5	1844.2	12398	380	4335	0	4615	0	0	0	3068
1777.5	1776.9	6115	288	4551	0	1276	0	0	0	0
1715.0	1715.7	2636	81	2508	0	128	0	0	0	0

correction, except for the oldest two for which no correction was made and which are identified by the centre of the data window. The second column contains the average date of all measurements, the 'data year' of the data-set. The largest bias is two years (for the 1955 model, caused by a large volume of data from late in the decade associated with project *Magnet* and the International Geophysical Year).

3.3. *Crustal magnetization as a source of error*

The estimation of the elements of C_e, the data covariance matrix, presents a formidable obstacle. The adage 'one man's signal is another man's noise' applies with some force in this case because the major component of our noise is the crustal magnetization, whereas the geophysicist interested in charting crustal anomalies must remove the core field from his map. The whole problem of statistical inference lies rooted in the difficulty of separating core and crustal signals, which is usually done by assuming the core field constitutes the long wavelength part of the signal and the crustal magnetization the short wavelength.

Figure 18 shows the power spectrum of the magnetic field at the Earth's surface. The interpretation usually made of this figure (see, for example, Lowes 1974; Langel & Estes 1982) is that the core field dominates up to about degree 14 (the 'knee' in the graph) and the crustal field from thereon. This interpretation, although plausible, is totally *ad hoc*: it is merely a convenience introduced by field modellers. Contrary to the implications of some studies, separation of the core and crustal fields is impossible on the sole basis of measurements taken above the Earth's surface: assumptions must be made about the nature of crustal magnetization as well as the core field to make the argument plausible. In our formulation the assumptions about crustal magnetization go into the elements of C_e; those about the core field into the elements of C_m. A discussion of crustal fields is therefore in order.

Crustal fields result from two sources: the induced magnetization of rocks with significant magnetic susceptibility and the remnant magnetization of rocks, generally acquired by cooling through the Curie point in a magnetic field. This picture is actually rather over simplified:

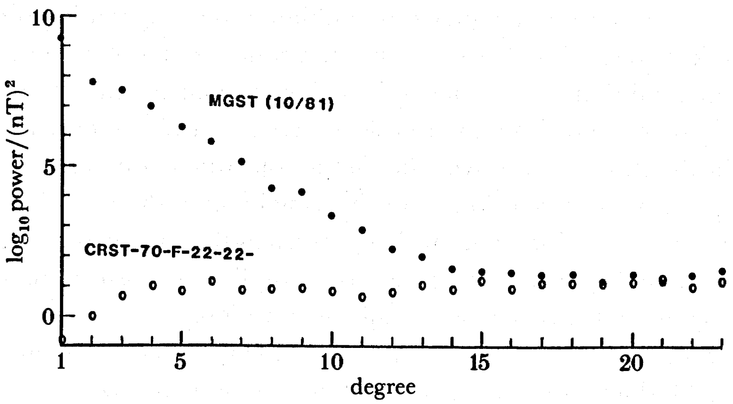

FIGURE 18. Power spectra at the Earth's surface of MGST(10/81) field model and CRST-70-F-22-22- crustal model. MGST(10/81) is based on field observations, whereas CRST-70-F-22-22- is based on forward modelling of crustal magnetization. The approximate agreement of the two models from about degree 14 onwards lends some justification to the common assertion that harmonics of above degree 14 largely represent crustal sources.

rocks also acquire viscous components of magnetization which are induced magnetizations acquired over longer time periods and with longer decay times. Whereas an ordinary induced magnetization is acquired almost instantaneously (*ca.* 10^{-8} s) and decays, on removal of the inducing field, similarly, rapidly viscous magnetizations are acquired and decay over very much longer timescales of up to millions of years. For our purposes it will be adequate to consider induced magnetization as being dependent on the magnetic susceptibility of the material and the ambient field, and remnant magnetization dependent on the historical field. Induced magnetizations are parallel (or nearly parallel if we include the possibility of anisotropic susceptibility) to the inducing field direction, while the direction of remnant magnetization depends upon the direction of the field when the material last cooled through its Curie temperature, plus the effects of tectonic rotations and deformations.

The ratio of remnant magnetization to induced magnetization is known as the Köenigsberger ratio. Köenigsberger ratios are generally found to be high (of the order of 50) for oceanic basalts (Vacquier 1972), although rather lower for continental basalts. This implies that over oceanic crust the crustal field is likely to be dominated by remnant sources, with a more even balance over continental crust. Our concern is the extent to which these crustal sources are likely to contaminate models of the core field. Core field models include wavelengths at the Earth's surface of greater than, say, 3000 km and so we can safely consider crustal fields of wavelength shorter than, say, 300 km as a source of random noise, although we must beware of the possibility of aliasing on account of uneven data distributions. Our concern is, then, primarily with components of crustal magnetization of greater wavelength than 300 km; we refer to these as long wavelength sources of crustal magnetization (commonly, wavelengths below 65 km are referred to as short; wavelengths from 65 km to 1500 km as intermediate; and wavelengths above 1500 km as long, so our terminology is non-standard).

Although remnant magnetization is likely to be the dominant contribution, or at least to contribute equally, to the crustal field at a point, at these long wavelengths we can expect induced magnetization to be dominant. The wavelengths associated with remnant magnetization of oceanic crust are well known from studies of magnetic reversal stripes (Vacquier 1972), which, in general, have a separation of the order of 10 km. It should, however, be remembered that the wavelength of magnetization oblique to the spreading direction is much greater (Shure & Parker 1981). Furthermore, in quiet zones (zones of oceanic crust extruded during periods of predominantly one magnetic polarity) longer wavelengths can also be important. Indeed, LaBrecque & Raymond (1985) have recently demonstrated that such an effect is detectable in the *Magsat* data over the Cretaceous quiet zone in the North Atlantic. We shall, for the purposes of this discussion, while bearing in mind these possible complications, assume that induced sources are dominant at these wavelengths for oceanic crust; we shall also assume this for continental crust. The generally complicated history of deformation of continental crust suggests that this is a reasonable assumption.

Recently, J. Meyer and colleagues (Meyer *et al.* 1983; Hahn *et al.* 1984) have attempted to model the crustal field down to wavelengths of about 500 km by a forward modelling technique. They divide the crust into blocks of 2° by 2° and either two or three layers. These blocks are then classified by using one of 10 (in the earlier paper) and 16 (in the later paper) crustal types. The magnetization of this model induced by a model of the core field is then calculated. Although this method has obvious serious weaknesses, the assessment of subsurface crustal type being an obvious one, it does represent a useful attempt at studying the separation of core and crustal fields. The crustal model CRST-70-F-22-22- of Hahn *et al.* (1984) does reproduce the power spectrum beyond the 'knee', lending some real justification to the usual interpretation (see figure 18).

To summarize, observations of the field made on the Earth's surface will contain a significant crustal component (we have assumed 200 nT per cartesian component) most of which is of very short wavelength and so may be treated as random observational noise. This short wavelength component becomes small at satellite altitude owing to the attenuation in upward continuation. Satellite data is equivalent to densely spaced ground survey data which has been passed through a spatial low-pass filter by virtue of the satellite's altitude; it can therefore be used to remove the short wavelength component at magnetic observatories and repeat stations. The long wavelength component of crustal magnetization places a limit on the resolution of small scale structure in the core. The problem of contamination is more serious for studying crustal fields than it is for core fields: models of the crustal field lose resolution at the long wavelength end of the spectrum owing to core fields, and so lack essential large scale variations, whereas core field models lose resolution only at the short wavelength end of the spectrum (from the 'knee' onwards) and so lose only small-scale resolution. If, in the future, forward models of the crustal field become more reliable it may be possible to remove the influence of long wavelength crustal fields from the data, so extending the resolution to smaller-scale core features.

3.4. *A discussion of error estimation*

The most critical step in this inversion is also the most difficult to justify, the choice of the damping parameter λ. We consider here three different underlying philosophies for our method; all three give identical models but only one yields error estimates on the model parameters. The great similarity between the methods has led to some confusion, which we hope this discussion will clear up.

The first philosophy we can call the 'mapping' approach. The end product is the map of the radial component of magnetic field at the core–mantle boundary which will subsequently be studied to gain insight into the processes causing the secular variation in the core. In our view this is the most important activity because our main concern is to understand the dynamo;

other workers may have different goals. We would like to avoid large differences between maps of different epochs arising from data-sets of widely differing quality. The nearest quantitative criterion would then be to choose λ to give the same norm M for each model, because then each core field map would be equally 'smooth'. From the geophysical point of view this is the most sensible approach, but unfortunately it is the most difficult to justify in terms of statistics.

Another approach is warranted if our primary interest is to fit the data with the 'simplest' model (either the model with the least number of degrees of freedom or, in this case, the smallest possible norm). The appropriate choice of λ would then be such as to give a misfit of unity to the weighted data. Unfortunately, this process tells us more about the quality of the data distribution than it does about the physics of the core field, but for the surveyor wanting the simplest possible representation of the core field to remove from his survey it would be very suitable.

Thirdly, there is the bayesian approach in which we suppose we know *a priori*, from our knowledge of core physics (which is independent of the data-set being inverted), the elements of the covariance matrix $\lambda^{-1}C_m$. λ is then fixed for all the epochs (because presumably the core physics does not change on the decade or century timescale!), and we should not change it. Bayes' theorem then relates the covariances of the model estimates to the *a priori* model covariances. This is the only philosophy of the three that allows error estimates to be calculated, or, equivalently, to quantify the range of permissible models. Bloxham & Gubbins (1986) tried to achieve the ideal bayesian philosophy by using similar λ for three recent models and tried to add some quantitative hypothesis testing to the calculations by using the error estimates to test the frozen-flux hypothesis (see also §6).

The first of these approaches needs no further explanation, the second is purely of inverse-theoretical rather than geophysical interest and we do not consider it further and the third differs only in its use in producing error estimates. We consider now the meaning and nature of these error estimates. These errors are described as 'formal' because they represent the uncertainty in the model subject to the restrictions we have placed upon it (in this case the double restriction of satisfying the measurements and the prior information). They may be invalidated either by faulty observations or by overly severe prior information. It is therefore important that we state the precise meaning of the covariances, and their dependence on the underlying assumptions.

One contribution to the model error comes directly from the data errors: inaccuracies in the measurements are simply mapped into the model. The corresponding model parameter error we shall call the standard error; it is derived from the covariance matrix C_s, where

$$C_s = \hat{\sigma}^2 (A^T C_e^{-1} A + \lambda C_m^{-1})^{-1} A^T C_e^{-1} A (A^T C_e^{-1} A + \lambda C_m^{-1})^{-1}, \tag{3.17}$$

which is related to the covariance matrix C in equation (3.13) and the resolution matrix R in equation (3.15) by

$$C_s = RC. \tag{3.18}$$

Thus C_s gives the variance of the solution if we were to resample the data, keeping the same geographical distribution. It does not contain that part of the variance in a particular parameter associated with trade-offs in resolution with other parameters: such trade-offs occur when two or more combinations of parameters have the same effect on the fit to the data. This problem is circumvented in conventional least-squares parameter estimation: resolution is perfect, $R = I$, up to the truncation level, and there is no distinction between C and C_s (cf.

equation 3.18); of course, above the truncation level resolution is identically zero. However, trade-off is usually the most severe limitation on an estimate in geophysical applications and its contribution to the variance of the solution usually dominates the standard error. The covariance matrix C gives the uncertainty in the model parameters while still satisfying both data and prior information, which in all cases will be larger than the standard-error covariance matrix C_s.

Equation (3.18) gives some more insight into the difference between the two covariance matrices. The resolution matrix gives the mapping from the true model to the estimate. A row of the resolution matrix gives the linear combination of true model parameters that go to make up an estimate of one of the model parameters. C gives the covariances of the true model (provided the data have been weighted correctly and the prior information is valid) and therefore RC contains the covariances of the estimate, i.e. those without regard to lack of resolution of each model parameter. Thomson & Gubbins (1982) calculated both standard and total estimation errors for a seismological inverse problem and found the latter to exceed the former by a factor of 2–3: in that one case the variance, because of noise in the measurements, was dominated by uncertainty due to lack of resolution. Lowes (1987) has asserted that we have omitted a bias term. This would have been the case if we had used C_s rather than C: this confusion arises from failing to distinguish between stochastic inversion and bayesian inference.

At this stage we mention some points of 'practical' importance, by which we mean those parts of the procedure which do, and those which do not, produce much change in the solutions. First, a change by a factor of ten or so is needed in the damping constant λ to produce a noticeable change in the appearance of the core field maps; the error estimates are rather more sensitive to λ. Secondly, the estimation of C_e is uncertain by perhaps a factor of 3, which produces exactly the same effect on the solution as a scaling of the damping constant λ. Thirdly, non-gaussian data produce a very marked effect on the solution: three isolated measurements on a highly magnetic Pacific island in 1944 produced an enormous core field anomaly. We hope that these considerations put the discussion of the differences in philosophy into perspective: the differences are fundamental but quite unimportant in the appearance of the resulting core field model.

Clearly our error estimates will be valid only if the prior information is valid. There is no way in which our choice of λ can be justified *a priori* in the way we would wish. The point at issue is not whether λ should be changed by a small factor, but whether it should be changed by many orders of magnitude and whether the structure of C_m is correct. We recognize that a change in the prior information to a more conservative form will increase the errors on the model parameters, and offer the following discussion on how we believe a more conservative form could be argued for. The specific form of the damping has the effect of shaping the spherical harmonic spectrum so that the energy in higher terms falls off according to a prescribed formula, which depends on the norm. Data can change this tapering, but our measurements have little effect at high spherical harmonic degree. In our models the spectra fall off as $(c/a)^{2l}$ times some power of l, depending on the choice of norm. The geometrical factor is dominant because it increases by $(a/c)^2 \approx 3.34$ with each increase in l, compared with $(l+1)/l$ raised to some power, which is close to unity for large l. The important part of the prior information in determining the model is the core radius and not the specific choice of norm on the core–mantle boundary.

Stochastic inversion can incorporate a wide range of different norms. For example truncation of the spherical harmonic expansion can be viewed as stochastic inversion in which model coefficients with degree higher than the truncation level N are down-weighted so heavily as to make them zero, while those with lower degree are weighted equally. The effect on the spectrum is that of forcing a cut-off at spherical harmonic degree N; the covariance matrix given by conventional least squares will correspond to both C and C_s, which are equal in this case and contain the assumption (prior information) that all harmonics of degree higher than N are identically zero (and therefore their uncertainty cannot contribute to C).

We believe the assumption made implicitly in truncating the expansion, that all terms higher than some truncation level N in the spherical harmonic representation of the core field be zero, is quite unreasonable (although it may be a reasonable way to go about representing a surface field in regions of uniform data coverage for mapping purposes). We have tried to justify an imposed tapering of the spherical harmonic spectrum on physical grounds by arguing that small-scale features with large amplitude would contribute to an unrealistically large value of the Ohmic heating in the core (Gubbins & Bloxham 1985). The tapering imposed on the spectrum was chosen to make the spherical harmonic series for the integral of $B_r \nabla_h^2 B_r$ over the core–mantle boundary fall off as l^{-1}, i.e. to diverge as slowly as possible. This assumption provides convergence for the error series for any component of field on the core–mantle boundary.

It is possible to place a lower bound $\Phi_{\min}$ on the electrical heating Φ in the core using the geomagnetic coefficients and an assumed value of the electrical conductivity of iron. Gubbins (1975) derived the formula

$$\Phi > \Phi_{\min} = \frac{4\pi}{\sigma} \sum_{l=1}^{\infty} \frac{(l+1)\,(2l+1)\,(2l+3)}{l} \left(\frac{a}{c}\right)^{2l+4} \sum_{m=0}^{l} [(g_l^m)^2 + (h_l^m)^2], \tag{3.19}$$

which formed the basis for one of the norms used by Gubbins & Bloxham (1985). Equation (3.19) could be used to provide error estimates by using Backus linear inference (Backus 1970*a*, *b*, *c*). The inequality (3.19) defines a hyperellipsoid in parameter space, the data define an open surface, and the allowed solution space is the closed intersection of the two. Error bounds provided by Backus linear inference are usually too pessimistic to be of much help (see the discussion by Parker 1977) and we know it to be so in this case, indeed no bound is placed at all on point values of the magnetic field at the core–mantle boundary.

This discussion highlights the weakness of the derivation of error estimates based on our form of the prior information. It is true that the spherical harmonic series must fall off faster than the required rate at sufficiently high degree, but we do not know *a priori* the degree at which it will occur. Our choice of damping constant usually makes the spectrum fall off near degree 12, at about the point where resolving power of the data falls off (see §3.4). However, the bound (3.19) does not guarantee that this imposed tapering will start at degree 12, it may not start until some higher value, while still satisfying the inequality. There is, therefore, a range of wave numbers in the spectrum which are not constrained by either the data or the inequality (3.19), but which have been constrained by the *a priori* information we have used. This is the weak point in our argument for the choice of *a priori* information.

In this paper we have sought to take a geophysically reasonable approach: our error estimates are most certainly dependent on our assumptions which we are unable to justify rigorously, but are nevertheless less unreasonable than other alternatives that have been explored. Backus (1988) argues that the only valid *a priori* information is that the magnetic field energy should not exceed the rest mass of the Earth, or, if we are willing to assume that the heat flowing across the core–mantle boundary does not exceed the heat flux at the Earth's surface, that $\Phi_{\min}$ should not exceed the surface heat flux. Dynamo theory suggests the presence of a strong toroidal field in the core (most likely resulting from the effect of differential rotation in the core on the poloidal field); this toroidal field is likely to dominate the Ohmic dissipation in the core yet it does not even enter into $\Phi_{\min}$. We might reasonably expect $\Phi \gg \Phi_{\min}$. Additionally, it is reasonable to expect that a substantial proportion of the surface heat flux results from radiogenic heating in the crust and mantle.

We stress that these criticisms only pertain to our error analysis. The use of stochastic inversion to construct solutions with desirable mathematical properties (for example, adequate regularization) have not been questioned.

4. RESULTS

4.1. *Model parameters*

Table 4 shows the model attributes. The norm is approximately uniform for all except the last two models, for which we calculated the norms with the dipole (g_1^0) term normalized using the linear extrapolation formula

$$g_1^0(t) = -31\,110.3 + 15.46(t - 1914.0) \tag{4.1}$$

TABLE 4. MODEL PARAMETERS

(The damping constant is λ, the parameter discussed in §3.4. The norm M is defined in §3.2 and is a measure of the roughness of 'energy' in the model. * indicates that the norms have been calculated using the extrapolation of g_1^0 given in equation (4.1). The misfit is the mean residual between the model and the data (reduced to unit variance); ideally it should be unity. The resolution is the trace of the resolution matrix and is a measure of the number of degrees of freedom of the model, roughly equivalent to the number of spherical harmonic coefficients retained in a spherical harmonic expansion. The range of errors on the core–mantle boundary gives an idea of the variability in data distribution for the model; their absolute values, and in particular the asymptotic errors (corresponding to spherical harmonic degrees 21 and above, see Gubbins (1983)) are unreliable because the damping constant changes between models: they cannot be compared across models.)

model year	damping constant/10^{-14}	norm/10^{12}	misfit	resolution	error range/μT	asymptotic error/μT	model year
1980.0	1000	136	1.09	150	23–24	16	1980.0
1966.0	2000	130	1.29	144	19–27	13	1966.0
1955.5	200	132	0.87	137	39–60	28	1955.5
1945.5	75	126	0.87	119	60–132	14	1945.5
1935.5	150	124	0.97	112	51–103	36	1935.5
1925.5	200	124	0.94	118	44–87	30	1925.5
1915.5	330	131	0.89	125	34–45	22	1915.5
1905.5	130	129	0.94	124	54–84	37	1905.5
1882.5	90	132	1.03	115	49–79	49	1882.5
1842.5	130	132	0.92	102	62–91	36	1842.5
1777.5	170	88*	1.09	83	76–106	38	1777.5
1715.0	400	47*	1.03	54	59–123	23	1715.0

DESCRIPTION OF PLATES 1–4

FIGURE 19. Maps of the radial component of the magnetic field at the core–mantle boundary. The orange shades represent intensity of flux out of the core, the blue shades intensity into the core. The map projection is Aitoff equal-area. (*a*) 1980.0; (*b*) 1966.0; (*c*) 1955.5; (*d*) 1945.5; (*e*) 1935.5; (*f*) 1925.5; (*g*) 1915.5; (*h*) 1905.5; (*i*) 1882.5; (*j*) 1842.5; (*k*) 1777.5; and (*l*) 1715.0.

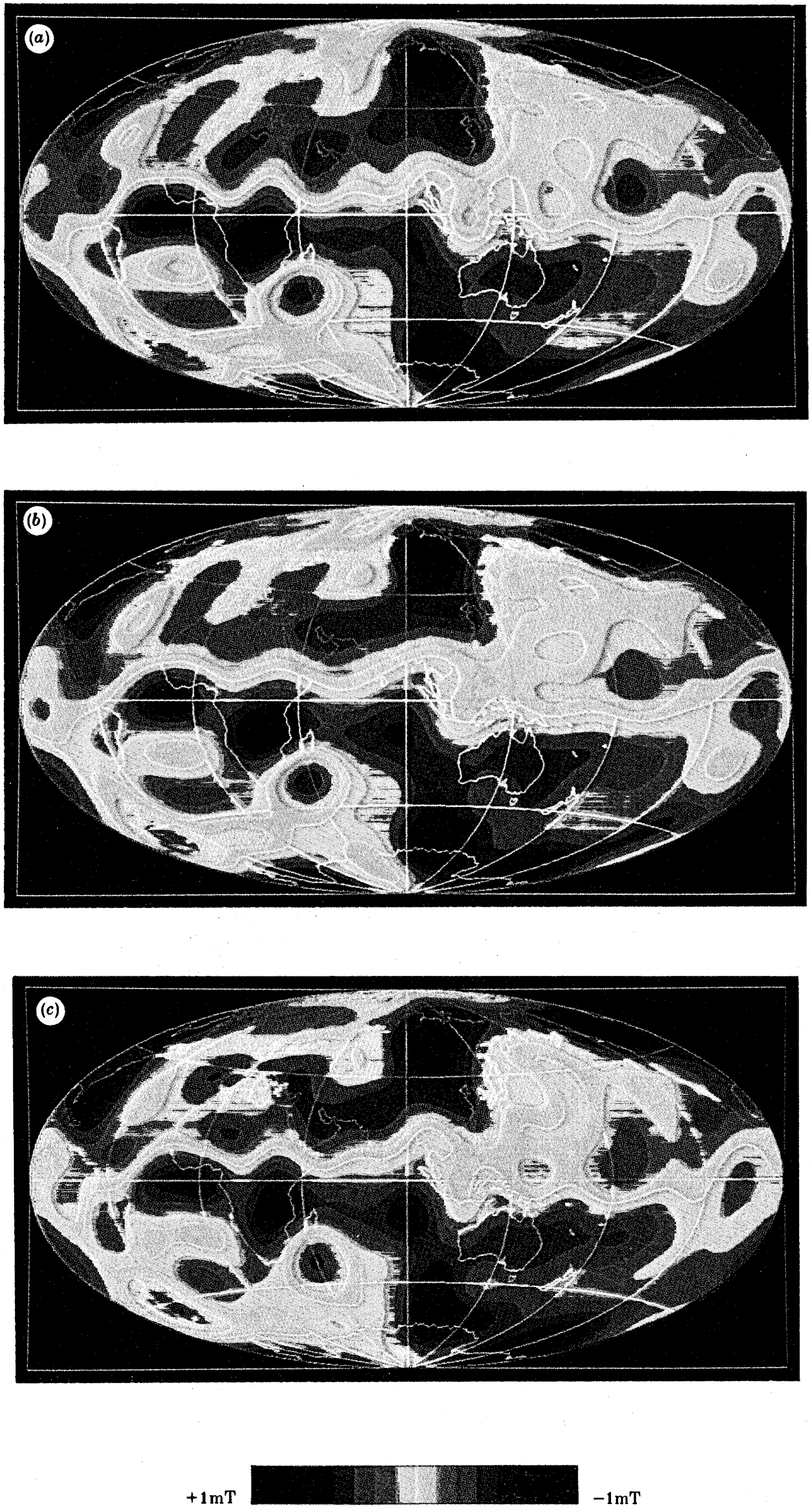

Figure 19 *a*, *b*, *c*. For description see opposite

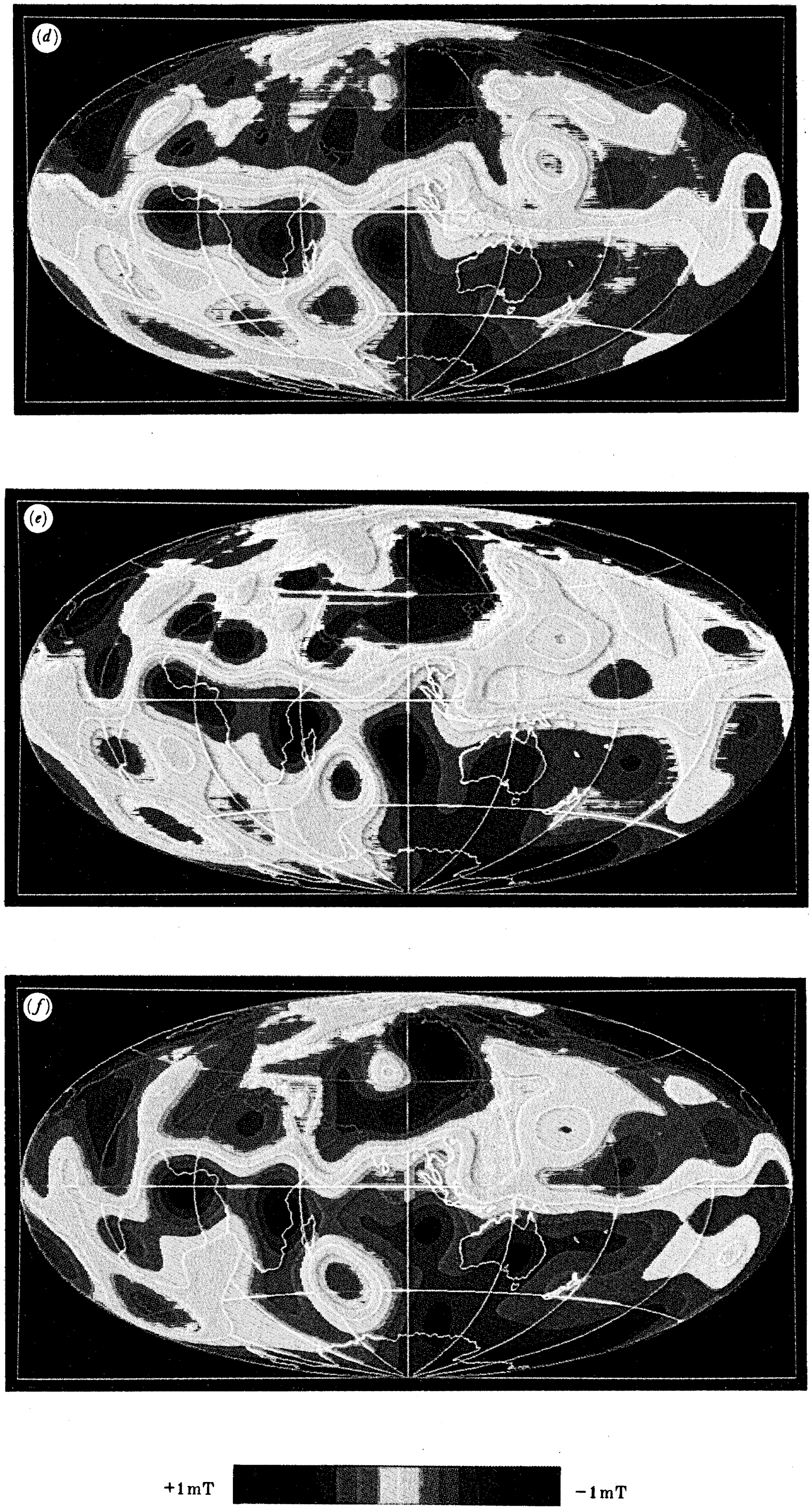

FIGURE 19 *d*, *e*, *f*. For description see facing plate 1.

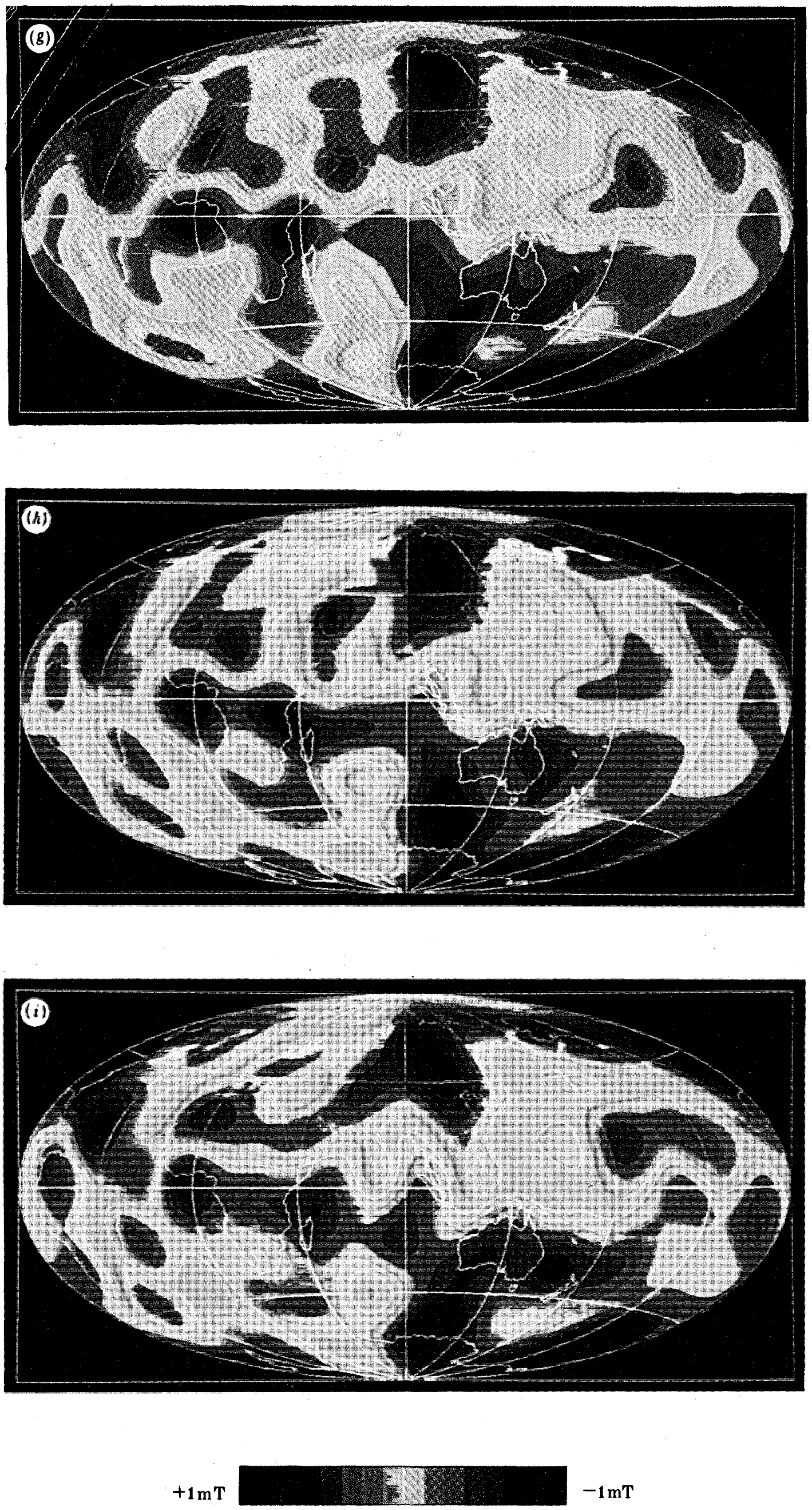

FIGURE 19 *g*, *h*, *i*. For description see facing plate 1.

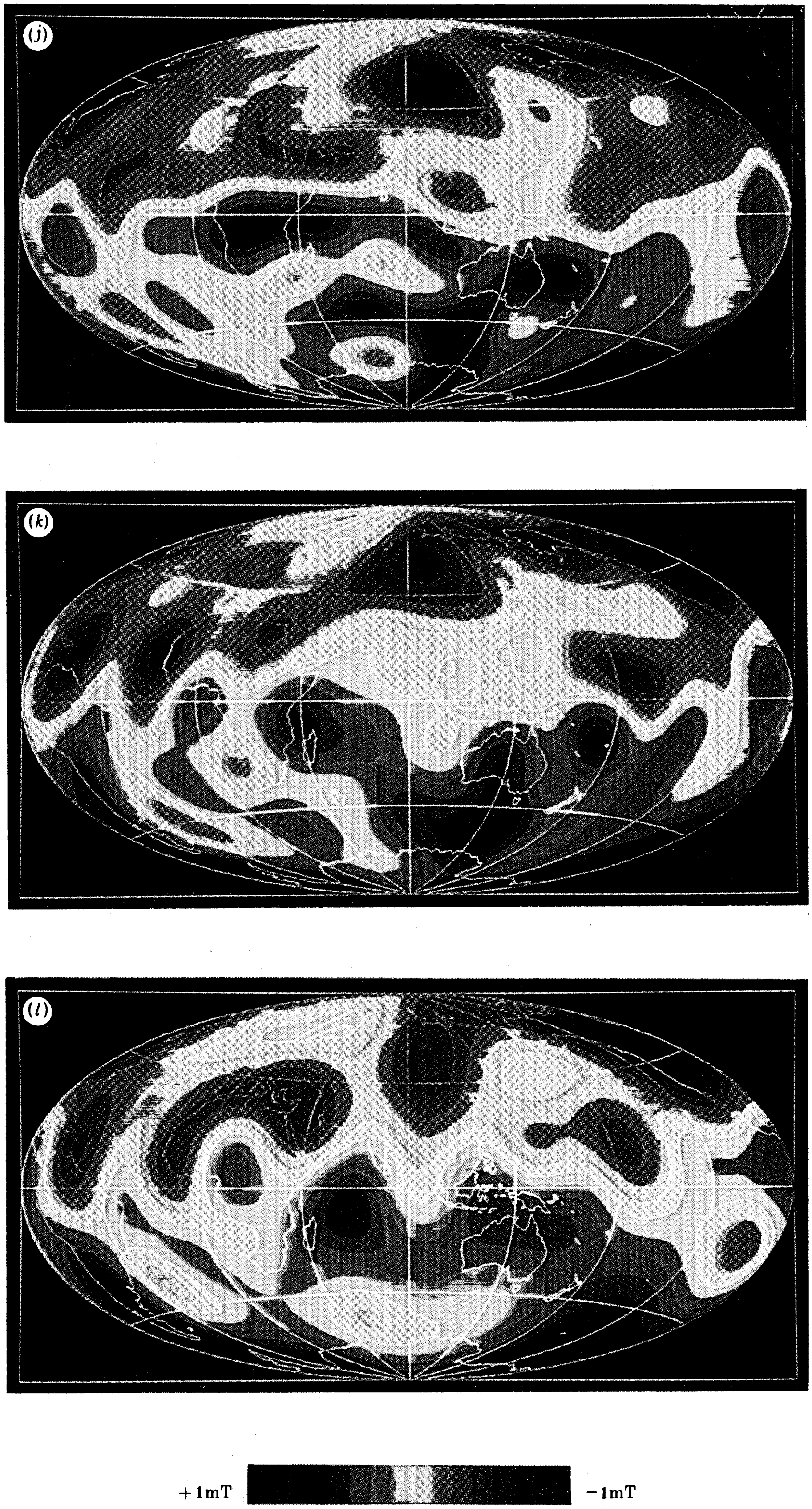

FIGURE 19 *j*, *k*, *l*. For description see facing plate 1.

used by Barraclough (1974). These two norms are smaller; the poorer data quality led to very rough models when the norm was increased beyond these values.

The misfit column would read 1.00 if the data are normally distributed and weighted correctly. As stated in §3, the overall weighting is less important than the relative weights given to different data types. For example the *POGO* data contributing to the 1966.0 model were somewhat over-weighted, giving a high value of the misfit. Changing all the weights by the same ratio has no effect other than changing the calculated misfit and the corresponding value of the damping parameter. (Referring to equations (3.12)–(3.15) it is easy to see that a constant scaling of both C_e^{-1} and λ will leave the model $\hat{m}$ and resolution matrix R unchanged; the covariance matrix C is also unchanged because of the associated change in $\hat{\sigma}^2$, the misfit. In (3.14) only C_e^{-1} changes whereas D and $\mathrm{tr}(R)$ remain constant.)

Column 5, entitled 'resolution', contains the sum of the diagonal elements of the resolution matrix for each model. It reflects the overall quality of the data-set, being highest for 1980.0 and lowest for 1715.0. 1955.5 has clearly the best data distribution of the twentieth-century ground-based models (figure 12) and 1935.5 the worst, which is reflected in their resolutions. Note that the early twentieth century has good data distribution and high resolution. Both the 1955.5 and 1966.0 models are based on more data than we used for the 1980.0 model (see column 3 of table 3), but either the coverage is poorer (1955.5) or data type is dominated by total intensity (1966.0), giving lower resolution for these models. A conventional spherical harmonic series truncated at degree N has $N(N+2)$ coefficients; taking this to be the number of degrees of freedom and comparing with the resolution in table 4 suggests the 1715.0 model is equivalent to degree 6 or 7 (48 and 63 degrees of freedom respectively) and the 1980.0 model to degree 11 or 12 (143 or 168 degrees of freedom). Such comparisons are dangerous however: the models reported here can contain significant coefficients of degree higher than 12, and even the 1715.0 model shows more detail in the field in certain places on the core–mantle boundary than a truncated degree 8 expansion such as the 1965 IGRF.

4.2. *The magnetic field at the core–mantle boundary*

We present the models by plotting the radial component of magnetic field at the core–mantle boundary in figure 19, plates 1–4, as colour maps, and in figure 20 as contour maps, using the Aitoff equal-area projection, arranged in order of increasing age. In a mathematical sense the maps contain all the information in the models because the radial field determines the magnetic potential throughout the insulating region.

The morphology of the field is described in §5. In the present section we restrict our comments to how the appearance of each map is related to the data distribution and quality. The only connection between models is through the crustal corrections applied to the observatory annual means, which if in error would create the same error in all those models containing that observatory (at most 1882.5–1966.0). Therefore, if we find a feature appearing at one time but not at others, we might attribute it to poor data. On the other hand we can be confident that features appearing in many different models are real.

Consider, for example, the prominent concentration of flux beneath the central Pacific Ocean in figure 20*a*. (This concentration of flux is marked as S3 in figure 25*a*.) It remains stationary in the central Pacific with a strength of 300–400 μT throughout, despite a wide variability in the data distributions (compare figures 1–13 and the position of the Honolulu observatory (HO) in figure 15). It is therefore well-resolved by even the worst data distribution, although we cannot prove it to be of core rather than crustal origin.

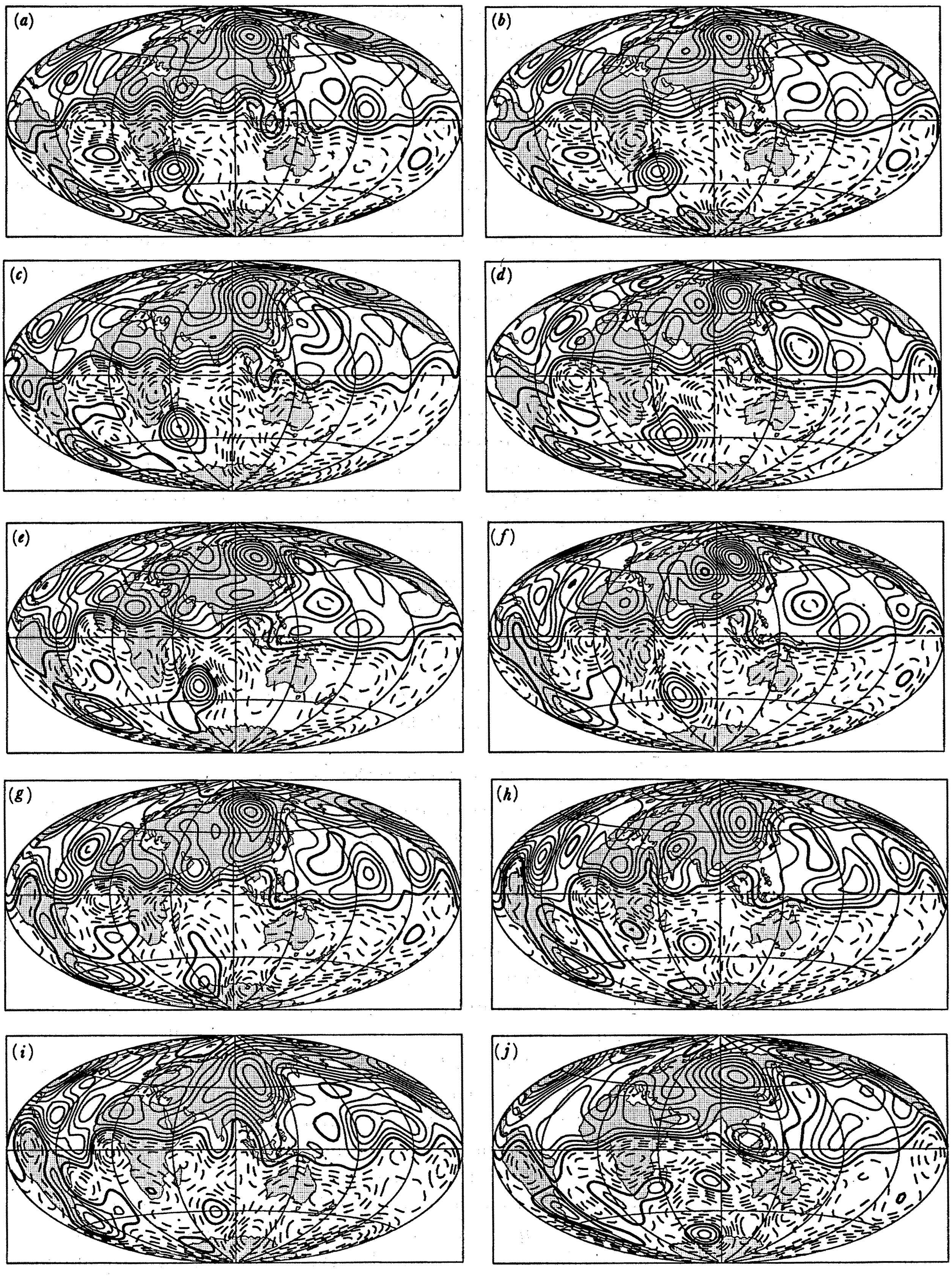

Figure 20*a–j*. For description see opposite.

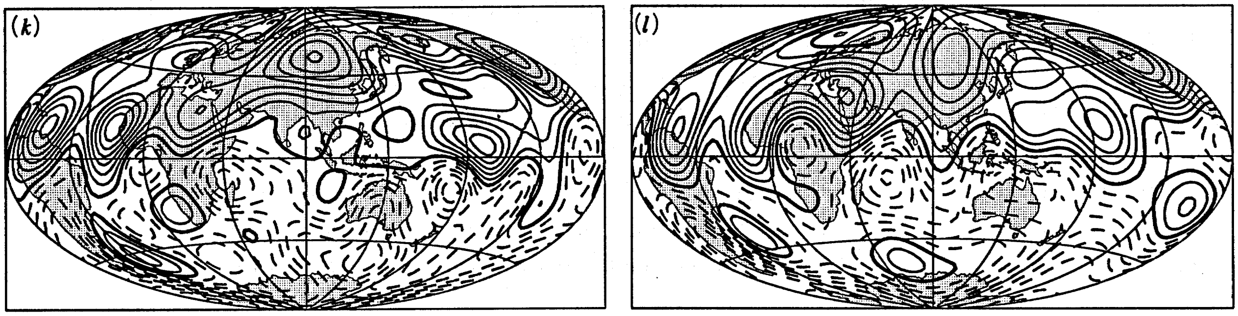

Figure 20. Maps of the radial component of the magnetic field at the core–mantle boundary. The solid lines are negative contours, the broken lines positive contours, and the bold lines zero contours. The contour interval is 100 μT. The map projection is Aitoff equal-area. (*a*) 1980.0; (*b*) 1966.0; (*c*) 1955.5; (*d*) 1945.5; (*e*) 1935.5; (*f*) 1925.5; (*g*) 1915.5; (*h*) 1905.5; (*i*) 1882.5; (*j*) 1842.5; (*k*) 1777.5; and (*l*) 1715.0.

Beneath Easter Island we can identify in figure 20*a* a weak patch of flux bounded by a null-flux curve. It appears as a small null-flux curve in the same position in 1980.0, 1966.0, 1925.5, 1915.5, 1842.5, 1777.5 and 1715.0; a weaker feature is suggested by a bend in the magnetic equator in 1945.5, by a −100 μT contour in 1935.5, and deformation of the −100 μT contour in 1905.5. Comparing with the maps in figures 1–13 we find the data coverage to be quite good in this area for the historical models 1915.5 and 1925.5, very bad in 1935.5 and 1945.5 and rather poor in 1905.5. There is a hole in the data distribution at this location in 1955.5, which perhaps explains its absence (but even so the behaviour of the model is quite poor for this epoch). We conclude this feature is also static throughout but too small to be resolved by the poorer data-sets. It is therefore a good guide to the limit of resolution of this type of data; finding a spurious feature at two different epochs corresponding to good data distributions would be a strange coincidence.

Africa is another region where data are sparse: the coverage is poor there in historical times, in contrast with the oceanic regions where coverage is good in historical times. We can identify westward drifting features in this region: for example, the two small concentrations of flux out of the core just southward of the equator beneath Africa and the mid-Atlantic Ocean. (We identify these features as N2 and N3 in figure 25*a*.) The data distribution over Africa and the western Indian Ocean is poor in 1842.5 (figure 5) and the two features are poorly separated in figure 20*j*; we have identified the weak right-hand member with N3 on the basis of the drift rates (§5). Both features are clearly identifiable in 1882.5, probably because of good coverage in the Red Sea and Indian Ocean.

A similar patch is apparent in 1955.5 (figure 20*c*), beneath Brazil. (Identified as N1 in figure 25*b*.) It has also drifted slowly west from 1842.5 to 1955.5 but it disappears abruptly between 1955.5 and 1966.0. This could be a data problem, such as an anomalous observatory, but several factors mitigate against the interpretation:

(1) the feature was found in both a model for 1955.5 based on observatories alone and another based on survey data alone;

(2) it lies offshore in the South Atlantic ocean in 1842.5 and in 1882.5; the former model has no observatory data, whereas the latter model has no observatory near South America;

(3) it is very weak in the 1960.0 model of Bloxham & Gubbins (1986, figure 1*a*), which contains a great deal of later data from 1960.5–1964.5 in addition to some common with our 1955.5 model.

A more likely explanation is in terms of an effect of variable smoothing, caused by damping in the models. The −200 μT contour is present in the rough models for 1980.0 and 1969.5 of Gubbins & Bloxham (1985). Then again, it may be a real effect at the very limits of our detection capability; this area is certainly one of high secular variation.

In this subsection, we have concentrated on small features in the field at the core–mantle boundary to assess the accuracy and consistency of the models rather than giving a physical or even phenomenological description of them, which is reserved for the next section. In the main these small, poorly resolved features have been found to be consistent between models, lending encouragement to our interpretation of larger features in the next two sections.

4.3. *A discussion of residuals*

All least squares procedures give high weight to data lying a long way from their expected value. Something must be done to remove them and we have adopted the common procedure of rejecting data further than three standard deviations from the starting model to obtain a more robust solution. The iterative procedure described in §3.2 ensured that we did not reject data until the model had converged quite closely to its final form.

The figures in columns 3 and 4 in table 3 can be used to calculate the proportion of data rejected; it lies between 0% and 5% at the three standard deviation level. Only 0.26% would be rejected at this level if the data were normally distributed, there are therefore many outliers. A proportion of the outliers are clearly blunders in key-punching or recording of the data or site positions. This might provide as much as 1%, although a careful study of the 1955.5 data-set did not reveal as many as this. Blunders do not constitute a serious problem because they are most likely to produce very large errors and will therefore be caught by the rejection process (they are true outliers).

The crustal contribution to the error is likely to give the distribution a long tail. A seamount or volcanic region on land may have a crustal contribution of more than 1000 nT and lie outside our three standard deviation cut-off: our survey data-set may well contain a high proportion of data from such areas because of their inherent geophysical interest, in the case of a volcanic island for example, because they constitute the only land for many miles. These could well contribute the remaining percentage of the rejected data. Any blunders or large crustal errors that lie inside three standard deviations will not affect the results significantly provided they influence only isolated observations (there are too few of them).

Figure 21*a*, *b* shows examples of histograms showing weighted residuals between data and model produced from the data. If the distribution of the 'noise' contaminating the data were truly normal then the plots would appear as gaussian distributions with mean zero. Most of the histograms are too long-tailed for the distribution to be gaussian; in fact many are closer to exponential distributions, and some do not have mean zero.

In the same way that it is impossible to separate the core field from the crustal field on the basis of the data alone, it is impossible to infer the distribution of errors on the basis of residuals from a model: the data have already been used in the production of the model, and the resulting distribution will depend on the method of production of the model. If, as is suggested from the histograms, the error distribution is more nearly exponential than normal, then the correct error norm to minimize would be the L_1 norm (minimize sum of absolute weighted residuals), rather than the L_2 norm implemented here (see, for example, Menke 1984). This would give even less weight to the 'tails', and we would expect the resulting histogram to become even more exponential. This illustrates the fact that the correct choice of error norm to be minimized cannot be determined by mere inspection of the residual distribution, because

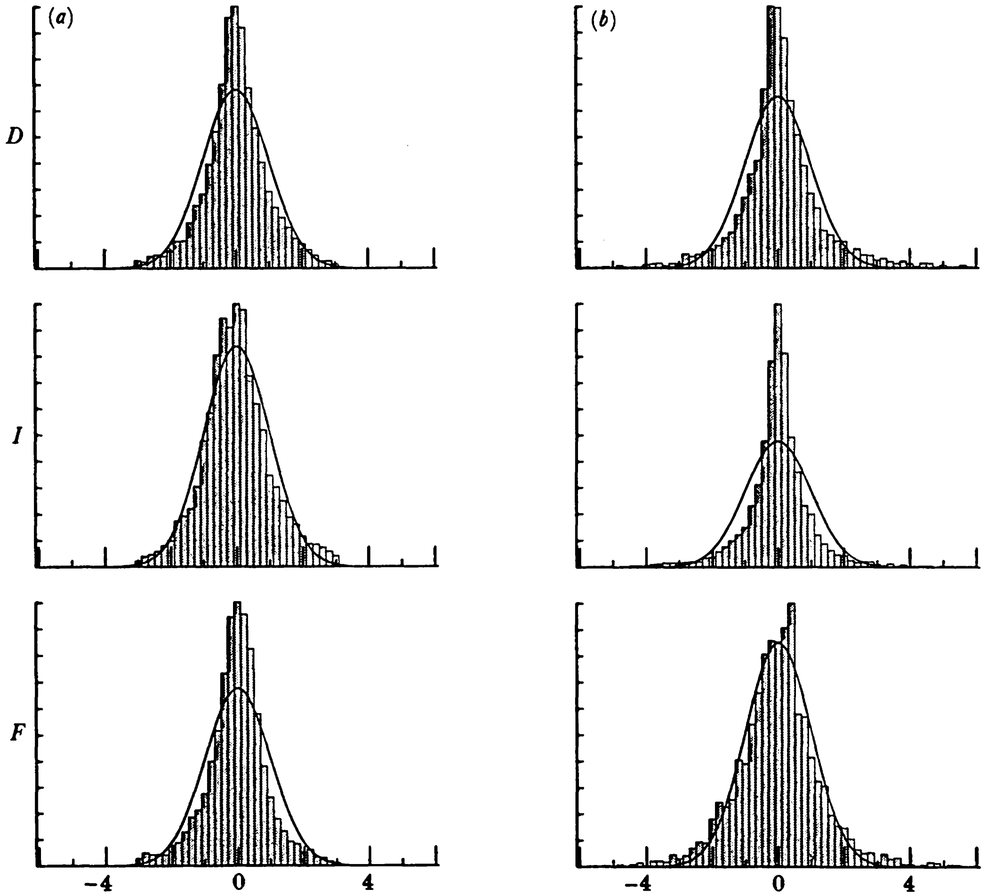

Figure 21. Histogram of residuals of (*a*) 1925.5 field model to 1925.5 data-set; and (*b*) 1842.5 field model to 1842.5 data-set. Plotted are the relative number of observations falling into each $\frac{1}{8}\sigma$ bin. The box heights have been normalized to the height of the largest bin. The continuous curve shows the distribution of residuals expected from a normal distribution.

this in turn depends on the method of construction of the model. Some other information, based perhaps on physical arguments regarding the production of crustal magnetization and magnetic storms, must be used.

The L_1 norm is implemented by using linear programming (LP) techniques. It is, however, computationally more expensive, and in this problem would be difficult to implement. In our application the resulting model covariances are easy to interpret; this is not the case in LP. We have attempted to make our solution robust by rejection of residuals at the three standard deviation level (this should be sufficient to alay the problem of outliers). Data adaptive methods of parameter estimation exist, such as iteratively reweighted least-squares estimation. Such techniques have been used successfully in small studies such as the estimation of power spectra (for example, Chave *et al.* 1987), but are unsuited to large computing tasks such as the one considered here.

4.4. *Error analysis on the core–mantle boundary*

We calculated the error in the radial field at the core–mantle boundary from the covariance matrix, as described by Gubbins (1983), as a quadratic form. If the radial field is expanded in terms of the model parameters as

$$B_r = \boldsymbol{a}\cdot\boldsymbol{m}, \qquad (4.2)$$

then its variance is

$$\mathrm{var}\,(B_r) = \boldsymbol{a}^{\mathrm{T}}C\boldsymbol{a}, \tag{4.3}$$

plus an additional asymptotic part, associated with coefficients of degree higher than the truncation point, which we calculated separately. This asymptotic part is independent of position on the core–mantle boundary, because of the form of the prior information.

Typical errors and their range across the core–mantle boundary are given in the last two columns of table 4. They vary from 30 μT for 1980.0, the best model, to nearly 140 μT for 1842.5 and 1945.5, and reflect the quality of each model. These errors are also in agreement with discrepancies between models of different epochs and we therefore take them to be a good guide to the accuracy of the core field maps, despite the reservations expressed about them in §3.4, except for the oldest two models, which have radically different damping constants and artificially small errors. The errors are mapped for three of the models, 1715.0, 1915.5, and 1945.5, in figure 22.

In general, the errors at the CMB reflect the surface data distribution, and the internal consistency of the measurements. The errors vary with position for many of the models by roughly a factor of two, though the errors for some models, such as 1915.5 and those from satellite data, are much more uniform than this. The historical models exhibit by far the greatest geographical variation.

The errors for 1715.0 (figure 22*a*) vary by more than a factor of two, from minimum in the North Atlantic to maximum in the South Pacific, the area of least data. For 1777.5 the excellent data distribution produces more consistent errors, the maximum being near the pole in the South Atlantic. Errors in 1842.5 also vary little; those in the Antarctic are almost as small as in Europe because of the intensive surveying there. The errors increase under Africa from the local value, suggesting our inability to separate the flux bundles N1 and N2 of §4.2 may not be real and may rather be because of the quality of data there. For 1882.5 minima are in Europe and the U.S.A. and the errors increase quickly in the Antarctic (cf. discussion in §2.3). There is also a maximum in the central Pacific, where we experienced difficulty with *Challenger* data.

For the twentieth-century land-based models the errors are generally smallest in Europe. From 1935.5 to 1955.5 the maximum error lies consistently in the South Pacific, near 40° S 130° W. Note, in figure 22*c* for 1945.5, that the errors are considerably larger than those in 1915.5. There was little oceanic data within this period, and this area is probably the furthest from any operating observatory on the globe. Note that the errors in 1945.5 are particularly large; in the South Pacific the error exceeds that in 1715.0. The 1966.0 model is peculiar in having greatest uncertainty at the equator and smallest errors at the poles because the *POGO* satellite measured only field intensity; the sectorial harmonics are the worst resolved and models are susceptible to the perpendicular error effect (Lowes 1975), whereby errors in B_r are largest at the equator. The inclusion of observatory data helps to alleviate this. In contrast, the errors for the 1980.0 model increase towards the poles, because of the use of only Z in high latitudes, as noted by Gubbins & Bloxham (1985).

The two oldest models have a special difficulty because of the lack of intensity data; they have an inherent arbitrary scaling factor. The values in table 4 were calculated using equation (4.1) to scale the dipole term g_1^0. The behaviour of the dipole moment is very uncertain, but its extrapolation is unlikely to be off by more than 10%.

It is possible that these models of the core field are contaminated by long-wavelength crustal

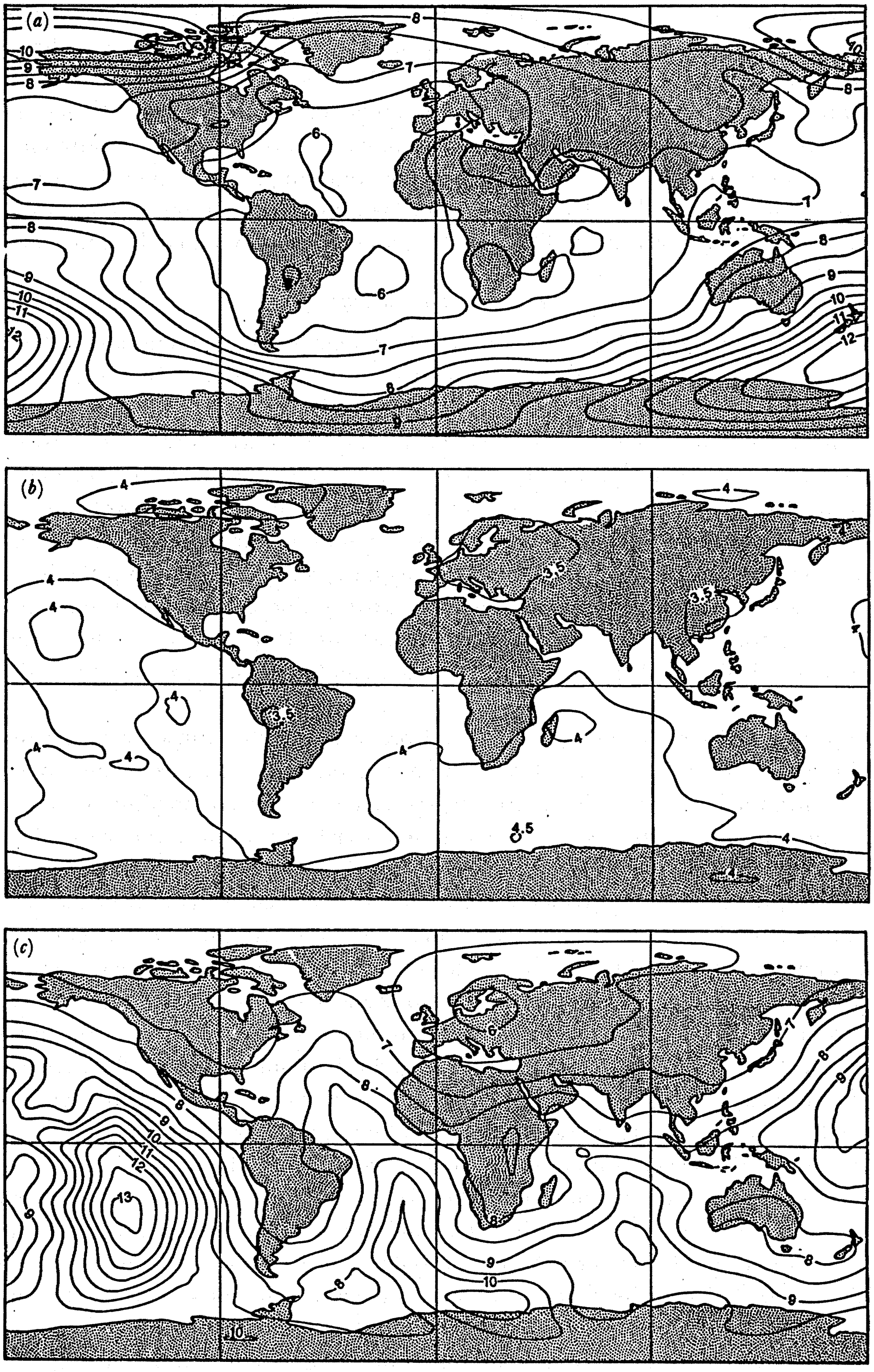

FIGURE 22. Contour maps of errors in the estimated radial field at the core–mantle boundary for (*a*) 1715.0; (*b*) 1915.5; and (*c*) 1945.5. The contour interval is 5 μT; the units are 10 μT, and the projection is Plate Carée. We note in 1715.0 the large errors near the poles owing to paucity of high-latitude data; in 1915.5 the generally very even errors owing to a good data distribution; and in 1945.5 the large errors beneath the eastern Pacific ocean owing to sparse data in that region. The errors shown in (*a*) are relative errors because of the absence of intensity data.

fields. As a fairly crude test for such contamination, we subtracted the global crustal field model CRST-70-F-22-22- of Hahn *et al.* (1984) from the 1980.0 data, and analysed the resulting amended data in the same manner as the original 1980.0 data. We found the resulting model (with damping parameter $\lambda = 10^{-11}$) to be very similar to the original model: the root mean square (r.m.s.) difference in the radial field at the core–mantle boundary between the two models was approximately 2%; not surprisingly, the resulting maps of the field were found to be virtually indistinguishable. This indicates that, within the limitations of the crustal model used, our core-field models are unlikely to be seriously contaminated by long-wavelength crustal fields.

4.5. *Resolution analysis*

In the previous subsection we have discussed the problem of model uniqueness. How broad is the domain of geophysically acceptable models that fit the data? In this subsection we address the different but closely related problem of resolution. We seek to determine how sensitive our models are to changes in the *a priori* damping. This information is given by the resolution matrix. If we had continuous data, i.e. we were somehow able to measure the magnetic field everywhere at the Earth's surface, and if we ignore the problems posed by crustal fields, then the resolution matrix would be an infinite dimensional identity matrix. In practice, as we have discussed, our data are inadequate, and we must damp the inversion to obtain stable solutions. This gives the resolution matrix a different form. We consider first the resolution of particular spherical harmonic coefficients. It is instructive to examine the resolution of particular coefficients, as it provides a useful tool for interpreting the inadequacies of our data.

The top left-hand corner (up to degree and order 10) of the transpose of the resolution matrix for epoch 1966.0 is shown in figure 23*a* as a perspective view, from the top left, of an array of prisms, the height of which represents the value of the corresponding matrix element. We show the transpose of the resolution matrix in order to reveal the structure of the matrix, which is not symmetric, more clearly. Each row of the resolution matrix runs horizontally across the plot, with the rows corresponding to low degree coefficients nearest the viewer, i.e. at the bottom of the picture. The first element has unit height. The diagonal element corresponding to the first dipole (g_1^0) coefficient is in the lower-left corner. The diagonal element in the upper-right corner corresponds to coefficient number 120, h_{10}^{10}.

The expected value of the model estimate is the product of the resolution matrix and the true model vector. One row of the resolution matrix gives the resolving kernel for that particular coefficient. The expected value of the estimate is the scalar product of that row with the true model vector. By examining rows of the resolution matrix we can see that low degree coefficients are well resolved from other low degree coefficients (the matrix is nearly diagonal at low degree), but the separation from higher degree coefficients is less good. Of course, we could fit the data, but not necessarily the *a priori* information, with a model with all low degree coefficients up to some degree set to zero, and only high degree coefficients having non-zero values. At very high degree (beyond that shown in the plot), the rows of the resolution matrix are all zero showing that we have no resolution here.

The diagonal elements are very close to unity out to coefficient number 80 (h_8^8). At higher degree the diagonal elements fall below unity for the coefficients g_9^9, h_9^9, and g_{10}^m, h_{10}^m, where $m \gtrsim 8$. The tesseral harmonics are poorly resolved. This is because the 1966.0 data-set contained a large amount of total field data from the *POGO* satellite. It is well known that total field data does not resolve tesseral terms well because of the Backus effect (Backus 1974) and it is satisfying to see the effect in the resolution matrix. The diagonal elements for higher terms fall off with increasing order for the same degree, then rise for the first (zonal) harmonic of the next degree.

The resolution matrix for 1842.5 is shown in figure 23*b*. Clearly, the resolution is poorer than in 1966.0, with a significant fall in the diagonal elements starting at degree 6 rather than degree 9. The high-order coefficients are very poorly resolved, with some of the off-diagonal terms at degree 10 approaching 0.5. The diagonal elements deteriorate with increasing spherical harmonic degree, forming blocks of roughly equal value corresponding to coefficients of similar degree. Within each block the resolution improves with increasing order, in complete contrast to the 1966.0 model. This results from a dominance of declination data in 1842.5. Declination measurements determine tesseral harmonics very well (because these functions vary rapidly in longitude and therefore produce a big effect on the declination measurements), and zonal harmonics very poorly.

The resolution matrix for 1715.0, shown in figure 23*c*, tells a similar story to that for 1842.5. The resolution is generally poorer, with some of the off-diagonal elements exceeding unity. The pattern of diagonal elements increasing with order within a block of the same degree is exaggerated here because the data-set is even more dependent on declination measurements. There were no intensity measurements and it was necessary to scale the dipole arbitrarily; this gives a resolution of unity (identically) for the coefficient g_1^0.

The resolution matrix also enables us to determine how well we resolve the field at the core–mantle boundary. Following Backus & Gilbert (1967, 1968, 1970) and Whaler & Gubbins (1981) we write the expected value of the estimate $\hat{B}_r$ of the true field B_r at the point (θ_0, ϕ_0) in the form

$$\hat{B}_r(\theta_0, \phi_0) = \oint_{\text{CMB}} A(\theta, \phi; \theta_0, \phi_0)\, B_r(\theta, \phi)\, \mathrm{d}\Omega. \tag{4.4}$$

The expected value of the estimated field is a spatial average of the true field, weighted with an averaging function $A(\theta, \phi; \theta_0, \phi_0)$. After some algebra we can obtain $A(\theta, \phi; \theta_0, \phi_0)$ in terms of the resolution matrix and sums of spherical harmonics,

$$A(\theta, \phi; \theta_0, \phi_0) = \boldsymbol{c}^{\mathrm{T}}(\theta_0, \phi_0)\, R\boldsymbol{b}(\theta, \phi), \tag{4.5}$$

where $\boldsymbol{b}$ has elements of the form

$$(1/4\pi)\, (c/a)^{l+2}\, ((2l+1)/(l+1))\, P_l^m\, (\cos\theta) \cos m\phi,$$

and $\boldsymbol{c}$ has elements of the form

$$(a/c)^{l+2}\, (l+1)\, P_l^m\, (\cos\theta_0) \cos m\phi_0.$$

In figure 24*a* we plot the averaging function for 1966.0 for the point (50° N, 0° E), and in figure 24*b* for the point (0° N, 180° E). In the ideal case of perfect, continuous data the averaging functions would appear as delta functions. Instead, we see that our estimates depend upon a broader, but none the less well-localized, average of the field. It is worth commenting that the equatorial averaging function in figure 24*b* is a little worse than the high-latitude function in figure 24*a* despite the preponderance of *POGO* data contributing to the model. This is a manifestation of the perpendicular error effect. In figure 24*c*, *d* we show the averaging function for 1842.5 centred on (50° N, 0° E) and (40° S, 170° E) respectively. Although the

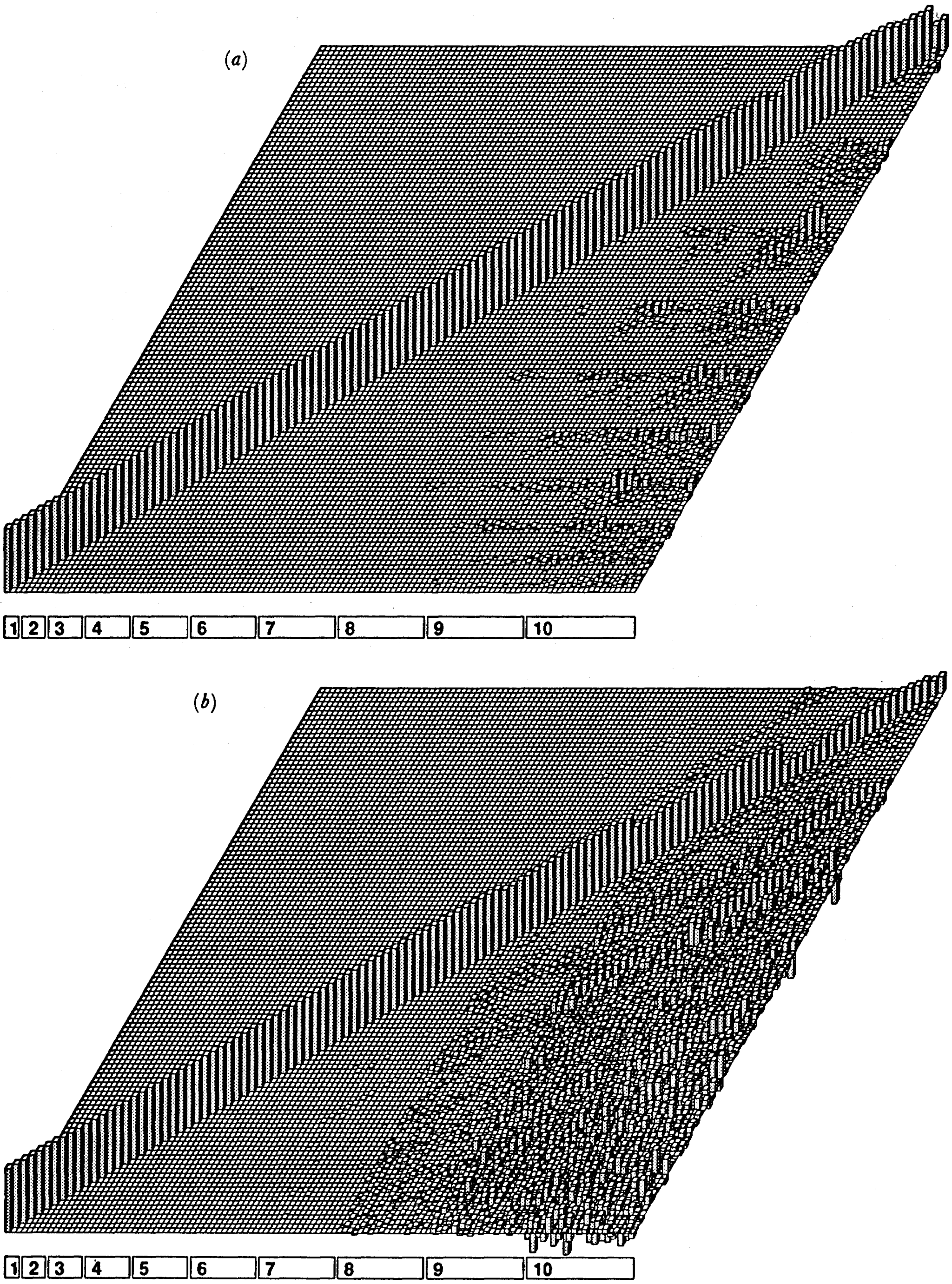

FIGURE 23*a*, *b*. For description see opposite.

peaks are now somewhat broader owing to the lower resolving power of the data, we note that our inversion scheme is still providing well-localized averages. In figure 24*e*, *f* we show the averaging function for 1715.0, again centred on (50° N, 0° E) and (40° S, 170° E). We still have a well-localized average beneath Europe (where the data distribution for 1715.0 is at its best), but a very much poorer averaging function beneath the southwest Pacific Ocean (where there is no datum for 1715.0).

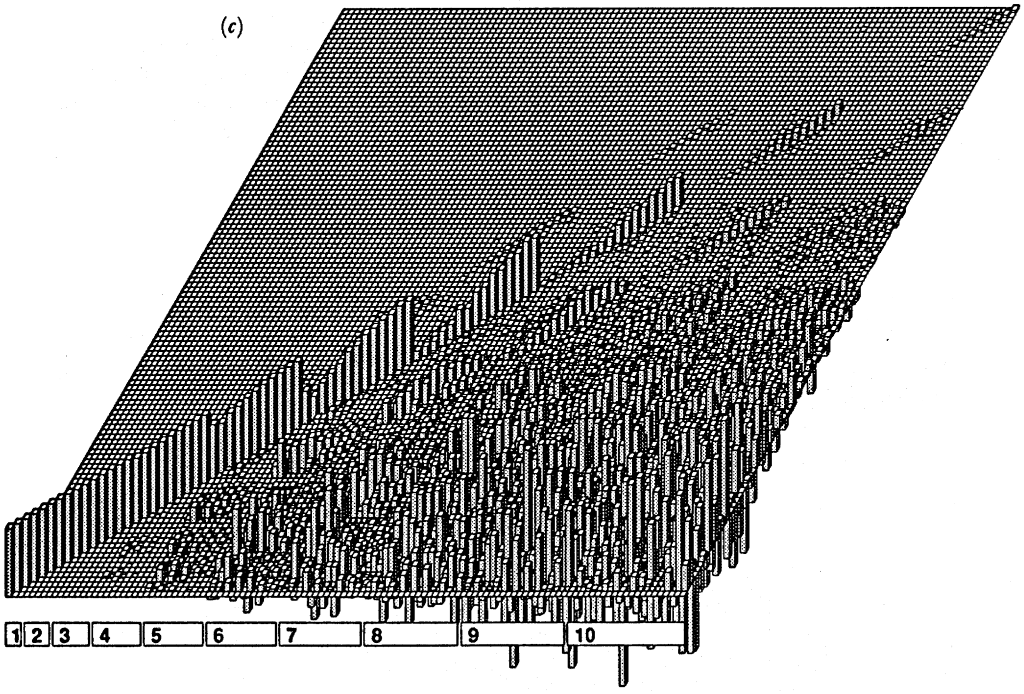

FIGURE 23. Schematic representation of transpose of the resolution matrix for: (*a*) 1966.0; (*b*) 1842.5; and (*c*) 1715.0. The first element of the matrix is in the lower left-hand corner of the plot. The scale along the lower edge shows the corresponding spherical harmonic degree of the columns of the matrix; within each degree the elements are ordered by spherical harmonic order, with cosine (real) terms preceding sine (imaginary) terms within each degree and order. With this representation the first row of the resolution matrix is along the lower edge of the plot.

For comparison, in figure 24*g*, *h* we show the averaging functions corresponding to simple truncations of the spherical harmonic expansion at degrees 8 and 4. Even at degree 8 we see that the average is much more poorly localized: our 1715.0 model is clearly providing better resolution of the field beneath Europe than could be obtained by a degree 8 representation, regardless of the data contributing to the degree 8 model. Compared with a degree 4 truncation (the truncation point used most commonly in previous studies of the historical field) the superiority of our inversion technique is indisputable.

These plots demonstrate that our new inversion technique has largely solved one of the fundamental problems with truncated spherical harmonic inversions. The averaging functions in figure 24*a–f* show much less evidence of ringing than their counterparts in figure 24*g*, *h*. We have indeed succeeded in constructing maps of the field that are largely free from the effects of ringing.

5. PHENOMENOLOGICAL DESCRIPTION OF THE CORE FIELD AND ITS CHANGES

5.1. *Characterization of features*

If the Earth's field were a simple axial dipole then contours of its radial component would be latitude circles, the zero contour would be on the Equator, and extrema would be at the poles. Contour plots such as those in figure 20 would appear as latitude lines. We can describe 'features' of the core field as departures from this expected dipole state. Most of the features

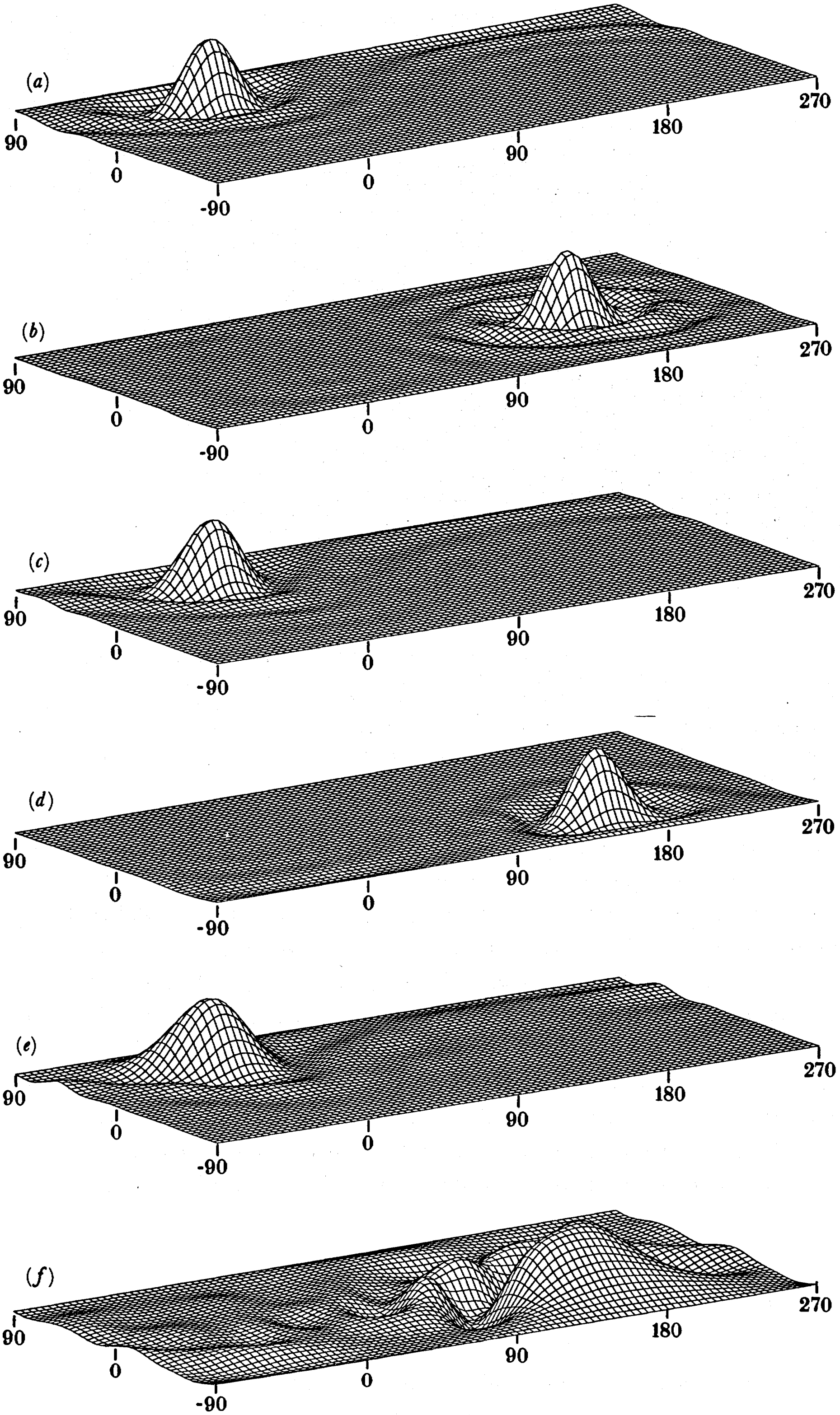

FIGURE 24*a–f*. For description see opposite.

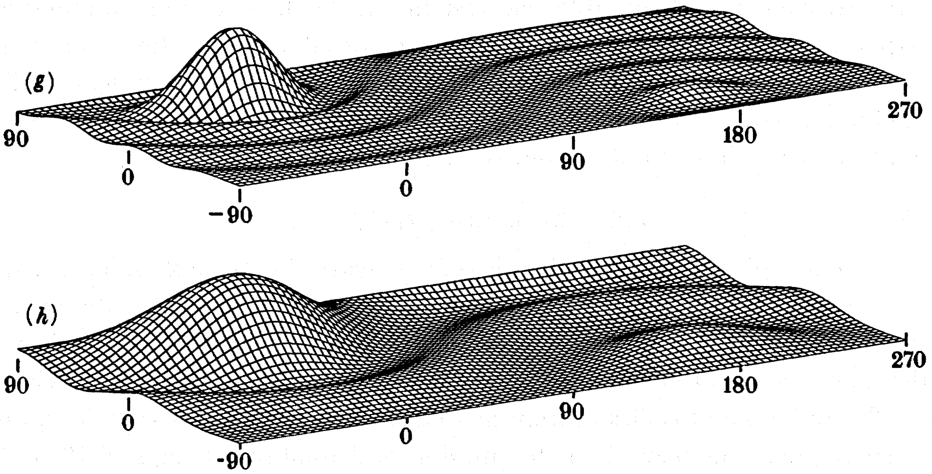

FIGURE 24. Maps of averaging functions of the radial field at the core–mantle boundary: (*a*) 1966.0 centred on (50° N, 0° E); (*b*) 1966.0 centred on (0° N, 180° E); (*c*) 1842.5 centred on (50° N, 0° E); (*d*) 1842.5 centred on (40° S, 170° E); (*e*) 1715.0 centred on (50° N, 0° E); (*f*) 1715.0 centred on (40° S, 170° E); (*g*) degree 8 spherical harmonic expansion centred on (50° N, 0° E); and (*h*) degree 4 spherical harmonic expansion centred on (50° N, 0° E).

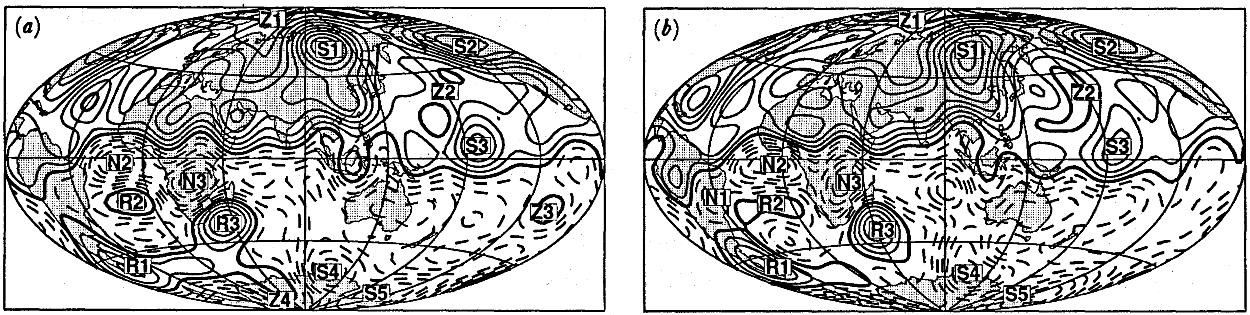

FIGURE 25. Copies of figure 20*a* (1980.0) and 20*b* (1955.5), *a* and *b* respectively, showing maps of the radial component of the magnetic field at the core–mantle boundary, with key features in the field labelled with two character codes. Static features are labelled S1–5, normal-signed features N1–3, reversed-sign features R1–3, and zero flux features Z1–4. These features are referred to throughout §5.

identified in figure 25*a*, for 1980.0, and figure 25*b*, for 1955.5, are either concentrations of flux into areas one or two thousand kilometres across, or similar-sized regions of near-zero field.

We follow the characterization of features given by Bloxham & Gubbins (1985) and describe their evolution in each case. Flux bundles or spots are regions of high field marked as S (for static), N (for normal), and R (for reversed), in figure 25*a*. Patches of persistant low flux are marked Z (for zero-flux). The long time-span of this data-set allows us to discriminate quite easily between stationary (S and Z), and moving (N and R) features. In 265 years the latter have drifted by as much as 60° in longitude but the former have shown no persistent movement.

The moving features marked R have field in the reverse direction to that expected from a dipole; in 1980.0 they are mainly in the South Atlantic region. Some of the R and N features may be coupled, so that field lines emerging from N3, for example, re-enter at R3. We call such features 'spots' by analogy with sunspots which are formed by expansion of toroidal flux through the corona (a similar mechanism may be operating in the core (Bloxham 1986*b* and §8)).

This leaves two further identifiable features in the field. The large undulation in the magnetic equator beneath Indonesia is a region of rapid change, the oscillations do not propagate despite their wave-like appearance. They were called localized field oscillations by Bloxham & Gubbins (1985). The undulation in the magnetic equator under the Amazon basin behaves in a somewhat similar fashion but is longer wavelength.

5.2. *The stationary field pattern*

A very persistent aspect of the core field is shown clearly in figure 25*a*. The field over the North Pole is low; the zero flux patch Z1 persists throughout our models. A dipole field would achieve maximum intensity at the poles, and yet the Earth's field is near zero there. Feature Z4, near the South Pole, is less convincingly permanent. It merges with the moving, reverse-flux features R1 and R3 and is absent from models such as 1955.5 and 1935.5 (figure 20*c*, *e*), arguably a consequence of poor data distribution and quality (cf. figures 10 and 12). Its reappearance in 1905.5, 1842.5, and perhaps 1715.0, is evidence for a permanent low in the region. Therefore we suspect a symmetry in the static field: low radial field exists near, but not precisely at, both polar regions.

The dominant features in the field are the static ones S1 and S2 in the Northern Hemisphere, and corresponding highs S4 and S5 in the Southern Hemisphere. We call these four the 'main lobes' of the core field; they remain static although S4 and S5 become indistinct in some older models such as 1715.0. This again we attribute to poor data distribution. These main lobes change somewhat with time, but they do not drift persistently. For example, S2 is split in 1842.5, with the larger maximum considerably eastwards of its position in 1980.0. This could be a combination of a drifting feature, perhaps associated with the polar wave (§5.4), passing through the stationary high.

A study of the change in the feature around 1842.5 suggests such an effect: the location of the greatest maximum moves east from 1715.0 to 1905.5, then west again, with the secondary high reaching a peak at the time of greatest eastward displacement.

Lobe S5 has shifted to the west slightly in recent times but its appearance in almost the same position in 1842.5 (and other models) shows it to be fundamentally different from drifting features. Its present movement is probably because of the proximity of the large reverse-flux feature R1, which has moved westward and displaced it.

The central Pacific flux concentration, S3, has been remarkably stable for the entire span of our data. It appears to be similar in size and shape to the moving flux bundles N1, N2, etc., but quite different in its temporal evolution. It is flanked to the north and northwest by a large stable region of low flux Z2. Secular variation is not completely absent from the Pacific region however: the area to the east of S3 shows persistent small changes to both north and south of the magnetic equator (which are responsible, incidentally, for the secular variation observed at Honolulu Observatory).

The Easter Island null flux curve, Z3, is another most persistent feature of all our models. Data coverage is quite good in this remote part of the Pacific in historical times but is rather poor in the twentieth century before the advent of satellites; it is absent from the 1945.5 and some other models, almost certainly because of poor data coverage (cf. figure 11). Again, there is significant secular variation to the east of the feature, and also to the south and west.

Ideally, we would like to separate the stationary part of the field by time-averaging all our models. Unfortunately, as we showed above, even a time interval as large as the 265 years spanned by the models in this paper is insufficiently long for time-averaging to remove all of the drifting and time-dependent features. We must be content with an 'eyeball' average of the field. The stationary field then appears as four main lobes in the Pacific hemisphere near latitudes 65° N and 65° S, and longitudes 120° E and W, with a smaller concentration of flux near the Equator southwest of Hawaii (S3). Flux in the North Pacific region is low but secular variation prevents us from deriving an accurate picture of the mean field elsewhere. This steady field is antisymmetric about the equator; the main lobes S1, S2, S4, and S5 appear as pairs on similar longitudes. The antisymmetry is much less apparent in individual field models because drifting features dominate the picture; they also prevent any apparent antisymmetry appearing in the geomagnetic coefficients. We comment further on this antisymmetry in §8. The mid-Pacific flux bundle, S3, does not satisfy this antisymmetry; it is almost symmetric about the equator.

Yukutake & Tachinaka (1969) have already found that a representation in terms of standing and drifting harmonic coefficients was a better representation of the secular variation than a simple westward drift. They performed a formal separation of the geomagnetic coefficients up to degree and order 6 and it is interesting to compare their representation for the standing field at the core–mantle boundary with our own identification of stationary core features. The coefficients for the standing field published by Yukutake & Tachinaka (1969) omitted values for the zonal harmonics (these were calculated by averaging all the contributing field models they used). The resulting complete set of geomagnetic coefficients were then used to plot the radial component of field at the core–mantle boundary, as shown in figure 26.

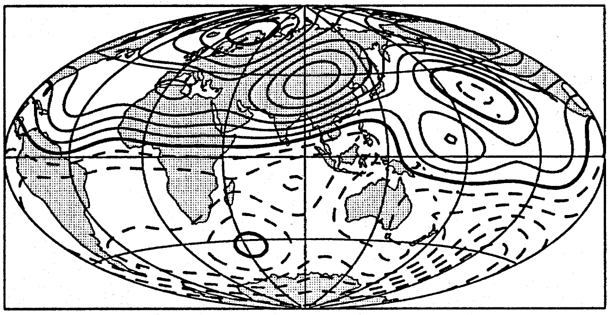

FIGURE 26. Map of the radial component of the magnetic field at the core–mantle boundary (contouring, projection, etc., as figure 20) based on the standing part of the standing or drifting field model of Yukutake & Tachinaka (1969). We have added zonal terms to their model, as described in the text.

The representation is only to degree and order six and is therefore rather smoother than those presented in §4. However, some of the main features are present, notably the zero-flux patch Z1 near the North Pole, the static flux patches S1, S2, S3, S5, but not the static flux patch S4. The low flux in the North Pacific is well represented, but the region of low flux off southern Africa remains: this we would regard as a moving feature and obviously the time span of a few hundred years is insufficiently long to average it out. The moving reverse flux patch R1 is also absent, although this is probably due more to the high truncation of the spherical harmonic series and poorer data quality of the models than the time averaging (truncating some of our own models at degree and order 6 removes this patch). We conclude that this previous study is in good general agreement with our analysis.

5.3. *The westward drift*

The westward drift was recognized by Halley (1683, 1692). Later, Halley surveyed the Atlantic Ocean, where the drift is most prominent. Declination plots for some of our models are shown in figure 27. They show westward drift in the Atlantic but little change in the Pacific, and eastward drift over parts of Asia. Westward drift is not therefore a global phenomenon, and had Halley sailed in the Pacific Ocean, rather than the Atlantic, it might not have assumed such prominence in the subject.

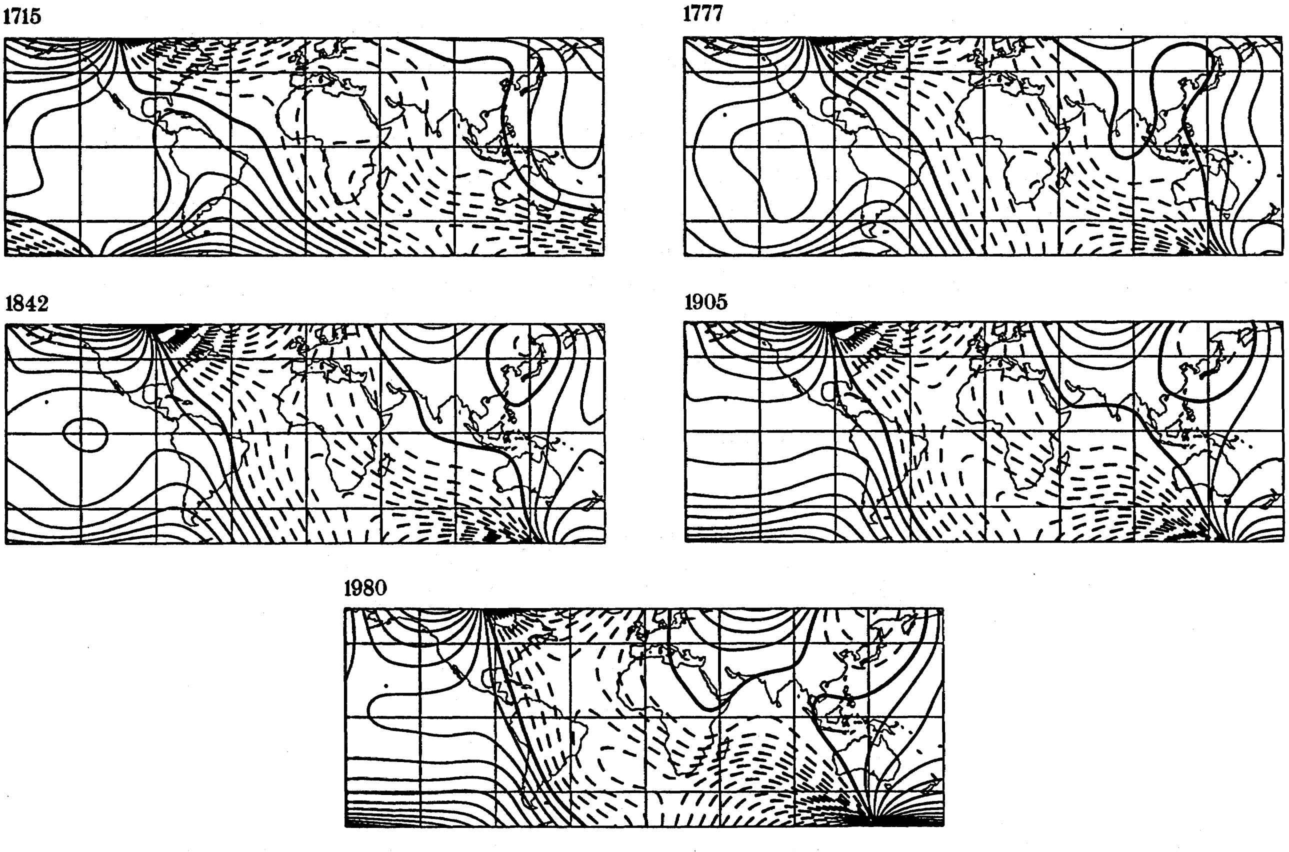

FIGURE 27. Maps of the declination at the Earth's surface calculated from our field models at approximately 60-year intervals from 1715 to 1980. Solid contours represent east declination, broken contours west declination, and bold contours zero declination. Contour interval is 5°.

We can make a number of simple observations from the maps of radial core fields in figure 20. Almost all the moving features in the radial field at the core–mantle boundary drift westwards rather than eastwards. The exception to this rule is around the main lobe S2, where the flux bundle appears split in two in the nineteenth and early twentieth centuries, and the easternmost part appears to move eastwards over northern Canada. However, this pattern may be alternatively interpreted as westward movement of a low in field intensity through a static feature, or east–west fluid motion stretching the static flux bundle. There is therefore no direct evidence of eastward motion at the core–mantle boundary; strong azimuthal motions are predominantly westward.

However, a very substantial portion of the core–mantle boundary shows no westward movement at all. This is most noticeable in the North Pacific. Features appear to stop before entering this region, and are initiated to the west of it. There is no indication that westward drift carries features in the field around a full 360° of longitude, as is sometimes supposed (and is implicit in some recent interpretations of, for example, lake sediment records (Creer *et al.* 1983)). The evidence is far more in favour of magnetic field features being initiated near longitude 120° E and drifting west to cease or disappear near longitude 90° W.

We note that a simple westward drifting field pattern is an inadequate model for the secular variation. This does not necessarily contradict previous studies of the westward drift. For example, Bullard *et al.* (1950) excluded the equatorial dipole from the field before determining westward drift rates around latitude circles and so did not determine a simple rotating field configuration. We have already pointed out that Yukutake & Tachinaka (1969) considered combinations of drifting and standing fields, which they were forced to do because of the failure of a simple westward-drifting model. The rapidly drifting features in the South Atlantic region of the core–mantle boundary drift at higher rates than those found by Bullard *et al.* (1950) and others (this is consistent if we recall the latter authors averaged around latitude circles and therefore included the large Pacific region, where there is virtually no drift at all). In fact the widespread belief that westward drift is a rotation of the entire field pattern, as if the core were rotating westward relative to the mantle, has never been justified by the secular variation observations. Taking any recent spherical harmonic model of field and secular variation shows that, whereas some harmonics may be interpreted as drifting individually, the entire field pattern shows only a very slight overall rotation. Our core field maps show something new: that the region of drift is confined to a rather specific part of the core–mantle boundary.

Westward drift, which hereafter we shall use to describe movement of features in the radial field at the core–mantle boundary, is most prominent beneath the South Atlantic, Africa and South America. Consider first the two features marked N2 and N3 in figure 25*a*. These are drifting rapidly and are responsible for the rapid secular change currently observed at the Earth's surface in the central Atlantic and South Africa respectively. A crude estimate of the drift rates is obtained by plotting the longitude of the maximum point of each feature N2 and N3 (table 5). For models from 1882.5 onwards this yields approximate rates of 0.17 deg a^{-1} (N2) and 0.25 deg a^{-1} (N3).

TABLE 5. LONGITUDES OF FIVE OF THE FEATURES MARKED IN FIGURE 25

(Longitudes are in degrees (postive east). A dash indicates the feature could not be identified reliably in that model.)

feature	1980	1966	1955	1945	1935	1925	1915	1905	1882	1842	1777	1715
N1	—	—	−50	−46	−42	−39	−36	−36	−31	−27	—	—
N2	−15	−10	−2	−11	−10	−3	−1	−1	−1	2	—	—
N3	25	32	35	36	45	36	41	39	52	—	—	—
R1	−70	−68	−62	−59	−54	−60	−60	−57	−54	−56	−42	−33
R3	35	41	47	52	60	57	—	69	70	—	—	—

The greatest uncertainty in this method of measuring drift is that change in shape of a feature may lead to spurious movement of the maximum; it is not possible to locate features N2 and N3 with any certainty in the older models. Although we can attempt to identify these features by using average drift rates, we find that such an approach does not yield wholly consistent results. The continuously time-varying mapping described by Bloxham (1987) may be expected to resolve these problems of identification.

Of the reverse flux features, R1 and R3 drift west, whereas R2 shows no persistent movement. Locations of the maxima of R1 and R3 are shown in table 5. R1 suffers considerable change of shape and the location of the maximum varies relative to other contours in the feature. The drift rate for the twentieth-century models averages at 0.21 deg a^{-1}. For earlier models identification is straightforward, giving a drift of about 0.11 deg a^{-1}.

R3 moves very rapidly, at about 0.46 deg a^{-1} in the twentieth century. It has also grown in intensity during that time (Bloxham & Gubbins 1985). This drift rate would be quite large enough to carry the reverse flux patch east of Indonesia in 1777.5 (figure 20*k*) and 1842.5 (figure 20*j*) into its position in 1905.5, a total movement of 73° of longitude in 200 years.

Feature R1 has moved southwards steadily throughout this time, by about 15°, and is continuing to move south today. It is very difficult to identify R3 in historical times because it is very weak and the maximum is ill defined. It appears to have moved south during historical times, but not during the twentieth century.

The magnetic field in the Northern Hemisphere shows less variations and therefore the features are more difficult to identify and track to provide a westward drift rate. However, the series of small features in the North Atlantic and over Europe drift west; motion of the null-flux curve in the Atlantic is apparent even in the final interval between 1966.0 and 1980.0. The rate is very hard to estimate, but again is between 0.15 deg a^{-1} and 0.25 deg a^{-1}.

We conclude from this survey that azimuthal motions at the core surface are predominately westward: the rates vary from 0.1 to 0.5 deg a^{-1}, depending on the feature.

5.4. *The polar wave*

The succession of highs and lows that stretch across the core–mantle boundary beneath Europe and the Atlantic Ocean in 1980 (P1–P5 in figure 28) is very striking when plotted centred on the North Pole. It has the appearance of a wave, centred near the pole, with wave number between 5 and 9. We shall call this feature the mid-latitude polar wave. It has drifted to the west, the best illustration being the recent movement of the small null-flux curve that lies in the central Atlantic in 1980.0. The pattern appears to merge into the main lobes S1 and S2, and may be responsible for the third high which is evident under Alaska in 1775.5–1905.5. This again suggests that the apparent eastward movement of S1 is in fact a manifestation of an eastward-propagating wave passing through it.

The very short wavelength of this feature makes it exceedingly difficult to analyse reliably. Although P1–P4 are clearly distinguishable in the satellite models (figure 20*a*, *b*) and in 1945.5 (figure 20*d*, when an extensive survey of the U.S.S.R. was published giving good data there, see figure 11), they are indistinct and variable in other models. The contours are too variable to follow for an estimate of the westward drift, and we adopted a correlation procedure instead. A correlation coefficient $C_M(t, \omega, \Delta t)$ is defined for a given westward drift rate ω by

$$\left.\begin{aligned} C_M(t,\omega,\Delta t) &= \iint_{S_n} B_r^M(c,\theta,\phi;t)\, B_r^M(c,\theta,\phi-\omega\Delta t; t-\Delta t)\, \mathrm{d}S/N(t), \\ \text{where}\qquad N^2(t) &= \iint_{S_n} [B_r^M(c,\theta,\phi;t)]^2\, \mathrm{d}S \iint [B_r^M(c,\theta,\phi;t-\Delta t)]^2\, \mathrm{d}S, \end{aligned}\right\} \tag{5.1}$$

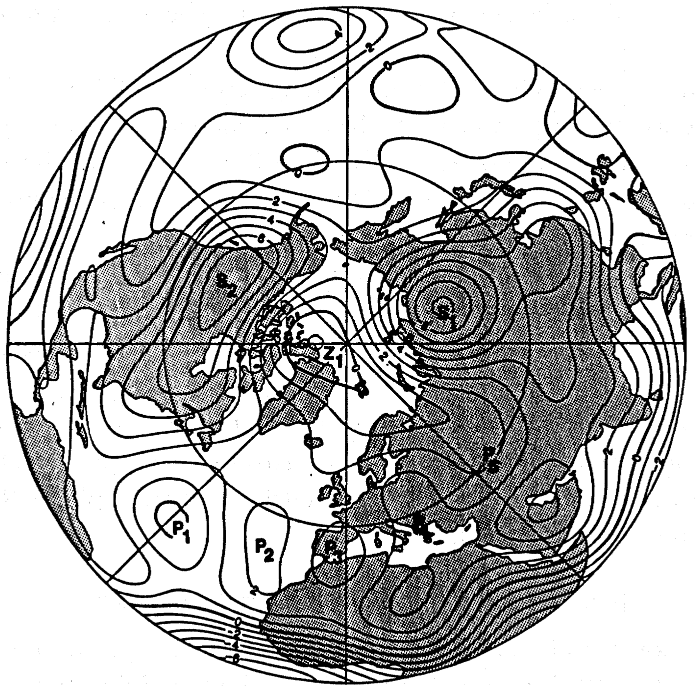

FIGURE 28. North polar view of the radial component of the magnetic field (1980) at the core–mantle boundary, using a Lambert azimuthal equal area projection. The contours are labelled in units of 100 μT. The static features S1 and S2, and the zero flux feature Z1, identified in figure 25*a* are labelled. Also labelled is the wave-like progression P1–5, referred to in the text as the polar wave.

and B_r^M denotes the radial component of magnetic field derived from the spherical harmonic sum (1.4) with $m \geqslant M$, thus excluding long-wavelength features by essentially high-pass filtering in the ϕ-direction. S_n denotes the Northern Hemisphere of the core–mantle boundary. Values of ω were sought which maximized the correlation coefficient C_M.

$M = 5$ was found to give the best results; those with higher values of M were noisy, and those with $M \leqslant 4$ gave a slower drift rate, reflecting the influence of the larger stationary highs. The results are shown in table 6. The very low drifts obtained from 1955.5 to 1966.0 and 1882.5 to 1915.5 are also seen in the lack of movement of the contours during these times. They might

TABLE 6. OPTIMUM WESTWARD DRIFT RATES FOR THE POLAR WAVE

(Each pair of field models are rotated by an angle determined by their difference in time and ω and the correlation coefficient calculated for harmonics with $m > 5(C_5)$; ω is determined by maximizing the correlation coefficient.)

model 1	model 2	ω	C_5
1980.0	1969.5	0.15	0.904
1969.5	1966.0	0.22	0.935
1966.0	1955.5	0.00	0.865
1955.5	1945.5	0.33	0.600
1945.5	1935.5	0.19	0.670
1935.5	1925.5	0.15	0.679
1925.5	1915.5	0.20	0.817
1915.5	1905.5	0.00	0.770
1905.5	1882.5	0.00	0.674
1882.5	1842.5	0.11	0.303
1842.5	1777.5	0.15	0.123
1777.5	1715.0	0.14	0.617

therefore represent a real variation in the drift speed. The mean rate of drift is around 0.15 deg a^{-1}.

We can also obtain a very rough estimate of the long-term rate of drift by identifying features P1–P5 in 1980.0 (figure 28) with those in the historical models (compare figures 28, 20*a*, *i–l*). The centre of P1, the low feature appearing as a null-flux curve in modern times, has drifted at an average rate of 0.18 deg a^{-1} between 1715.0 and 1980.0. Notice also that a second low appears in the Atlantic at 45° W in 1777.5 (figure 20*k*) when P1 is near the Greenwich meridian. This suggests a period of 200 years for the wave and azimuthal wave number 8. However, features P2–P4 drift faster and suggest longer wavelengths. P2 gives 0.20 deg a^{-1} since 1715.0 while P3 and P4 give 0.35 and 0.28 respectively since 1842.5 (they cannot be identified in the earlier models).

We believe this apparent wave in mid-northern latitude may be a manifestation of a magnetohydrodynamic wave, possibly a magnetic Rossby wave (Hide 1966), because of its restriction to mid-latitudes and resemblance to the effect of an atmospheric Rossby wave on the pressure. It will be the subject of further study.

5.5. *Formation and decay of the drifting features*

In the last subsection we observed that westward drifting features are confined between longitudes approximately 120° E and 90° W, whereas the remaining (predominantly Pacific) region is static. It follows that the drifting features originate near 120° E and die away near 90° W. Can we observe this process in action?

The moving feature, N1 (figure 25*b*), is absent from the first two and last two models but is persistent at other times; its reality was discussed in §4.2. From 1882.5 to 1955.5 it drifted west at a mean rate of about 0.28 deg a^{-1} (table 5). Its absence from the earlier models may be a consequence of poor data or misidentification, but its demise after 1955.5 is well documented. It moves progressively westwards throughout the twentieth century and loses its identity in the 1966.0 model (although we note here that a hint of it appears in the 'rough' 1980 model D80513 of Gubbins & Bloxham (1985), indicating that this model may contain more information than the smoother version we have used here). There is no corresponding increase in the flux in the region in the southeast Pacific, northeast of the Easter Island null-flux curve, where we might expect it to appear if it had retained its drift.

Features to the north and south of N1 appear to be deflected towards the main lobes S2 and S5 as they approach longitude 90° W. R1 is now moving southwards and only very slowly west at its western edge. The large patch of flux in the Northern Hemisphere in 1905.5, immediately west of the null-flux curve in the North Atlantic, is progressively absorbed into the main lobe S2 as the twentieth century progresses, and is virtually undetectable by 1980.0. Here there is apparent northward movement of the flux patch.

The region of origin, along longitude 120° E, contains what Bloxham & Gubbins (1985) referred to as a localized field oscillation, near the undulation in the magnetic equator under Indonesia. Comparing the core-field maps shows the undulation to persist in this region, even in the oldest models, but that it also changes form quite rapidly. The time dependence of the field here is of a wholly different character from that in the South Atlantic, which has distinct flux patches drifting as a whole.

We would expect to identify new flux patches separating from this region, or from the main lobes S1 and S4, but the identification is very difficult with this short record. We tentatively identify R3 with the reverse flux feature in 1777.5; and a new flux patch (which could become N4) breaking from the same region in 1842.5.

5.6. *Changes in the dipole moment*

We have discussed secular variation in terms of core field rather than geomagnetic coefficients because the former can be interpreted physically in terms of inductive effects of core flows. However, the first geomagnetic coefficient (g_1^0) deserves special attention because, representing as it does strength of the Earth's axial dipole moment, it is our simplest measure of the global intensity of the field.

Values of g_1^0 for each of our models from 1842.5 to 1980.0, plus two points from 1959.5 and 1969.5 from earlier work (Gubbins & Bloxham 1985; Bloxham & Gubbins 1986), are plotted in figure 29. No intensity measurements were available for the earliest two models, 1715.0 and 1777.5, therefore their g_1^0 coefficients are arbitrary and have not been plotted. The variations of g_1^0 in figure 29 show the well-known decay of the dipole moment, which has amounted to 7 % in nearly 150 years. We infer that large variations in the axial dipole moment are a long-term part of the behaviour of the geomagnetic field, in agreement with palaeomagnetic findings (see, for example, Merrill & McElhinny 1983). A straight line was fitted to this curve by least squares to give

$$g_1^0 = -31\,359 + 16.2(t-1900), \tag{5.2}$$

where t is the date in years A.D. This line has a slightly steeper slope than the 'standard' one adopted by Barraclough (1974, equation (4.1) of this paper) of 15.5 nT a^{-1}. The difference reflects variability in the actual decay rate and the time intervals used to calculate it, rather than any discrepancy between the two analyses.

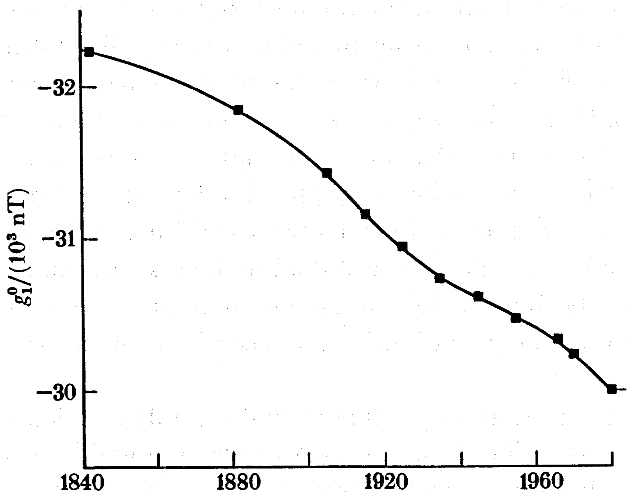

FIGURE 29. Decay of the axial dipole component of the field. Plotted are values of g_1^0 in nanoteslas from the field models; no intensity measurement was made before 1832, so no eighteenth-century model is plotted.

There are no direct measurements that bear on absolute intensity before 1832, the date of the first measurement. We must rely on archaeomagnetic and palaeomagnetic measurements of intensity if we wish to continue the curve in figure 29 further back in time. A single measurement at 1715.0 or 1777.5 can be converted to an estimate of g_1^0 using our field models, provided the non-uniqueness of those models, which are based on directional data alone, is restricted to a multiplicative constant (Proctor & Gubbins 1989).

Older archaeomagnetic data from Greece, Bulgaria, Rome, and the Middle East, reviewed in Creer *et al.* (1983), all suggest a g_1^0 in Roman times about 50% higher than the present value. Equation (5.2) gives a decay of 32400 nT in 2000 years, or a fall of 100%, too large to be consistent with the Roman data. This suggests the present period of rapid decay is temporary and that the rate was lower in the eighteenth century and earlier. As figure 29 shows, the rate in the mid-twentieth century is substantially lower than earlier in the century or at the present day. If we use this slower rate to extrapolate g_1^0 back to the Roman period we find agreement with the high archaeo- and palaeointensity measurements. The present rate of fall of the dipole moment is therefore exceptionally rapid.

6. THE FROZEN-FLUX HYPOTHESIS

6.1. *Background*

In the previous section we gave a commentary on the appearance of the maps of radial field on the core–mantle boundary. Attaching a physical interpretation to the behaviour of the radial field maps requires some understanding of the underlying causes of the changes. Our most powerful tool in this regard is the frozen-flux theory of Roberts & Scott (1965), as extended by Backus (1968).

The core fields must satisfy conditions for consistency with the frozen-flux condition: the topology of the null-flux curves, and the flux through them as given by the integrals in equation (1.10), must remain invariant. Only a very small amount of diffusion is required to change the topology of the null-flux curves and therefore the first condition is of no practical interest. We shall ignore it hereafter, except to note that changes in the topology between epochs in figure 20 are not so violent as to cast doubt on the accuracy of the field models.

The flux constraints (1.10) are more stringent and we can use them to test the validity of the frozen-flux approximation. Each flux integral is a spatial average of the radial field on the core–mantle boundary and is therefore less influenced than point estimates by the uncertainties in very small scale fields. Backus (1968) showed that these flux integrals must remain constant as a necessary condition for the flux to be frozen; he also showed them to be a sufficient set of conditions to allow the calculation of fluid motions consistent with the observed secular variation (in fact the problem of calculation of fluid motion is non-unique and a whole class of fluid velocities may then be found). However, these conditions are not sufficient to prove the flux is frozen-in because there may be diffusive flows consistent with the same magnetic field and secular variation.

With imperfect data it may well be possible to find suitable candidate fluid velocities by using the frozen-flux approximation. In such circumstances we should ask whether the data are sufficiently good to detect diffusion and whether the fluid flows are a reasonable approximation to the truth (or an unrealistic mapping of a truly diffusive flow). Typical estimates of the electrical conductivity of iron in the core suggest decay times of about 100 years for the smallest features in the core surface fields displayed in §4: it would therefore be rather implausible to fit the entire span of our models with the frozen-flux approximation. The most recent data is also the most accurate and it might be possible, therefore, to detect diffusion in the last 20 years as part of a long-term trend.

Booker (1969) was first to study the flux integrals for geomagnetic field models. He found a fall in the total flux linked with the core–mantle boundary; the fall is associated with the decay of the dipole moment. He conjectured the flux might have been converted to small-scale features which were not resolved by the field models available. Gubbins & Bloxham (1985) repeated the calculation with better field models and confirmed his conjecture, satellite data from 1969 to 1980 giving resolution capable of detecting the small-scale features missing from the models used by Booker.

Later Bloxham & Gubbins (1986) studied individual flux patches in the South Atlantic region and found evidence for change (i.e. a violation of the hypothesis) between epochs 1980.0, 1969.5, and 1959.5. They concluded the overall reversed flux in the Southern Hemisphere had increased in magnitude significantly (at the 99% level). This conclusion was tentative and heavily dependent on the validity of the formal error estimates: a factor of two increase in the error estimates of the integrals would remove the significance entirely, although such an increase would require a rather larger increase in the point errors in the radial field so that the result is more robust than it might appear. Part of the increase in flux was associated with the complete absence of the small reverse flux patch R1 in 1959.5, which clearly violates the frozen-flux hypothesis, and a large increase in the flux through the same patch between 1969.5 and 1980.0.

Subsequent calculations with historical field models (Bloxham & Gubbins 1985) and a preliminary version of the 1905.5 model (the final version is given in this paper) showed the change in total reversed flux through the Southern Hemisphere (i.e. south of the magnetic equator) had increased progressively throughout the 265-year span of the models, and that therefore the small increase detected in the last two decades was in fact a real phenomenon, a manifestation of a long-term diffusive trend. The models in this paper are used to investigate the flux changes further.

6.2. *Individual flux patches*

Changes in the topology of the null-flux curves make identification of the flux patches difficult in some cases.

Every model has a North Pole patch, with 1945.5 having additional patches near Iceland and Kamchatka and 1842.5 one near Greenland. The strengths of the flux integrals are distributed around 50 MWb (table 7), which strongly suggests a stationary patch of constant strength.

Most models have two small patches in the North Pacific; in 1935.5 (when data coverage in the Pacific Ocean was very poor) there is only one, in 1842.5 they are merged with the Southern Hemisphere, and in 1715.0 they are absent. Again this suggests stationary patches with no change in strength.

In most cases we observe a small patch beneath Easter Island; it is absent in 1935.5–1955.5 and 1905.5, times of bad data coverage, and is merged with the Northern Hemisphere in 1777.5 and 1882.5. Again this is evidence for a stationary patch with no change in intensity (the large value in 1715.0 cannot be taken in isolation as evidence of a change in intensity).

The very small patch in the North Atlantic has drifted in recent times. The rate of drift is supported by the older models. Even for models without a null-flux curve here there is a distinct low in radial field intensity. Again the flux integrals give no evidence for a change in intensity, but unlike the previous patches, which have maintained their position, this one has drifted persistently westward.

None of the patches considered so far give any suggestion of diffusion through a change in flux. We consider now the remaining patches in the Southern Hemisphere. In 1980.0 these are

Table 7. Flux integrals for the major patches in MWb

(The two models for epochs 1969.5 and 1959.5 from Gubbins & Bloxham (1985) have been included for completeness. A dash indicates the patch is absent. Abbreviations in parentheses indicate the name of a larger region to which the patch was joined at that epoch, for example in 1925.5, (NH) in the column for SA indicates the South American patch was joined to the Northern Hemisphere. Abbreviations are as given in the text in §6.4. Some small patches appear at isolated epochs: Indonesia in 1777.5 (−13 MWb), Greenland in 1842.5 (2 MWb), South Africa in 1905.5 (−12 MWb), Iceland (9 MWb) and Kamchatka (7 MWb) in 1945.5, and Central America in 1959.5 (6 MWb). $\mathcal{N}$ is the unsigned flux integral, given by the sum of the moduli of the contributing patches.)

epoch	NP	EP	WP	NA	EI	SH	AN	SA	IO	NH	$\mathcal{N}$
1980.0	39	2	33	3	−20	88	SA	−1274	SA	−17547	37858
1969.5	66	10	35	5	−41	−50	−57	−1250	SA	−17469	37620
1966.0	45	4	26	9	−23	−54	−40	−1241	SA	−17491	37618
1959.5	15	21	61	—	−10	—	IO	−588	−557	−17533	37376
1955.5	75	37	2	—	—	SA	—	−568	−488	−17630	37372
1945.5	43	26	120	9	—	NH	SA	−547	−506	−17691	37488
1935.5	54	—	99	—	—	−15	IO	−564	−575	−17957	38222
1925.5	37	1	58	—	−6	NH	—	NH	−330	−18259	37190
1915.5	31	7	72	40	−8	NH	−277	NH	AN	−18534	37538
1905.5	35	12	13	7	—	NH	−7	NH	−46	−18358	36822
1882.5	46	13	32	—	NH	−1	−26	NH	−59	−18545	37262
1842.5	2	—	NH	—	−1	−201	−126	−319	−66	−18219	37864
1777.5	91	5	36	—	NH	−155	—	−253	−1	−18243	37330
1715.0	63	—	—	—	−338	NH	−169	−152	—	−19269	39856

St Helena (in the South Atlantic Ocean) and the patch to its south shaped like a bone. In previous epochs these appear as separate patches below South America, Antarctica and the Indian Ocean.

The Antarctic patch seems to have been stationary (it appears in 1715.0 in virtually the same place as it does in 1969.5). Its intensity varies considerably between models and it sometimes merges with the South American (1945.5) or Indian Ocean (1935.5) patches. At epochs when it is a distinct patch its value appears to be around 50 MWb (table 7).

The South American patch drifts quite rapidly to the west. It merged with the Northern Hemisphere from 1882.5 to 1935.5 and it is therefore impossible to determine a precise long-term change in its strength. The flux integral is uniform from 1935.5 onwards; the historical models prior to 1882.5 suggest a slightly smaller value but this may be because of inaccuracies of the models. In any even there is no evidence for violation of the frozen-flux hypothesis because flux can quite legitimately be transferred into it from the Northern Hemisphere during the interval 1882.5–1935.5 when the two were joined.

The main evidence against frozen-in fields comes from the remaining patches in the Southern Hemisphere, in particular the Indian Ocean patch which can be seen to intensify quite dramatically in the figure 20*h*–*k*. The flux intensities are difficult to plot because of the continually changing topology of the bounding curves, but a compromise is as follows: to plot the combined flux of Antarctic and Indian Ocean patches (when they are distinct) for 1715.0–1966.0 and, on a different scale, the combined patches for all the Southern Hemisphere except Easter Island for 1715.0–1842.5 and 1935.5–1980.0. The missing epochs are due to merging of the Indian Ocean and South American patches in the later epochs and merging of the South American and Northern Hemisphere for the middle epochs.

We show the results in figure 30. We observe a steady increase in flux throughout the twentieth century, both in the Indian-Ocean–Antarctic combination and the combination of all Southern Hemisphere reversed patches. As stated earlier, the increase in the last 20 years was studied by Bloxham & Gubbins (1986) with the conclusion, subject to some qualifications, that the change was significant at the 99 % level. These patches occupy areas of quite good data coverage, particularly in the historical models, and there is no evidence for the patches varying with data distribution (as does the Easter Island patch for example). Figure 30 confirms the recent change as part of a long-term change in the flux integrals, and we now regard this as conclusive evidence for diffusion.

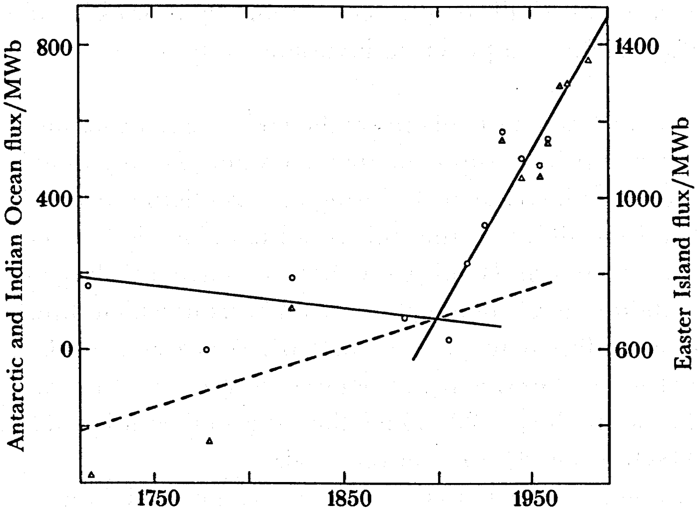

FIGURE 30. Evidence for diffusion from the Southern Hemisphere reverse flux patches. Shown as circles are the flux integrals for the combined flux of the Antarctic and Indian Ocean patches. From 1966 to 1980 the patches merged with the South American patch to form the 'bone' shaped patch, so these flux integrals are not plotted. Shown as triangles are the total flux integrals from all the Southern Hemisphere patches excluding Easter Island. Between 1882.5 and 1925.5 inclusive the South American patch was joined in the Northern Hemisphere (another diffusive effect), so these points are omitted. The straight lines indicate the trend of the points; before 1900 the broken line shows the trend for all patches, the solid line for just the Antarctic and Indian Ocean patches (after 1900 the solid line shows the trend for both).

Before about 1900 the change in flux is very much smaller, and not large enough to be significant, particularly when the lower accuracy of the two earliest models, which contain no intensity information, is taken into account. The contribution from the Indian Ocean flux patches is negligible (200 MWb) before 1900, and the changes in Southern Hemisphere flux represent mostly a reduction in intensity of the South American patch.

The St Helena patch is absent from the 1959.5 model but is present again in 1955.5 and earlier times (in fact this location appears to be the site of a persistent low-flux feature). Bloxham & Gubbins (1986) found this disappearance of a null-flux curve was evidence for diffusion. This part of the argument is now weakened because it is not part of a long-term trend. However, the growth of the St Helena flux patch in the later models is well defined, and we still prefer the interpretation that the flux patch weakened, and possibly vanished, near 1960.

6.3. *The unsigned flux integral and geomagnetic core radius*

A commonly quoted property of a magnetic field is its unsigned flux integral or pole strength, $\mathcal{N}$, given by

$$\mathcal{N} = \int_{S'} |B_r(r)|\,\mathrm{d}S', \tag{6.1}$$

where S' is the core–mantle boundary. This is the sum of the moduli of all the individual flux integrals, and is therefore also conserved in the absence of diffusion. It has an intuitive appeal as representing the total flux linked with the core surface. Constancy of $\mathcal{N}$ represents a weaker constraint on the field than the full complement of some eight or nine conserved flux integrals, but in some respects it might be a preferred invariant as being less prone to errors in the field model.

Values of $\mathcal{N}$ for the models reported here are shown in the last column of table 7. Apart from in 1715.0, its value has remained approximately constant, varying only by about 4%. There is some slight evidence of an increase in $\mathcal{N}$ during the twentieth century, but the scatter is very large and the evidence for diffusion from this condition alone is inconclusive.

The Northern and Southern Hemisphere patches have the largest flux integrals, and therefore their contribution to $\mathcal{N}$ dominates; local effects in which diffusion can be detected, such as the Indian Ocean flux patch, are 'swamped'. We cannot speak of the contribution of one model coefficient to $\mathcal{N}$, because it is a nonlinear property of the whole model, but for a purely dipolar field of strength $g_1^0 = 30000$ nT the value of the unsigned flux integral would be approximately 28 GWb or nearly 75% of the total.

The anomalous value of $\mathcal{N}$ in 1715.0 could be because of different variable damping, or because of the extrapolation (4.1) of the geomagnetic coefficient g_1^0 used to normalize the intensity of the model. Because the value of $\mathcal{N}$ in 1715.0 is larger than the average by about 6%, it suggests g_1^0 should be smaller than that given by (4.1) by a similar percentage, at $g_1^0 = -32252$ nT. This is in line with the conclusion drawn in §5.6 that the dipole decay was lower in the eighteenth century.

Hide & Malin (1981) have used conservation of $\mathcal{N}$ to determine the geomagnetic core radius. They used models of main field and secular variation to determine the rate of change of $\mathcal{N}$ with time at epoch 1965 for several values of the core radius. The 'best' estimate of the core radius was obtained when $\mathcal{N}$ was stationary. They obtained estimates of the radius that were comparable with the seismological estimate; similar results were obtained later by Voorhies & Benton (1982).

A geomagnetic determination of the core radius will never be as accurate as the seismological determination and therefore the study is of little interest. However, the same approach may be used on measurements from Jupiter's magnetic field to determine the radius of the conducting region in the interior, which is not known from any other method (Hide & Malin 1979); it is also conceivable that the top of the liquid core is composed of some non-conducting material and it is worth checking that the geomagnetic and seismological radii are in agreement. A significantly smaller value of the geomagnetic radius might indicate a non-conducting scum near the core surface. It is also possible that the lowermost mantle is highly conducting through presence of a high percentage of iron, but this would screen out the secular variation rather than give a larger value of the geomagnetic core radius.

We investigated the problem by calculating the flux integrals at different core radii for the two models at epochs 1980.0 and 1966.0 and studying the differences between the resulting values. The maps of core field are rougher for values of the core radius less than 3485 km, leading to larger values of the flux integrals in all cases, but no new null flux curves were introduced. For values of the core radius larger than 3485 km the maps of core field are smoother, leading to smaller values of the flux integrals, but in this case several of the smaller null flux curves are absent. The core field maps for epochs 1980.0 and 1966.0 for radii 3385 km and 3585 km are shown in figure 31.

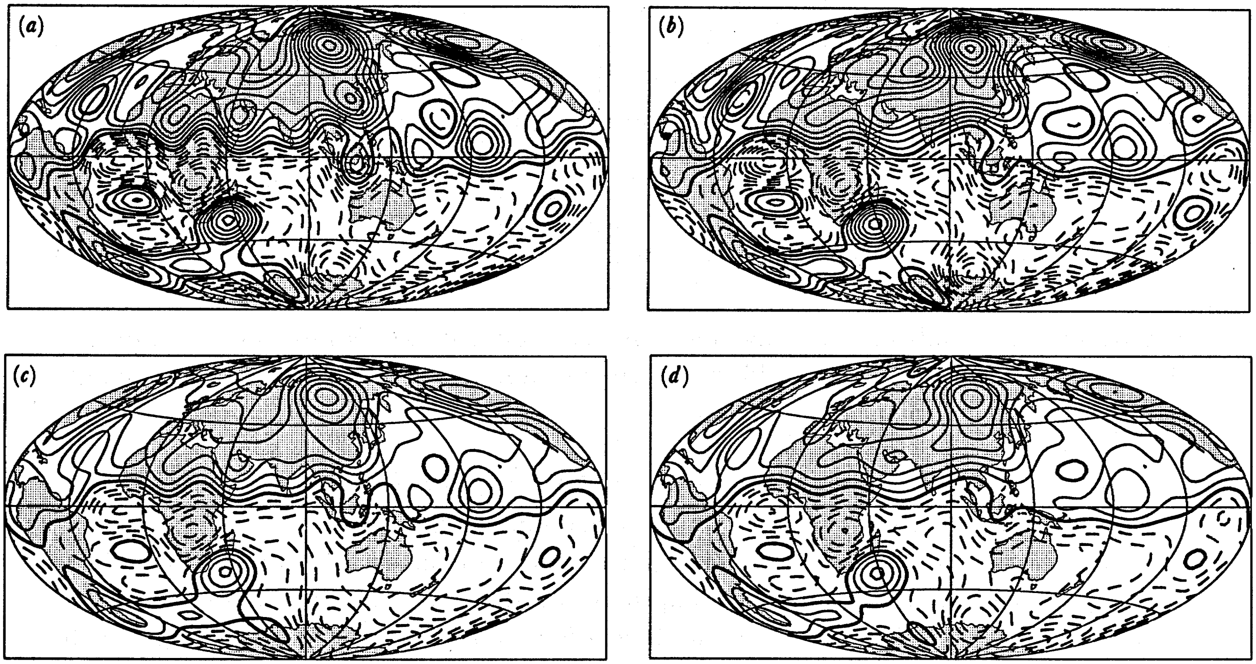

FIGURE 31. Maps of the radial component of the magnetic field near the core–mantle boundary. The solid lines are negative contours, the broken lines positive contours, and the bold lines zero contours. The contour interval is 100 μT. The map projection is Aitoff equal-area. (*a*) 1980.0 100 km below the core–mantle boundary; (*b*) 1966.0 100 km below the core–mantle boundary; (*c*) 1980.0 100 km above the core–mantle boundary; and (*d*) 1966.0 100 km above the core–mantle boundary.

We compare the integrals in table 8. Most indications are for a geomagnetic radius larger than the seismological value. A best estimate is about 3700 km, based on the unsigned flux integral, although no firm zero has been found. The difference with the seismological value of 3485 km is probably because of failure of the frozen-flux hypothesis and errors in the models. Flux diffusion is most noticeable for patch *B*, which does not permit interpolation to zero within the range. The geomagnetic radius is the larger, which is unphysical, suggesting again an error rather than a real effect. The size of the discrepancy is similar to that found by Hide & Malin (1981) in their second study where they found errors of 10–15%; Voorhies & Benton (1982) claimed greater accuracy.

For a proper calculation of the geomagnetic core radius we should work from original data rather than field models. Hide & Malin (1981) show a wide variation of results depending on the choice of truncation level in their spherical harmonic expansion. We have already used the core radius of 3485 km in determining the field models in this paper and so the results are

Table 8. Flux integrals and their time differences for various core radii

(The values of the integrals have been extrapolated to give a geomagnetic core radius for which the flux integral is near zero. B stands for the 'bone-shaped' contour beneath the south Atlantic region comprising IO, SA, and AN from other epochs. Blanks indicate the patch did not exist at that radius. Extrapolations to a 'best' estimate of the core radius were done from the differences shown here and those for radius 3485 km using the values in table 6. No estimate is given where there is no apparent zero in the radius range 3385–3685 km. The estimates were found by rough linear interpolation.)

	1980			1966			1980–1966			
curve	3685	3585	3385	3685	3585	3385	3685	3585	3385	radius
SH	−6	−32	−186	−1	−14	−132	−5	−18	−54	3690
B	−612	−891	−1796	−590	−861	−1772	−22	−30	−24	3470
EI	—	−4	−54	—	−4	−61	—	0	7	3485
EQ	−15824	−16599	−18755	−15844	−16596	−18614	20	−3	−141	3600
WP	2	12	33	0	7	60	2	5	−27	3450
EP	—	—	22	—	—	31	—	—	−9	3500
NA	—	—	26	—	—	43	—	—	−17	3500
NP	—	5	123	—	26	139	—	−21	−16	—
$\mathcal{N}$	32884	35052	41582	32870	34950	41158	14	102	424	3700?

already biased. A full statistical investigation using original data is probably not worth the effort, as the errors involved are likely to remain large and the problem is of very limited geophysical (but not planetary) interest.

6.4. *Field models consistent with the frozen-flux hypothesis*

We can produce models that satisfy the frozen-flux conditions to any desired degree of accuracy: the fit to the observations for a given value of the norm will, of course, deteriorate as the fit to the frozen-flux conditions is improved. Bloxham & Gubbins (1986) give a method for computing fields consistent with the frozen-flux conditions, by incorporating the flux constraints into a penalty function. The procedure involves calculating definitive flux integrals, in this case from the 1980.0 model, starting from some model with the same null-flux curve topology as 1980.0, and performing an inversion for a model with the same flux integrals as 1980.0. The problem is nonlinear since the position of the patches depends upon the model, so the solution must be sought iteratively. In practice we have found that about five iterations are needed.

It should be clear that this process cannot prevent the breaking up or merging of null-flux curves to form a different set of patches as the iteration proceeds. This was not a problem in the previous study of Bloxham & Gubbins (1986), when only models for 1980.0, 1969.5 and 1959.5 were used. The only split occurs in the 'bone-shaped' contour of 1980.0, when the Antarctic curve splits off in the earlier models, which was resolved by combining the patches into a single constraint. With earlier models the problem is more severe.

We used eight constraints in forming the 1969.5 and 1966.0 models. (The abbreviations used are: NP, North Pole; EP, north-east Pacific; WP, north-west Pacific; NA, North Atlantic; EI, Easter Island; SH, St Helena; AN, Antarctic; NH, Northern Hemisphere; IO, Indian Ocean; SA, South American; B, bone shaped contour.) For 1955.5 we merged the two Pacific patches into a single constraint, and separated the Antarctic and bone-shaped patches, again giving eight constraints. We tied these to the 1966.0 model. For all the remaining models in the twentieth century, we merged the two Pacific patches into a single constraint, and also merged all the South Atlantic patches (SH, B, AN, IO, and the small ones mentioned in the caption to table 7), leaving six patches.

We show the resulting models in figure 32 for epochs 1966.0–1905.5 inclusive. The model for 1966.0 is relatively unchanged, with the only noticeable difference being the increase in flux

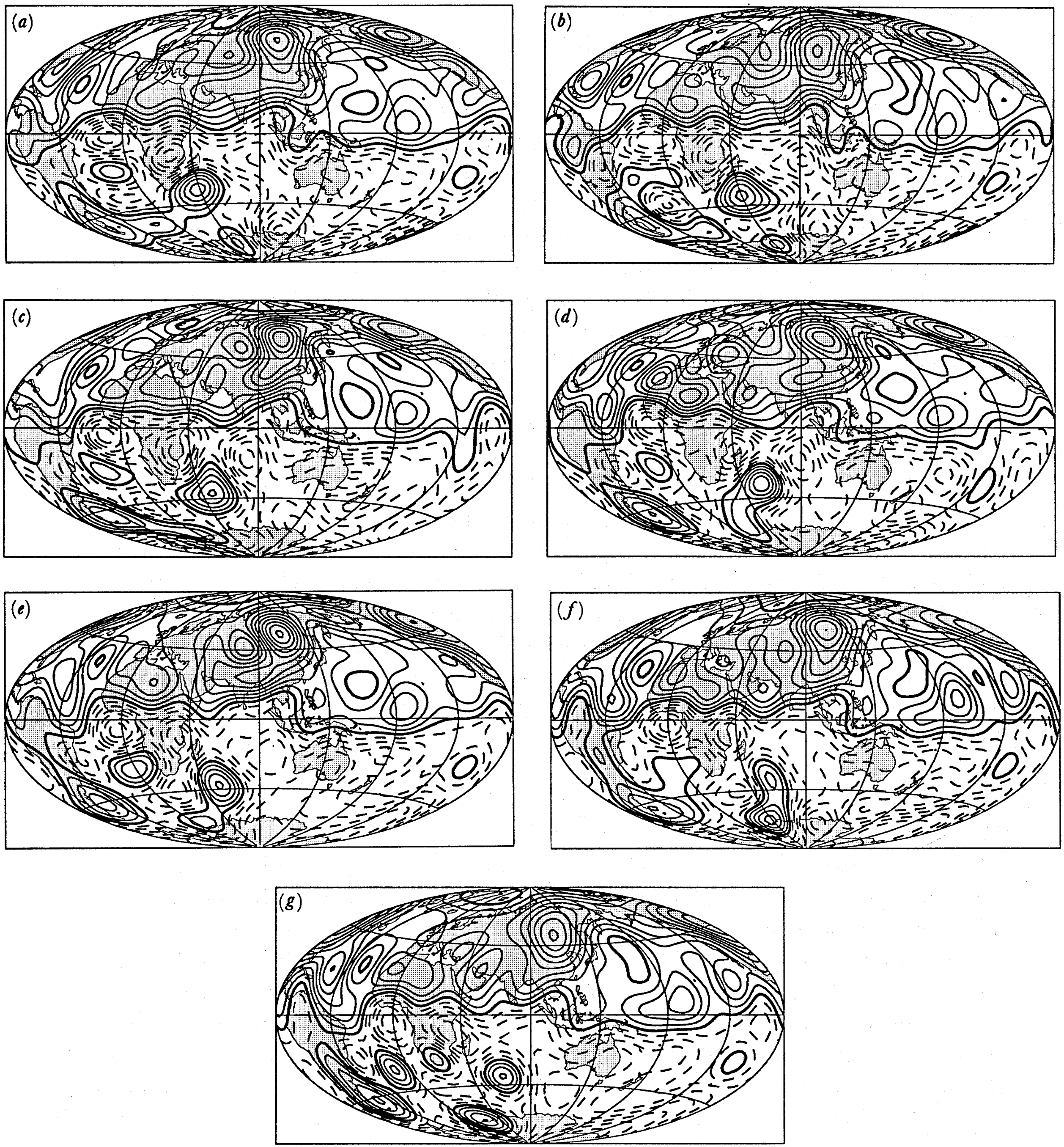

FIGURE 32. Maps of the radial component of the magnetic field at the core–mantle boundary, for flux-constrained models. The solid lines are negative contours, the broken lines positive contours, and the bold lines zero contours. The contour interval is 100 μT. The map projection is Aitoff equal-area. (*a*) 1966.0; (*b*) 1955.5; (*c*) 1945.5; (*d*) 1935.5; (*e*) 1925.5; (*f*) 1915.5; and (*g*) 1905.5.

through the St Helena patch. The model for epoch 1955.5 has changed quite significantly and now appears more like 1966.0 than its unconstrained counterpart for the same epoch. The 1935.5 and 1945.5 models are almost certainly improved by the addition of the constraints (the Easter Island curve, for example, was absent from these models only because of poor data coverage in the Pacific Ocean).

The earlier models of 1905.5–25.5 have better data distributions than 1935.5–45.5 and therefore any apparent 'improvement' is less likely to be a genuine reflection of core field behaviour. The South American null-flux curve remains distinct from the magnetic equator for all these models, albeit only just. The South Atlantic region again gives an indication of how difficult it is to satisfy the frozen-flux conditions here; although the total flux through this combination of patches is the same throughout, their appearance and morphology differs considerably from those of the more recent models. Note in particular the sharp increase in flux for the St Helena patch in 1905.5–25.5 caused by the flux constraints.

Our main purpose of producing this suite of models is to aid in calculating core motions, as described in the next section. Clearly, the core motion calculation will be difficult for the early part of the century because of the failure of the frozen-flux condition. The constraints have produced a more uniform set of models since 1925.

The misfits for the constrained models were mostly about 1 % larger than the misfits to their unconstrained counterparts. They could be used as a basis for a statistical test of the validity of the frozen-flux hypothesis. Bloxham & Gubbins (1986) have pointed out that comparing misfits between constrained and unconstrained models gives the identical result to comparing the differences in constraints (flux integrals) between epochs and their formal error estimates. A formal study of the later models has already suggested some violation of the frozen-flux conditions. We have not repeated the calculations for the earlier models for two reasons. First, the widely differing nature of the data-sets make the process questionable and it is unlikely to add anything to the case already made with the relatively homogeneous data-sets of the satellite era. Secondly, we believe the qualitative case presented as evidence of diffusion in §6.2 above is more convincing than any statistical test.

7. QUANTITATIVE INTERPRETATION: CORE MOTIONS

7.1. *Method*

As we have discussed, the frozen-flux hypothesis is our most powerful quantitative tool for the interpretation of our models. In this section we seek to apply the frozen-flux hypothesis to obtain maps of the fluid motion immediately beneath the core–mantle boundary.

As data we have a sequence of field maps. We seek to find the steady core motion that best (in a least-squares sense) advects the starting field (the first field map of the sequence) through the other members of the sequence. We use the flux constrained models, so as to satisfy the necessary and sufficient conditions of Backus (1968) for the determination of an eligible fluid velocity. By assuming that the velocity is steady through the time interval, we obtain a unique solution (Voorhies & Backus 1985). The assumption of steady motions has been found to be reasonable over intervals of 'a decade or two' by Voorhies (1986*a*). Bloxham (1988*a*) has presented some evidence that it may be reasonable over longer time intervals. However, Gubbins (1984) showed that magnetic observatory data were inconsistent with steady flow around 1970, the time of the magnetic jerk. The models derived in this paper, and those studied by Voorhies (1986*a*) and Bloxham (1988*a*), lack the resolution in time required to detect the jerk and may therefore be satisfied with a single, steady flow. The longest interval for which we seek solutions is 1925.5–1980.0; although we have available flux constrained models for 1905.5 and 1915.5 they are clearly corrupted by the effects of diffusion and would most likely lead to misleading solutions.

Here we give a summary of the method (full details are given by Bloxham (1988*a*)). Similar problems have been addressed by Voorhies (1986*a*, *b*) and Whaler & Clarke (1988). The method of Bloxham (1988*a*) differs from that used by other investigators in several respects: most important of these is that Bloxham (1988*a*) solves the full nonlinear problem, rather than a linear approximation.

The evolution of the magnetic field is given by

$$B_r(t_i) = B_r(t_0) - \int_{t_0}^{t_i} \nabla_{\mathrm{h}} \cdot (B_r \boldsymbol{u}_{\mathrm{h}})\, \mathrm{d}t. \tag{7.1}$$

This equation can be written in the form

$$\gamma_i = \boldsymbol{f}_i(\boldsymbol{u}_{\mathrm{h}}), \tag{7.2}$$

where γ_i is a data-vector consisting (essentially) of the coefficients of the field model at time t_i, and $\boldsymbol{f}_i$ is a nonlinear functional of $\boldsymbol{u}_{\mathrm{h}}$. The exact forms of γ_i and $\boldsymbol{f}_i$ can be derived from Bloxham (1988*a*).

We have N such equations, where $N+1$ is the number of field maps in the sequence, giving an nonlinear inverse problem of the form

$$\boldsymbol{\Gamma} = \boldsymbol{F}(\boldsymbol{u}_{\mathrm{h}}), \tag{7.3}$$

where the data vector $\boldsymbol{\Gamma}$ has the form $(\gamma_1, \ldots, \gamma_N)$, and the nonlinear functional $\boldsymbol{F}$ has the form $(\boldsymbol{f}_1, \ldots, \boldsymbol{f}_N)$. To satisfy the uniqueness condition of Voorhies & Backus (1985), we require $N \geqslant 3$.

We obtain solutions to the inverse problem by using an iterative procedure very similar to that described in §3. We weight these inversions by using weight matrices derived from the diagonal parts of the model covariance matrices. We do not include off-diagonal terms as we believe that we are unable to take account of correlations of the coefficients between epochs. Details of the parametrization and regularization of the problem are given by Bloxham (1988*a*).

For each set of solutions we calculate the norm (a measure of the roughness of the solution), the r.m.s. velocity, and the misfit, σ, given by

$$\sigma = \left[\frac{1}{N}\sum_{i=1}^{N} \frac{(\boldsymbol{m}_i - \hat{\boldsymbol{m}}_i)^{\mathrm{T}} C_{m_i}^{-1} (\boldsymbol{m}_i - \hat{\boldsymbol{m}}_i)}{\dim (C_{m_i})}\right]^{\frac{1}{2}}, \tag{7.4}$$

where $\boldsymbol{m}_i$ is the field model at time t_i, C_{m_i} is the covariance of $\boldsymbol{m}_i - \boldsymbol{m}_0$ (calculated from the covariances of the field models), and $\hat{\boldsymbol{m}}_i$ is the prediction of $\boldsymbol{m}_i$ (calculated by advecting $\boldsymbol{m}_0$ from time t_0 to t_i using the velocity model $\boldsymbol{u}$).

7.2. *Results*

We consider three sets of solutions:

(A) solutions for the sequence (1980.0, 1969.5, 1966.0, 1955.5);
(B) solutions for the sequence (1955.5, 1945.5, 1935.5, 1925.5);

(C) solutions for the sequence (1980.0, 1969.5, 1966.0, 1955.5, 1945.5, 1935.5, 1925.5).

The calculations are all performed by using the most recent member of the sequence as the starting model, and advecting backwards in time. We adopt this strategy, which is justified as a consequence of the frozen-flux approximation, because, in general, the most recent model should be the most reliable of the sequence, and hence the best starting model.

Within each set, we obtain solutions for a selection of values of the damping parameter, representing the trade-off between minimizing the model norm (roughness) and the misfit to the data.

In figure 33, we show the trade-off diagrams for these solutions. For the first interval (1980.0–55.5, curve A) we have obtained misfits to the field models only slightly larger than unity, indicating that we have fit the models to within almost their standard errors. For the earlier interval (1955.5–25.5, curve B) we obtain substantially worse fits, somewhat greater than twice the standard errors, on average. For the entire period (1980.0–25.5, curve C) we obtain fits which are roughly 50% larger than expected on the basis of our error estimates.

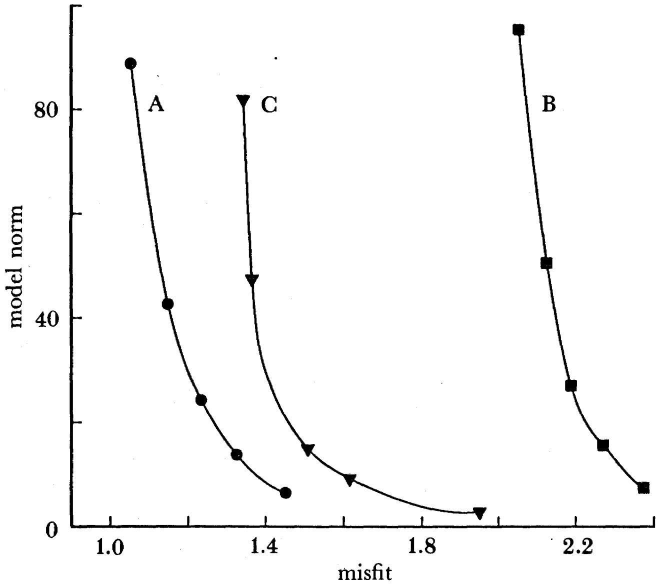

FIGURE 33. Trade-off diagram for core flow solutions. Curve A is for 1955.5–1980.0; B for 1925.5–1955.5; and C for 1925.5–1980.0.

We plot a solution from near the 'knee' of the trade-off curve from each set A–C in figure 34 respectively, and the power spectra of these solutions in figure 35 respectively.

We first consider the energies of these flows. The three solutions plotted have similar r.m.s. velocities: 12.9 km a^{-1} for 1955–80; 13.5 km a^{-1} for 1925–55; and 13.0 km a^{-1} for 1925–80. However, we cannot necessarily interpret this result as indicating that the r.m.s. flow velocity at the core surface is roughly 13 km a^{-1}. If we were to choose solutions away from the 'knee' of the trade-off curve, the solutions shown on the trade-off curve for set A, for example, range from 11.1 km a^{-1} to 20.7 km a^{-1}. However, in the absence of any compelling argument to accept solutions well away from the 'knee' we can infer that the r.m.s. flow velocity is roughly 12–15 km a^{-1}, slightly less than the values inferred by Voorhies (1986*a*).

The partition of energy between the toroidal and poloidal ingredients is noteworthy: we

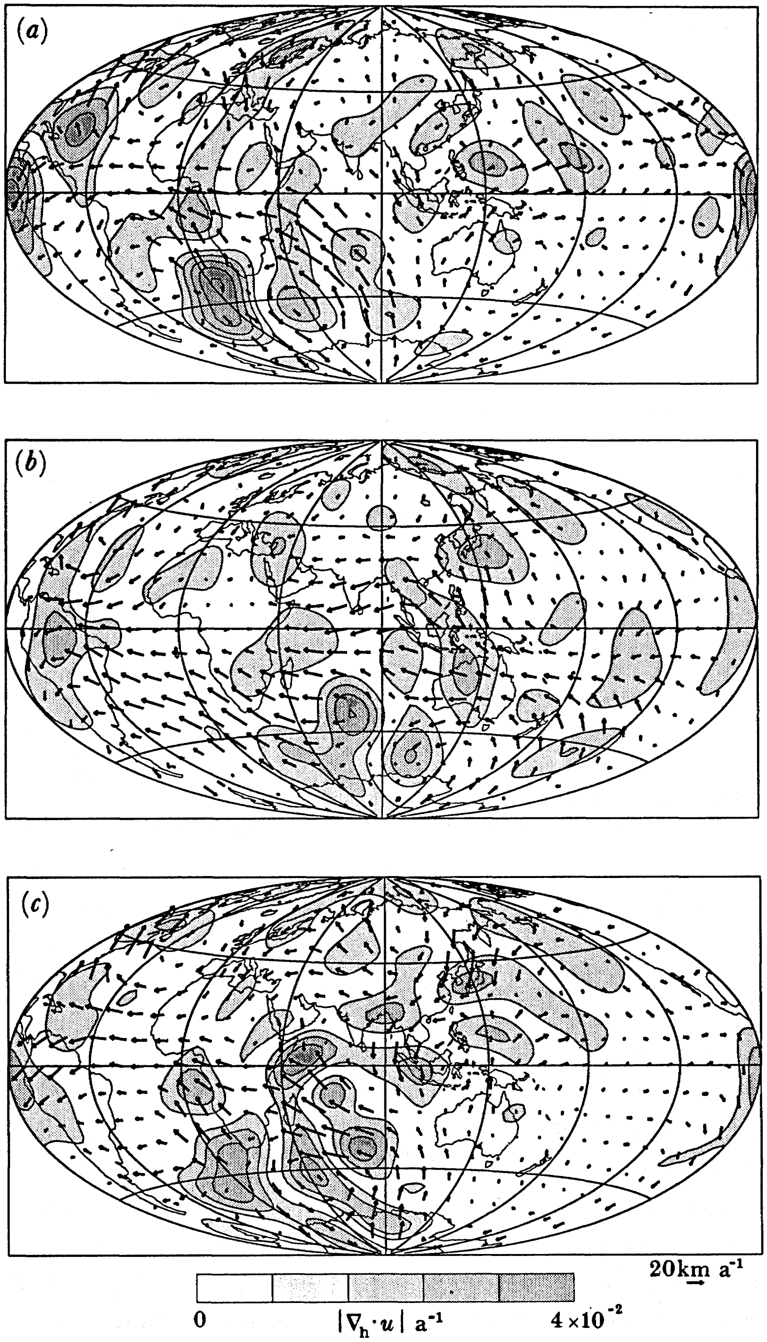

FIGURE 34. Maps of core surface motions for (*a*) 1955.5–1980.0; (*b*) for 1925.5–1955.5; and (*c*) for 1925.5–1980.0. The arrows represent surface flow vectors, scaled by the reference vector in the lower right-hand core of the figures. The shaded contours represent the magnitude of the horizontal flow divergence (a measure of the intensity of upwelling and downwelling), contoured according to the grayscale bar shown at the bottom of the figures.

observe that the toroidal flow is roughly a factor of four more energetic than the poloidal flow, indicating that these flows are fairly close to being toroidal in nature, lending support to the toroidal flow hypothesis of Whaler (1980). Voorhies (1986*a*) found a similar partitioning of the surficial kinetic energy. We might expect to obtain reasonable fits to the field with purely

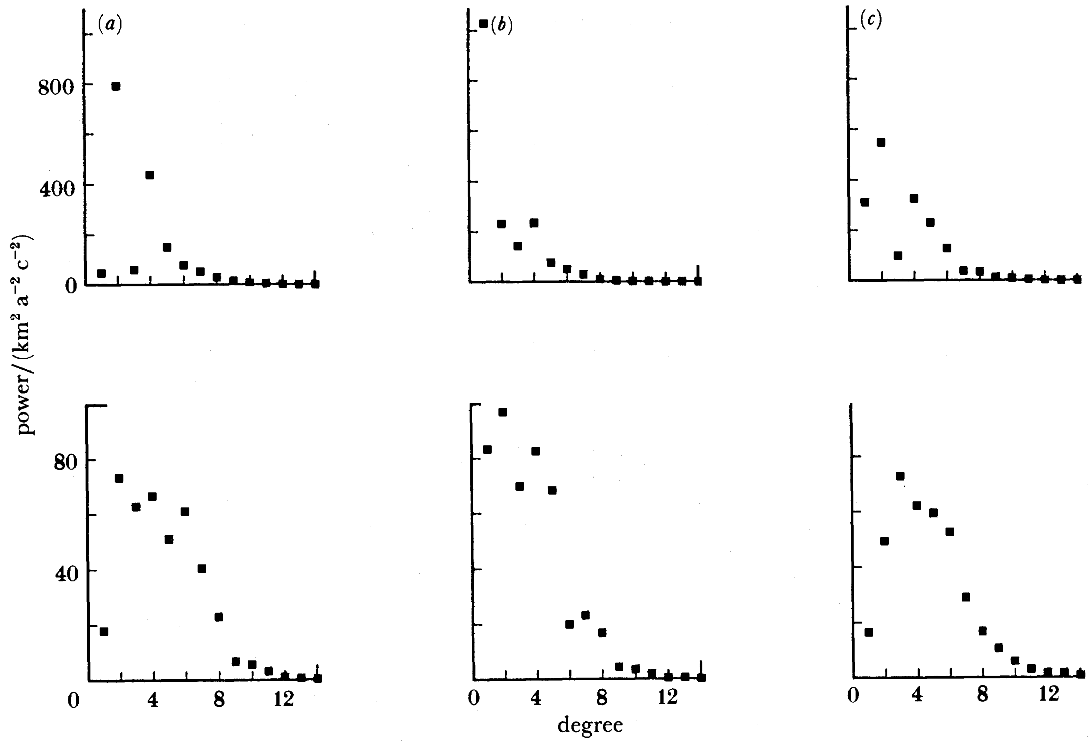

FIGURE 35. Power spectra of toroidal (top) and poloidal (bottom) core surface motions for (*a*) 1955.5–1980.0, toroidal r.m.s. 11.5 km a^{-1}, poloidal r.m.s. 5.7 km a^{-1}; (*b*) for 1925.5–1955.5, toroidal r.m.s. 12 km a^{-1}, poloidal r.m.s. 6.1 km a^{-1}; and (*c*) for 1925.5–1980.0, toroidal r.m.s. 11.8 km a^{-1}, poloidal r.m.s. 5.5 km a^{-1}.

toroidal flows. However, as noted at the end of this section, we reserve such a test to a future study.

To what extent is the flow steady? The solutions of set A for 1955–80 and for set B for 1925–80 certainly differ, but we cannot infer that such differences are necessarily significant. The errors on the 1925.5, 1935.5, and 1945.5 field models are larger than for the more recent models, and the flows obtained will be correspondingly less reliable. Furthermore, the misfits obtained during the interval 1925–55 are roughly twice as large as those obtained over the interval 1955–80 (we remind the reader that these are 'weighted' misfits, so the larger errors are already accounted for). Why are the misfits larger for the earlier models? There are three possibilities: first, it is possible that our errors for these earlier models are nevertheless too small relative to the more recent models; second, that the flow is less steady over the period 1925–55 than for 1955–80; third, that departures from the frozen-flux hypothesis are greater during the earlier period.

The first possibility could be the explanation if we have over-damped these earlier field models relative to the more recent ones, but the number of effective degrees of freedom for these solutions are only down by about 20% over the later solutions (see table 4). We would expect over-damping (relative to the later models) to reveal itself in this particular model statistic (as indeed it does for the eighteenth century models).

The second possibility is harder to assess; indeed, it is the very issue we were trying to address in the first place. We defer discussion of this possibility.

The third possibility is worthy of closer attention. Although we are using flux-fitted models, and so meet Backus's necessary and sufficient conditions for obtaining core flows, simply fitting the flux integrals is not sufficient to 'remove' the effects of diffusion. Backus's integral conditions are not sufficient for frozen-flux, they are only necessary. Thus it is possible that our fits are nevertheless degraded by diffusive effects; possibly the large changes in the flux observed beneath southern Africa immediately before this interval corrupt these solutions (these diffusive effects may continue). It is worth noting that a significant proportion of the poloidal flow in all the solutions shown is concentrated in this region, possibly indicating that the frozen-flux hypothesis may be a poor means of determining the poloidal ingredient of the flow.

Returning to the question of steadiness, it is clear that the answer is fogged by possible failure of the other approximations. The solution for 1955–80 plotted in figure 34*a* when used to advect the 1955 field back to 1925 results in a misfit of $\sigma = 5.7$, roughly twice that obtained with the 1925–55 solutions, not arguing unequivocally for either viewpoint. However, with the combined solutions, solving for the entire interval, we obtain quite reasonable fits to the field with misfits only 50% larger than expected on the basis of our error estimates do not provide a strong argument against steady flow.

However, the entire sequence of field models given in this paper do suggest that the flow is unsteady on the timescales studied. We observe quite abrupt changes in the field beneath southern Africa, seemingly beginning and ending quite rapidly, although drifting westward throughout. We have suggested that these changes are due to flux expulsion resulting from toroidal field entrained in poloidal flow. While unsteadiness of the upwelling is implied, it is not necessary (the configuration of toroidal field could be such as to make the process of flux expulsion episodic). The drift of the centre of inferred upwelling is more compelling argument against steadiness.

It is clear, though, from the field maps that we have discussed that while the flow may not be actually steady, the pattern of flow changes remarkably little over the time period studied. This pattern of flow, which we can infer subjectively by examining the field maps, and more objectively in this section, is relatively simple. (Some aspects of this description have been noted by Bloxham & Gubbins (1985), LeMouël *et al.* (1985) and Voorhies (1986*a*, *b*).) We observe very little flow beneath the Pacific hemisphere; northward flow toward the Indian ocean from beneath Antarctica, turning into a westward jet beneath the Indian ocean, continuing westward under Africa and the South Atlantic ocean. This strong zonal flow ceases abruptly at roughly 270° E, being accommodated by a downwelling beneath the easternmost Pacific, and a northerly flow beneath North America. The flow beneath Asia is less organized but generally weakly westward. We observe complex, and possibly time-dependent, flow beneath Indonesia, with possible transport across the equator, in violation of the geostrophic hypothesis (LeMouël 1984).

7.3. *Comment*

Our aim in this section has been to undertake a quantitative analysis of the secular variation observed in our field maps. However, as a method of obtaining core motions our method has a serious drawback. To satisfy the steady motions theorem of Voorhies & Backus (1985), our sequence of field models must have at least four members, limiting our choice of time interval. Although we have been able to produce solutions spanning periods of 24.5 years and 30.0 years in the twentieth century, to produce solutions for earlier periods would require solving over very long time periods: our earliest sequence of four field maps (1715.0, 1777.5, 1842.5, and 1882.5) spans 167.5 years. An alternative method is required.

A simple adaptation of this technique can be applied to the continuously time-varying field mapping technique of Bloxham (1987). With a continuously time-varying description the field can be evaluated at as many points in time as required, so the restriction encountered in this study is avoided. However, although it might appear that we could then produce steady solutions over as short a time interval as we might wish, the time interval must still be chosen sufficiently long that adequate resolution of the otherwise non-unique aspects of the flow are obtained.

In a future study, using time-varying field maps, we will address some of the specific issues discussed in this section, seeking to determine, for example, whether the flow is more nearly toroidal or geostrophic in nature. Preliminary results of such a study are reported by Bloxham (1988*b*), who finds some evidence that the flow is more nearly toroidal than geostrophic.

8. QUALITATIVE INTERPRETATION

8.1. *Diffusion*

The electrical diffusion time for the Earth's core is usually expressed in terms of the free decay time of a dipole solution to Helmholtz's equation (see, for example, Backus 1968) as $\tau = \mu_0 \sigma c^2/\pi^2$, which gives 25000 years for $\sigma = 5 \times 10^5$ S m^{-1}. This result is for a magnetic field configuration throughout the core that gives the slowest decaying mode (it is optimal in terms of low Ohmic decay). All other decay rates must be faster than this.

Obtaining a rigorous estimate of the decay rate of any of the core field features in figure 20 is impossible without some knowledge of the underlying field within the core itself. We must estimate $\hat{\boldsymbol{r}} \cdot \nabla^2 \boldsymbol{B}$, but we cannot determine $\partial^2 B_r/\partial r^2$ within the conductor from observations in the insulating exterior. We must be content with estimating $\nabla_\text{h}^2 B_r$ from the core field models and assuming the radial derivatives of B_r and other terms contributing to the full laplacian do not radically change the estimate (but, of course, in the insulator $\nabla^2 B_r = 0$ and these other terms must exactly cancel the horizontal laplacian!). The assumption may be grossly in error if a strong magnetic boundary layer is present at the top of the core.

For small features such as S3 in the central Pacific we have $l \approx 10$ which gives, by dividing the dipole decay rate by l^2, an expected decay time of 250 years. This value is probably an overestimate because the dipole decay rate is optimally low for this value of the electrical conductivity. It suggests that diffusion should be detectable during the span of the models shown in this paper. A corollary is that features that have persisted throughout, and which have not shown signs of changing in size, must be maintained by inductive effects. The fluid velocities required to maintain static features are very much slower than those determined from secular variation, for the frozen-flux hypothesis would require the velocity beneath a static feature to be zero (or at least a member of the class of non-inductive motions).

Bloxham & Gubbins (1985) estimate a fluid velocity of order 5×10^{-6} m s^{-1} to sustain the static patch S3 in the central Pacific. Similar flows are required to sustain the main lobes S1, S2, S4 and S5. This suggests a way to map the slower flows that occur on the diffusion timescale, and which may therefore be participating in the dynamo process. Flux is concentrated by downwelling and dispersed by upwelling; rapid flow would lead to a changing field in which the flux concentration is still continuing, but we suppose that an equilibrium has been reached at these static sites. The main sites of downwelling are then beneath static features S1–S5, and of upwelling beneath patches of low flux Z1–Z3. Note that the core velocities we infer from this indirect and rather speculative approach are two orders of magnitude below those calculated using the frozen-flux hypothesis in the previous section where diffusion was neglected.

Another diffusive process is suggested by the rapid change in the flux through the reverse flux feature R3 in recent times. The appearance of R3 and the adjacent moving feature N2 is reminiscent of a pair of sunspots and suggests they were formed by expulsion of strong subsurface (probably toroidal) flux. The mechanism was studied by Allan (1961) and Allan & Bullard (1966) for low magnetic Reynolds numbers and more recently by Bloxham (1986*b*) at higher values of the magnetic Reynolds number. Expulsion of toroidal flux would occur above upwelling; its efficiency depends on the rate of flow, the strength of the toroidal field beneath the core surface, and the ratio of electrical conductivities in the mantle and core (a parameter not investigated so far in calculations of either Allan or Bloxham). Bloxham concluded that this may be a very important effect for the observed secular variation, and that it was responsible for the present growth in the flux patch R3. Finite electrical conductivity in the mantle might make the effect even more significant.

Inversions assuming the frozen-flux hypothesis will nevertheless attempt to fit changes in the field caused by diffusive effects, for example a core spot pair, produced by expulsion of toroidal field due to an upwelling motion, may be mimicked as adjacent regions of upwelling and downwelling, although the actual configuration would depend upon the ambient field. It may be quite difficult to discriminate between poloidal motion with flux preserved on the one hand, and diffusion in the presence of a large toroidal field on the other.

8.2. *Implications for the dynamo*

Secular variation studies using the frozen-flux approximation cannot be related directly to behaviour of the geodynamo because they involve no diffusion, and the dynamo process is by its very nature a balance between inductive motions and diffusion. We may eventually gain some insight into the dynamo process from secular variation studies if the field is maintained by a wave dynamo in which nonlinear interactions of magnetohydrodynamic waves strengthen the mean field, as in the MAC-wave dynamo of Braginsky (1964) or dynamo waves in an oscillatory $\alpha\omega$-dynamo. However, further interpretation must await theoretical developments of the dynamo process.

The slower motions deduced from diffusive arguments in the previous section may be responsible for a steady dynamo. The striking symmetry of the main lobes S1, S2, S4 and S5 about the equator suggests that this is the case (Gubbins & Bloxham 1987). These lobes appear on approximately the same pair of longitudes in 1980.0. S4 is absent from 1715.0, probably because of very poor data coverage in the Southern Ocean and Antarctica at the time, so we omit this model. Locations of the main lobes in the remaining models suggest an even more symmetrical distribution of the average positions of these main lobes to about 65° N and S and 120° E and W.

The main lobes are the primary contributors to the Earth's dipole moment. We demonstrate by noting that the dipole geomagnetic coefficient, g_1^0, is proportional to the surface average of $B_r \cos\theta$:

$$g_1^0 = -\frac{3c^3}{8\pi a^3}\int B_r \cos\theta \,\mathrm{d}S, \tag{8.1}$$

where the integral is taken over the core–mantle boundary. By plotting $B_r \cos\theta$ on an equal area projection (figure 36), we find the dominant contribution to the total average comes from the four main lobes (see also Gubbins 1987). Furthermore, the zero-flux patches near the geographic North and South Poles are of comparable size to the projection of the inner core, suggesting the latitude of the main lobes is determined by the size of the inner core itself. Gubbins & Bloxham (1987) have speculated that these features are a surface manifestation of the ends of convection rolls aligned with the rotation axis and touching the inner core as envisaged by Busse in his model of the geodynamo (Busse 1975), but the same symmetry may occur in other modes of magnetoconvection.

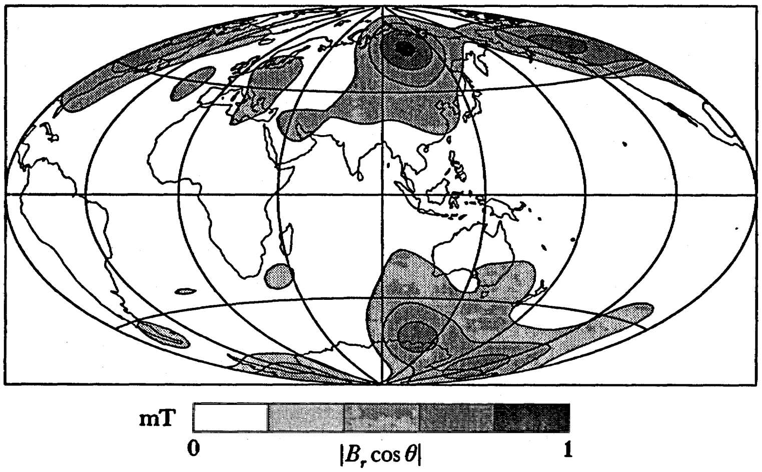

FIGURE 36. Map of $|B_r \cos\theta|$, showing contribution of features in the field to the axial dipole component. Note the predominant contribution of the two flux concentrations at high latitudes in each hemisphere.

8.3. *Interaction with the lower mantle*

Hide (1967) suggested long ago that convection in the core would be tied to features on the core–mantle boundary. He envisaged topography (bumps) to be the controlling feature, but other lateral variations could also be responsible: variations in temperature or electrical conductivity are two possible candidates. Bloxham & Gubbins (1987) proposed thermal interaction between the core and mantle, and found some agreement between cold patches in the lowermost mantle, as detected by high seismic velocities, and concentrations of flux; and hot patches, as detected by low seismic velocity, and either patches of low flux or flux expulsion. In this model the core fluid moves rapidly to equalize the temperature everywhere at the core–mantle boundary so that the mantle, which is itself convecting at a very much slower rate (centimetres per year rather than kilometres per year), sees an isothermal lower boundary.

Consider temperature effects first. An imposed isothermal boundary on the base of the mantle implies a heat flux across that boundary that varies laterally: heat flow will be high into a region where a cold sinker has fallen to the thermal boundary layer at the base of the mantle, and low where a hot plume has formed. Numerical models of mantle convection suggest this variability of heat flux may be as much as several hundred per cent of the average heat flux through the core–mantle boundary. This lateral variation in heat flux must be associated with a lateral transport of heat by surface motion of fluid in the core. The core fluid moves so rapidly in relation to the mantle that its pattern of convection is dictated by the structure of the thermal boundary layer at the base of the mantle. A simple order-of-magnitude argument (Bloxham & Gubbins 1987) shows the observed core flows associated with secular variation are sufficiently large to account for the lateral variation of heat flux into the mantle, and that therefore it is at least qualitatively plausible that the secular variation flows be driven, or at least heavily influenced by, the temperature within the mantle thermal boundary layer.

In the short term the core will simply respond to the pattern of heat flux across the core–mantle boundary imposed by the thermal boundary layer at the base of the mantle. In the long term the convection in the core and mantle may be tied together. Long-term aspects of the core convection are those features determined by the rotation axis and inner core boundary, both of which are fixed for long periods of geological time. Thus the characteristic shape of the geoid, which is closely related to the low-order dynamical core topography in figure 37, may be related to persistent core convection in the form of rolls aligned with the rotation axis touching the inner core.

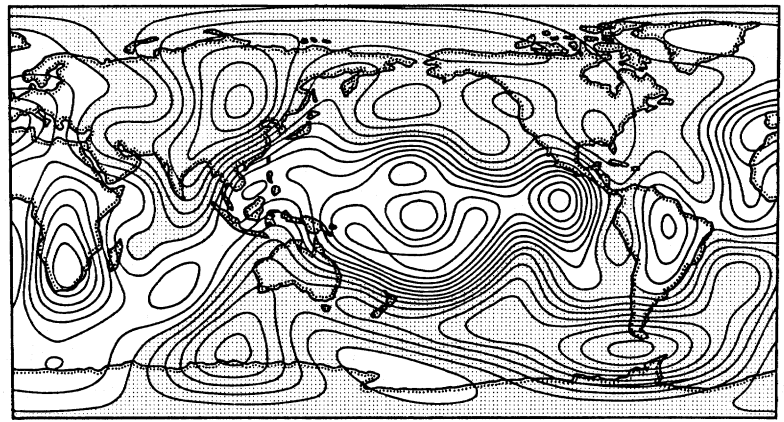

FIGURE 37. An estimate of CMB topography calculated from seismic inversions and gravity data by assuming mass anomalies are compensated dynamically by convective flow in a chemically homogeneous mantle. The contours also indicate the vertically averaged temperature in the lowermost few hundred kilometres of the mantle. From Gubbins & Richards (1986).

Now consider topography. Cold mantle material is also dense (provided it is chemically homogeneous) and therefore will be associated with topography on the core–mantle interface. The compensation of density anomalies in a convecting, self-gravitating mantle depends on mantle viscosity. Calculations of core topography for a chemically homogeneous mantle, using models for the seismic velocity of the lower mantle and the geoid with the effects of subduction zones removed, have been given by Hager (1984). This dynamic topography is directly related to the temperature in the lowermost mantle, and will only reflect the true core topography if there are no lateral variations in composition. Put simply, the core–mantle boundary is depressed beneath a cold sinker and elevated beneath a hot plume, it is therefore very difficult to isolate thermal effects from those of topography because they occur in the same place. Good correspondence is also found between the magnetic field and higher degree dynamic core topography (Gubbins & Richards 1986, fig. 8.2).

Seismic phases PcP and PKP can be used to measure core topography directly (Morelli & Dziewonski 1987; Creager & Jordan 1986). The resulting maps of core topography differ significantly from the calculations of dynamic topography, although all three show an elevated core–mantle boundary beneath Africa. These new maps of core–mantle topography show depressions in topography beneath the surface manifestations of the subduction zones in the 'ring of fire' around the Pacific. This suggests the topography may be associated with density anomalies in the subducted slabs in the upper mantle. The largest slab effect is expected beneath New Guinea where three subduction zones lie in close proximity; there is little evidence of a large bump there in either the model of Morelli & Dziewonski or the model of Creager & Jordan, but this may be due to lack of resolution. The core topography is different from that of Hager (1984); the two can be reconciled by supposing the subduction effect dominates the dynamical topography, that a low-viscosity layer at the base of the mantle prevents the formation of dynamically compensated topography, or that compositional variations are present.

The magnetic field also shows some evidence of the effect of subduction-related core topography. The line where secular variation stops lies along the west coasts of North and South America. Subduction occurs along this coast of South America, and only ceased along the west coast of North America a few million years ago, so that a density anomaly probably still remains (there is good evidence that a seismic velocity anomaly still persists (Grand 1986)). It appears almost as if a barrier stands in the way of the drifting features along this line. The region of stationary field and low flux in the Pacific region is outlined remarkably well by the ring-of-fire subduction zones (figure 20*a*, for example), and the site of *in situ* oscillations beneath Indonesia, diagnostic of a topographic feature on the core–mantle boundary (Bloxham & Gubbins 1985) lies directly beneath the site of the largest expected subduction-related topographic feature.

The correspondence with subduction zones is very surprising, and must still be regarded as highly speculative. It is very hard to understand how a bump can have as dramatic effect as suppression of secular variation throughout the Pacific. Furthermore, the seismological results and dynamical calculations are in conflict with each other to some extent, and also with the results of Wahr (1987), that the mis-alignment between the Earth's mean figure axis and mean rotation axis leaves no room for core topography of any size in the C_{21} and S_{21} (the analogue of g_2^1 and h_2^1) terms, and Gwinn *et al.* (1986), which similarly constrains the C_{20} term. The seismological results could perhaps be attributed to mislocation of earthquakes or some similar systematic effect which maps the subduction-zone signature to the core–mantle boundary, although the experiment of Morelli & Dziewonski (1987) has been very well designed to remove these problems; but it is a much more formidable task to dismiss both the seismic and geomagnetic results with a single, plausible explanation.

Finally we consider lateral variations in the electrical conductivity at the base of the mantle. Knittle & Jeanloz (1986) have argued that chemical reactions between the core and mantle may lead to the absorption of quite large fractions of iron into the lowermost mantle, yielding dramatic increases in the electrical conductivity there. A highly conducting region some 100 km thick, and with conductivity perhaps 10 times the normal value for the lower mantle, would be sufficient to screen a substantial part of the secular variation at the Earth's surface. Such a value for the thickness of such a layer is not unreasonable if the core is chemically equilibrated with the mantle (E. Knittle, personal communication), and the conductivity could easily be larger by a factor of 10. If such a region lay beneath the Pacific Ocean it could explain our observed lack of activity there.

We have listed three possible mechanisms for core–mantle interactions: thermal, topographic and screening. Thermal interaction is the most straightforward to understand and is almost certainly an important feature in whole-Earth convection and cooling. Topographic interaction is a more complicated mechanism and the magnetohydrodynamic effects have not yet been fully evaluated; the geophysical identification of bumps on the core–mantle boundary is also questionable. Variations in electrical conductivity in the mantle are even more difficult to assess, although their effect on the secular variation is easy to calculate.

These mechanisms differ in their timescale for change: temperatures will change on the overturn time for mantle convection, which is typically 10^8 years for the upper mantle, and would be at least 10^6 years in the lower mantle. Topography may change on the much shorter timescale of isostatic compensation, about 10^4 years, but dynamic topography associated with temperature variations would change only on the longer overturn time. Changes in electrical conductivity depend on the time for mass diffusion and chemical reaction between the core and mantle; it could be much faster than the thermal overturn time. The observations imply the 'ring-of-fire' encloses a region of low secular change, but the subduction zones are known to have changed their relative positions in the last few million years; therefore either a fast response mechanism like topography is required, or there is a broad, permanently hot feature in the lower mantle below the present Pacific Ocean.

9. CONCLUSIONS

1. We have analysed over 175000 magnetic observations from an interval spanning 285 years (1695–1980). Even those observations that date from the early eighteenth century are of sufficient reliability to allow determination of the core field. The main reason for the success with older data lies in the main source of error in all except satellite observations: the short-wavelength crustal signal. The crust contributes several hundred nanoteslas to each component of a magnetic observation, swamping other contributions to the overall error and certainly dominating the instrumental error in all but the very earliest measurements. Modern ground-based survey data are not therefore greatly more accurate than the older measurements. Furthermore, determining the core field is in some ways easier than determining the surface field because the horizontal components sample the core field at some distance away from the measurement site. Core field maps are therefore more tolerant of holes in the surface data distribution than are surface maps.

2. At the start of this project in 1982, the earliest main field model based on actual measurements rather than averages or charts was the 1965 IGRF. Earlier models had been made (see, for example, Barraclough 1978) but they had been derived from a wide range of methods using charts or other data, the accuracy of which could not be evaluated. The use of a consistent method throughout has allowed us to produce consistent core-field maps so that progressive differences between epochs can be interpreted as genuine secular variation. The persistence of stationary features in the field between different epochs has given us confidence that even small features are well resolved and that formal error estimates give a good guide to the repeatability of core-field features; consequently we have confidence that progressive time changes in small features are also well determined.

3. The radial field at the core–mantle boundary exhibits both stationary and time-dependent features. The full span of the models, covering 265 years (1715–1980), is long enough to render straightforward the discrimination between static and drifting features (a

westward drift rate of 0.2 deg a^{-1} would take a feature through 53° of longitude in this time) and between *in situ* oscillations and drifting patterns. A striking new result is that secular variation at the core–mantle boundary is absent from a large part of the Pacific hemisphere. A corollary is that drifting features must start and end at the boundaries of the region where secular variation dominates, or are deflected around the Pacific region where secular change is very low. We have found some direct indication of this, but the evidence is rather weak.

4. Almost all of the drifting features travel west. The only place we have found apparent eastward motion of a patch of flux is under northern Canada, where a long-term static field patch split in two and subsequently merged into one again. The eastward movement corresponds to the westernmost part of the patch moving to rejoin the eastern part, giving the impression of eastward flow, but it can equally well be interpreted as westward motion of low flux through a static feature of high flux. The overwhelming impression from the core-field maps is that of westward motion, although there is clear evidence of motion in the north–south direction also. We do not imply at this stage that the underlying core motion is everywhere westward (determination of core motions from secular variation requires a whole suite of further assumptions and calculations).

5. The main part of the static field is the core-field feature contributing most to the Earth's dipole moment. It shows a strong antisymmetry about the geographic equator. Such antisymmetry is a feature of dynamo fields: the full equations governing dynamos driven by thermal or simple compositional convection exhibit solutions in which the poloidal magnetic field is antisymmetric about the Equator. Separate solutions with symmetry about the Equator (usually called quadrupole-type symmetry as opposed to dipole-type) do not exist for the full dynamo equations, although they do occur in $\alpha\omega$-dynamo models. We conclude this large part of the field arises from a steady dynamo operating in the core, which may function separately from the processes driving the secular variation (Gubbins & Bloxham 1987).

6. When viewed along the rotation axis the main lobes of the radial field are close to touching the inner core circle (the circle of radius approximately 20° where the cylinder inscribing the inner core intersects the core–mantle boundary). We attribute this to features in the magnetoconvection that are influenced by the inner core, the obvious candidate being convection rolls aligned with the rotation axis. The details of convection in a strong magnetic field are not sufficiently well understood yet to make a more definite identification (Gubbins & Bloxham 1987).

7. There is unequivocal evidence that magnetic flux has not remained frozen to the core–mantle boundary throughout the 265-year time span of our models. The flux linked with a large part of the Southern Hemisphere has changed progressively and by a large factor throughout the last 200 years, and was strongest in the first quarter of the twentieth century. Furthermore, the changes in flux in the last two decades are too great to be accounted for by the formal errors: the satellite models are so good that magnetic diffusion can be detected in just 10 years (Bloxham & Gubbins 1985, 1986).

8. Most of the magnetic diffusion is associated with formation of a pair of flux spots beneath southern Africa. This is attributed to expulsion of subsurface flux by strong fluid upwelling, in a process akin to that responsible for the production of sunspots on the sun (Bloxham 1986*b*).

9. The reverse flux features in the South Atlantic region are responsible for the present fall in the dipole moment. R1, at present beneath South America, is drifting south towards the pole and is therefore having greater effect on the moment; R3, at present beneath southern Africa,

is growing in size and drifting west, and is also having greater effect on the moment. The combination of these two features explains almost all of the present fall in the dipole moment, as well as the variation in rate of fall throughout the twentieth century (Gubbins 1987).

10. Although we are able to construct field maps throughout the twentieth century with the same flux integrals as the 1980.0 model, we encounter difficulties because of changes in the morphology of the flux patches (particularly acute for 1905.5 and 1915.5) arguing further against the frozen-flux approximation.

11. Using these frozen-flux models of the core field, we are able to construct steady core velocities with a good fit to the observed changes in the field. We argue that the general pattern of fluid motion within the core is changing only very slowly with time. We find that the toroidal flow is substantially more energetic than the poloidal flow. However, we do not entirely trust these maps of the fluid motion, and conclude that the effects of diffusion may corrupt the solutions.

12. The presence of static features in the magnetic field, and fixed regions that are persistent centres of secular variation, suggest the field or fluid flow interacts with the overlying solid mantle. A comparison of these features with recent maps of seismic velocity in the lower mantle, and dynamic core topography based on seismic velocity, the geoid, and a model of mantle viscosity on the one hand, and core field on the other, gives strong evidence for a correspondence between the temperature in the thermal boundary layer at the base of the mantle and the magnetic field such as might occur if core flows were driven from above as thermal winds, or the core convection had become attached to permanent mantle features (Bloxham & Gubbins 1985, 1987).

13. Recent seismological maps of the core–mantle boundary topography show depressions of the interface beneath subduction zones. These depressions also delineate the Pacific region of low secular variation in the core field. The largest core–mantle boundary depression expected from the surface subduction zone signal lies beneath Indonesia, where the geomagnetic field exhibits *in situ* oscillations of the type that might be expected from topography on the core–mantle boundary (Bloxham & Gubbins 1985; Gubbins & Richards 1986).

We are particularly grateful to D. R. Barraclough and R. A. Langel for their help and advice with both the data collection and analysis; and to S. R. C. Malin, L. Newitt, V. N. Vadkovsky, K. Bretterbauer and F. Eleman. B. Burton and B. Hodder helped with the data preparation. We also thank the librarians of the Cambridge University Library, the British Museum, the Scottish National Library, the National Maritime Museum, the Royal Observatory Edinburgh and the British Geological Survey.

This work was supported by U.S. NSF grants EAR-8608890, EAR-8804426 and EAR-8804618, NASA grant NAG5-918, and U.K. NERC grant GR3/3475. A.J. and J.B. were supported by British NERC research studentships during the course of this work.

APPENDIX. THE INTERVAL 1860–1900

No catalogue of geomagnetic data exists for the period 1860–1900, and consequently there is no obvious starting point for the compilation of a data-set for this period. Compilations for other periods are discussed by, for example, Barraclough (1982) and Veinberg & Shibaev

(1969). Here we give a review of the sources used in the construction of the data-set. All the data sources used are given at the end.

A useful starting point for land surveys is the catalogue of Hellman (1909), which lists all isogonic charts predating its publication. Oceanic data are, however, generally more difficult to trace; references to these data are infrequent because of their difficulty of use in studies of the secular variation at one place. We will first discuss these oceanic data, and then consider land data.

The period saw increasing importance of charts of the geomagnetic elements, especially declination, for navigation. The British Admiralty published charts of D from 1858 onwards, but unfortunately most of the data on which the charts were based remain unpublished. Post-1890 data were published (Admiralty 1901), and before this date most of the original results still exist in manuscript form in the geomagnetism data archive of the British Geological Survey, Edinburgh, though some were included in the catalogues of Sabine (1868, 1872, 1875, 1877). The published data are much easier to deal with, but we have included a small proportion of these unpublished data, namely from the ships *Alert*, *Dart*, *Flying Fish*, *Liverpool*, *Myrmidon* and *Thalia*. The manuscript measurements are uncorrected for the deviations due to the permanent and induced magnetic effects of the ship, but the Admiralty corrections were also recorded and have been applied. In cases where only place names were given, we added the positions from the Admiralty publications of suitable sites for magnetic measurements (Admiralty 1894, 1908). The first U.S. Naval chart was published in 1882 and the naval data for the period 1881–1885 were published (U.S. Bureau of Navigation 1886) and have been used. These naval vessels were wooden, so the deviations were probably small. The latter publication was subsequently updated to include some 600 more data collected up to 1894 (U.S. Hydrographic Office (USHO) 1894). We note in passing that other USHO sources we have investigated (for example U.S. Hydrographic Office 1895; Littlehales 1897) contain no new data; they are rather studies of secular variation at certain places based on published data. We have contacted the naval departments in the U.K. and U.S.A. and believe these to be the only sources of published data. Many of the French naval data were found by searching through the volumes of *Annales Hydrographiques* for this period. (See the end of the reference list for sources.) The German Naval Observatory chart for 1880.0 (Deutsche Seewarte 1880) also serves as an indicator of data sources.

The most important oceanic measurements of all three elements come from two ships which sailed contemporaneously, *HMS Challenger* (Nares 1882) and *SMS Gazelle* (Hydrographischen Amt des Reich-Marine-Amts 1888–90), which both measured D, I and F on their circumnavigations. Linklater (1972) describes the former voyage. Total intensity was measured at sea using Fox's apparatus and magnetic deflectors (see, for example, McConnell 1980), and frequent calibration at landfalls was necessary from measurements of horizontal intensity by unifilar. Some *Challenger* D and I data in the Pacific with large residuals had to be removed manually.

The *Gazelle* was a German *man-of-war* whose mission was the observation of the transit of Venus on Kerguelen Island in 1874. Although the values of D and I reported appear satisfactory, we found *Gazelle* F data to be somewhat biased; figure 38 shows the residuals between the 'reduced' data and the 1882.5 model (calculated without *Gazelle* F data). The residuals are almost all positive, though they are uncorrelated with the local (calculated) field strength, arguing against induced magnetization. The correlation between consecutive values

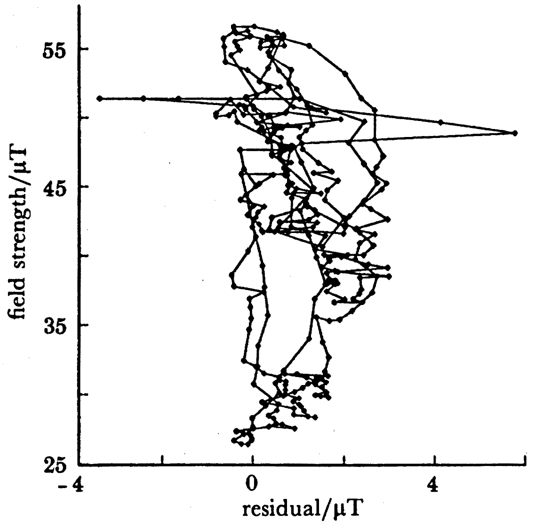

FIGURE 38. Residuals between 'reduced' data and the 1882.5 model for data from the *Gazelle*, plotted against local field strength. Dots indicate individual residuals, consecutive residuals are joined by straight lines.

rather argues for semi-permanent magnetization or incorrect calibration. This highlights one of the problems of measuring ***B*** in iron ships. Our analysis methods can deal with inaccurate, but not biased, data, and there appears to be no way of correcting the data *a posteriori*, in contrast to the case of induced magnetization where it would be possible to solve approximately for the susceptibility; consequently these F data have been omitted from the analysis.

The transits of Venus of 1874 and 1882 were events of international interest, and various expeditions were sent to observe them. However, unlike the extensive data from the *Gazelle*, we have found only limited magnetic data associated with two of the expeditions: the French expedition to Chile in 1882 (Bernardières 1884) and the British expedition to Kerguelen Island (Perry 1878). Recall that the motive of Cook's voyage to the South Seas in 1769, which furnished valuable data in our 1777.5 analysis, was the observation of an earlier transit.

A third world voyage of importance was that of the *Vanadis*, a Swedish warship whose expedition was under the auspices of Prince Oscar. Its departure is mentioned in *Nature*, vol. 29, p. 185 (1883), but the results were never published. Neumayer (1889, p. 37; 1891, p. 4) mentions that the magnetic measurements were on a large scale, and indeed measurements of all three components were taken. These data have recently been located by Dr F. Eleman (personal communication); apparently the measurements were improperly completed by the ship's crew. These data are not presently usable (they are mentioned for completeness and have not been included in the analysis).

The late part of the nineteenth century saw much activity in the Arctic, due to the search for the North-West passage from the Atlantic to the Pacific and the quest for the North Pole. Among the records from Arctic exploration which we have used are: the German expeditions under Koldewey & Hegeman of 1868 and 1869 (Freeden 1869; Koldewey 1874) in the *Germania* and *Hansa*; the Austro-Hungarian expedition of 1872 under Weyprecht & Payer (Weyprecht 1878) in the *Tegetthoff* (with the discovery of Franz Josef Land); the Swedish Arctic expedition of 1872–3 (Wijkander 1876); the British Arctic expedition of 1875 (Creak 1879) led by Nares (cf. *Challenger* expedition) in the *Alert* and *Discovery*; the Norwegian North Atlantic expedition (1876–8) of Wille & Mohn (1882); the expedition of the *Vega* (Wijkander

1883) under Nordenskiöld in 1878–80 (which discovered the North–East passage from Novaya Zemlya to the Bering Strait); the East Greenland expedition of 1891–92 (Ryder 1895); the Greenland expedition of 1891–93 of Drygalski (1897); the voyage of *La Manche* in 1892 (Leroux 1894); and Fridtjof Nansen's Norwegian North Polar expedition from 1893–96 in the *Fram* (Steen 1901 and Scott-Hansen 1901). A discussion of the instruments used in Nares's Arctic expedition has recently been given by Levere (1986). American expeditions subsequent to those of Kane & Hayes concentrated on the area north of their own continent; Hall led the U.S. Arctic expedition of 1871–73 (Bessels 1876) and Greely led the Lady Franklin Bay expedition of 1881–84 (Greely 1888) with the attainment of farthest north at the time; results from the subsequent Greely Relief expedition have also been included (U.S. Bureau of Navigation 1886).

In contrast there was practically no exploration in the Antarctic during this period. Indeed, the *Challenger* observations, having crossed the Antarctic Circle, provide the most southerly data available between the voyages of Ross and Crozier in the ships *Erebus* and *Terror* and of Moore & Clerk in the *Pagoda* in the 1840s (cf. 1842.5 model) and those of the *Southern Cross* expedition of Borchgrevink in 1898 (Borchgrevink 1902). Gerlache (1902) summarizes Antarctic exploration and confirms this view. For tracing sources of high latitude data we have found useful the catalogues of Veinberg (1933), Wilhjelm (1971) and Lundquist (1957).

The first International Polar Year 1882–83 has been described recently by Bretterbauer (1985). Eleven nations in all supported the venture, establishing 12 stations in the Arctic and two in southern latitudes. Although these measurements are intrinsically as accurate as other observatory annual means, our inability to apply a crustal correction through lack of reoccupation of the site means they contribute little more than other survey data.

In general we have used land survey data from original publications. Regional compilations of data have been used in four areas: the U.S.A., Canada, North Africa and western Russia. Tillo's catalogues (1881, 1885) for 'European Russia' contain measurements between latitudes 40° and 70° N and longitudes 16° and 70° E. There is a certain overlap with the catalogues of Sabine and data have been omitted to prevent duplication. A superior source is the catalogue of Veinberg (1929–33), which uses Tillo as one of the references. This must be taken as the definitive source for this area; Veinberg includes many data not found in other summaries (Veinberg 1929–33, table 1). We have not used this catalogue as Tillo's compilations give an adequate distribution within the time window (see figure 6), and Veinberg's data were unavailable to us. Veinberg's (1929–33) data have recently been prepared by Dr V. N. Vadkovsky of WDC-B2 (personal communication) and will be used in subsequent time-dependent calculations (Bloxham & Jackson 1989).

Keeling's (1907) catalogue has been used for North Africa, whereas for the U.S.A. the compilation of Hazard (1917) has been used. This contains all the results that were originally published in *Reports* or *Special Publications* of the U.S. Coast & Geodetic Survey. It also includes data from other bodies such as the Lake Survey and Corps of Engineers. Magnetic work in the U.S.A. gathered pace after 1870 because of the 'Bache Fund' and such people as Hilgard, Nipher, and Bauer (see Bauer 1902). After 1899 the Coast & Geodetic Survey began a systematic survey of the whole of U.S. territory, under the direction of Louis Bauer (see, for example, Bauer 1902, and figure 7). For Canada we have used both the catalogue of Herbert & McKnight (1924), which deals with Western Canada, and that of the Chief Astronomer

(1910) to try to ensure completeness. Many of the Canadian stations had been originally occupied by Sir John Franklin or Sir John Lefroy a few decades earlier.

The remaining land surveys we used were taken from original publications of the results. For example, Cirera (1893) reports on four expeditions to various islands of the Philippines between 1888 and 1892. Japanese data are provided by Knott & Tanakadate (1888) and Tanakadate (1904) for epochs 1887.5 and 1895 respectively. A few inclinations in China are given by Shadwell (1877). Fritsche (1893) supplies useful data between Europe and China, made during several journeys between 1867 and 1891, while he was director of the observatory in Peking. Note that his second publication of data (Fritsche 1897), including work up to 1894, adds only observations entirely around the Kursk anomaly near Moscow, which are extremely unsuitable for an analysis such as this. Two surveys financed by the Dutch government were those of Ryckevorsel (1880) in the Indian Archipelago and Ryckevorsel & Engelenburg (1890) in east Brazil, in the years 1874–77 and 1883 respectively. For South African data we have used the historical summary accompanying Beattie's (1909) report of his survey of 1902.

We have not compiled all European surveys available to us; they are generally on a fine scale and this area is served well by observatories. As an example of these fine scale surveys, the third survey of the British Isles for epoch 1886 used 205 stations between the years 1884–88 (Rucker & Thorpe 1890). In the subsequent three years the grand total of observation sites was increased to 882 (Rucker & Thorpe 1896); this density of measurements is too great for our purposes.

Veinberg (1929–33) and Veinberg & Shibaev (1969) suggest that the compilations of Sabine (1868, 1870, 1872, 1875, 1877) were not entirely comprehensive; for the U.S.S.R. Sabine compiled just over half the available data. We have also found this to be the case. For example, the survey of Victoria, Australia during the years 1858–64 by G. Neumayer whilst he was director of the Flagstaff observatory (Neumayer 1869), embracing 230 stations, was not included in Sabine's (1877) Southern Hemisphere catalogue.

Some of the aforementioned sources can be found in the reviews by Schering (1889, 1891, 1894, 1897, 1900) and Pasal'ski (1901); the latter is an extremely useful reference source. These papers were only located towards the end of the project and are not necessarily readily accessible.

The Greenwich meridian was adopted as an international longitude standard only in 1884, and some national conventions remained in use later than that date. Consequently some of the longitudes had to be corrected to Greenwich from the particular national conventions of Paris, the observatory at Pulkova (Leningrad), and San Fernando. The data contained in the journal *Annales Hydrographiques* continued to measure longitude from Paris until at least 1895; this difference of 2° 13 min arc was unexpected and difficult to detect. The conversion 1 B.U. = 4610.8 nT has been used to convert intensity measurements from British (or English) units to nanoteslas (Barraclough 1978).

REFERENCES

Admiralty 1894 *Instructions for making observations of the variation of the compass, with list of spots on different naval stations, specially suitable for magnetic observations.* London: Admiralty.

Admiralty 1901 *List of magnetic observations made by the officers of H.M. ships and Indian Marine Survey during the years 1890–1900.* London: Admiralty.

Admiralty 1908 *List of spots suitable for magnetic observations and list of places where abnormal variations have been reported.* Hydrographic Department, no. 211. London: Admiralty.

Aki, K. & Richards, P. G. 1980 *Quantitative seismology: theory and methods.* San Francisco: W. H. Freeman.

Allan, D. W. 1961 Ph.D. thesis, University of Cambridge, U.K.

Allan, D. W. & Bullard, E. C. 1966 *Proc. Camb. phil. Soc.* **62**, 783–809.

Backus, G. E. 1968 *Phil. Trans. R. Soc. Lond.* A**263**, 239–266.

Backus, G. E. 1970*a* *Proc. natn. Acad. Sci. U.S.A.* **65**, 1–7.

Backus, G. E. 1970*b* *Proc. natn. Acad. Sci. U.S.A.* **65**, 281–287.

Backus, G. E. 1970*c* *Proc. natn. Acad. Sci. U.S.A.* **67**, 282–289.

Backus, G. E. 1974 *Geophys. Res. Lett.* **1**, 21.

Backus, G. E. 1988 *Geophys. J.* **92**, 125–142.

Backus, G. E. & Gilbert, F. 1967 *Geophys. Jl R. astr. Soc.* **13**, 247–276.

Backus, G. E. & Gilbert, F. 1968 *Geophys. Jl R. astr. Soc.* **16**, 169–205.

Backus, G. E. & Gilbert, F. 1970 *Phil. Trans. R. Soc. Lond.* A**266**, 123–192.

Barraclough, D. R. 1974 *Geophys. Jl R. astr. Soc.* **36**, 497–513.

Barraclough, D. R. 1978 *Geomagn. Bull. Inst. Geol. Sci.* **8**, 1–65.

Barraclough, D. R. 1982 *Phil. Trans. R. Soc. Lond.* A**306**, 71–78.

Barraclough, D. R. 1985 Halley's Atlantic magnetic surveys. In *Historical events and peoples in geosciences* (ed. W. Schröder). New York: Peter Lang.

Barraclough, D. R., Gubbins, D. & Kerridge, D. 1989 *Geophys. Jl Intl.* **98**, 293–299.

Barraclough, D. R. & Malin, S. R. C. 1971 *Rep. no. 71/1. Inst. Geol. Sci.*, 26 pp. London: HMSO.

Bauer, L. A. 1902 *United States magnetic declination tables and isogonic charts for 1902 and principal facts relating to the Earth's magnetism.* Washington, D.C.: Government Printing Office.

Beattie, J. C. 1909 *Report of a magnetic survey of South Africa.* London: The Royal Society.

Benton, E. R. & Whaler, K. A. 1983 *Geophys. Jl R. astr. Soc.* **75**, 77–100.

Bernardières, M. 1884 *Résumé des déterminations magnétiques effectuées en 1882–1883 par la mission chargée de l'observation du passage de Venus au Chili, et de la mesure de différences de longitude sur la côte occidentale de l'Amérique du sud. Extrait des annales hydrographiques, 1^er^ semestre.* Paris: Imprimerie Nationale.

Bessels, E. 1876 *Scientific results of the U.S. arctic expedition, vol.* 1. *Physical Observations.* Washington, D.C.: Government Printing Office.

Bloxham, J. 1986*a* *J. geophys. Res.* **91**, 13954–13966.

Bloxham, J. 1986*b* *Geophys. Jl R. Astr. Soc.* **87**, 669–678.

Bloxham, J. 1987 *J. geophys. Res.* **92**, 11597–11608.

Bloxham, J. 1988*a* In *Mathematical geophysics, a survey of recent developments in seismology and geodynamics* (ed. N. J. Vlaar, G. Nolet, M. J. R. Wortel & S. A. P. L. Cloetingh). Dordrecht: Reidel.

Bloxham, J. 1988*b* *Geophys. Res. Lett.* **15**, 585–588.

Bloxham, J. & Gubbins, D. 1985 *Nature, Lond.* **317**, 777–781.

Bloxham, J. & Gubbins, D. 1986 *Geophys. Jl R. astr. Soc.* **84**, 139–152.

Bloxham, J. & Gubbins, D. 1987 *Nature, Lond.* **325**, 511–513.

Bloxham, J. & Jackson, A. 1989 *J. geophys. Res.* (Submitted.)

Booker, J. R. 1969 *Proc. R. Soc. Lond.* A**309**, 27–40.

Borchgrevink, C. E. 1902 *Magnetic and meteorological observations made by the 'Southern Cross' antarctic expedition, 1898–1900.* London: Harrison & Sons (for the Royal Society).

Braginsky, S. I. 1964 *Geomagn. Aeron.* **4**, 572–583.

Braginsky, S. I. 1984 *Geophys. Astrophys. Fluid Dyn.* **30**, 1–78.

Bretterbauer, K. 1985 J. Payer, C. Weyprecht, H. Wilczek: the promoters of international polar research. In *Historical events and people in geosciences* (ed. W. Schröder). New York: Peter Lang.

Bullard, E. C., Freedman, C., Gellman, H. & Nixon, J. 1950 *Phil. Trans. R. Soc. Lond.* A**243**, 67–92.

Busse, F. H. 1975 *Geophys. Jl R. astr. Soc.* **42**, 437–459.

Cain, J. C., Hendricks, S. J., Langel, R. L. & Hudson, W. V. 1967 *J. Geomagn. Geoelect., Kyoto* **19**, 335–355.

Chave, A. D., Thomson, D. J. & Ander, M. E. 1987 *J. geophys. Res.* **92**, 633–648.

Chief Astronomer 1910 Report of the Chief Astronomer for the year ending March 31 1909. *Department of the Interior Sessional paper, no. 25a,* Ottawa.

Cirera, P. Ricardo 1893 *El Magnetismo Terrestre en Filipinas.* Manila: Observatorio Meteorologico de Manila.

Claxton, T. F. 1899 *Mauritius magnetical reductions being a discussion of the results obtained from the self-recording magnetometers from 1875 to 1890 under the direction of C. Meldrum, M.A., L.L.D., F.R.S., together with a discussion of the absolute determinations of magnetic declination, horizontal force and dip from 1875 to 1897.* Mauritius.

Creager, K. C. & Jordan, T. H. 1986 *Geophys. Res. Lett.* **13**, 1497–1500.

Creak, E. W. 1879 *Proc. R. Soc. Lond.* **29**, 29–42.

Creer, K. M., Tucholka, P. & Barton, C. E. 1983 *Geomagnetism of baked clays and recent sediments.* Oxford: Elsevier.

Cunningham, J. 1704 *Phils. Trans. R. Soc.* **24**, 1639–1647.

Currie, R. G. 1967 *J. geophys. Res.* **72**, 2623–2633.

Deutsche Seewarte 1880 *Annalen der Hydrographie und marit. Mateorol.* **7**, 337–345.

Drygalski, E. V. 1897 *Grönland-Expedition der Gesellschaft für Erdkunde zu Berlin* (*1891–93*), *Band* 2. Berlin: W. H. Kuhl.

Ducruix, J., Courtillot, V. & Le Mouël, J-L. 1980 *Geophys. Jl R. astr. Soc.* **61**, 73–94.

Feuillée, L. 1714–1735 *Journal des observations physiques, mathematiques et botaniques faites par ordre du Roi sur les côtes Orientales de l'Amerique Meridionale & aux Indes Occidentales, 2 vols.* Paris: Pierre Giffart (1714) & Jean Mariette (1735).

Franklin, J. N. 1970 *J. math. Analysis Applic.* **31**, 682–716.

Freeden, W. V. 1869 *Die Wissenschaftlichen Ergebnisse der Ersten Deutschen Nordfahrt 1868. Geographie und Erforschung der Polar Regionen, no. 27* (Aus Petermann's Geogr. Mittheilungen 1869, Heft 6). Gotha: Justus Perthes.

Fritsche, H. 1893 *Ueber die Bestimmung der geographischen Länge und Breite und der drei Elemente des Erdmagnetismus durch beobachtung zu lande sowie erdmagnetische und geographische Messung an mehr als tausend verschiedenen Orten in Asien und Europa, ausgefuhrt in den Jahren 1867–1891.* St Petersburg.

Fritsche, H. 1897 *Observations Magnétiques sur 509 lieux faites en Asie et en Europe pendant la periode de 1867–1894 par Dr. H. Fritsche, Directeur émerité de l'Observatoire I. Russe de Peking.* St Petersburg.

Gauss, C. F. 1833 *Göttingen comment* **8**, 3–44.

Gerlache, A. de 1902 *Quinze mois dans l'antarctique.* Paris, Brussels.

Grand, S. P. 1986 Ph.D. thesis, California Institute of Technology, U.S.A.

Greely, A. W. 1888 International Polar Expedition. *Report on the Proceedings of the U.S. Expedition to Lady Franklin Bay, Grinnel Land, vol.* II. Washington: Government Printing Office.

Gubbins, D. 1975 *Geophys. Res. Lett.* **2**, 409–412.

Gubbins, D. 1983 *Geophys. Jl R. astr. Soc.* **73**, 641–652.

Gubbins, D. 1984 *Geophys. Jl R. astr. Soc.* **77**, 753–766.

Gubbins, D. 1986 *J. Geomagn. Geoelect., Kyoto* **38**, 715–720.

Gubbins, D. 1987 *Nature, Lond.* **326**, 167–169.

Gubbins, D. & Bloxham, J. 1985 *Geophys. Jl R. astr. Soc.* **80**, 695–713.

Gubbins, D. & Bloxham, J. 1987 *Nature, Lond.* **325**, 509–511.

Gubbins, D. & Richards, M. 1986 *Geophys. Res. Lett.* **13**, 1521–1524.

Gubbins, D. & Roberts, N. 1983 *Geophys. Jl R. astr. Soc.* **73**, 675–687.

Gubbins, D. & Roberts, P. H. 1987 *Geomagnetism*, vol. 2, ch. 1 (ed. J. A. Jacobs). London: Academic Press.

Gwinn, C. R., Herring, T. A. & Shapiro, I. R. 1986 *J. geophys. Res.* **91**, 4755–4765.

Hager, B. H. 1984 *J. geophys. Res.* **89**, 6003–6015.

Hahn, A., Ahrendt, H., Meyer, J. & Hufen, J-H. 1984 *Geol. Jb.* **75**, 125–156.

Halley, E. 1683 *Phil. Trans. R. Soc.* **13**, 208–221.

Halley, E. 1692 *Phil. Trans. R. Soc.* **16**, 563–578.

Hansteen, C. 1819 *Untersuchungen über den Magnetismus der Erde.* Christiana: Lehmann & Gröndahl.

Hazard, D. L. 1917 United States Magnetic Tables and Magnetic Charts for 1915. *U.S. Coast & Geodetic Survey Special Publication, no. 44.*

Hellman, G. 1909 Magnetische Kartographie in historisch-kritischer Darstellung. *Veröffentlichungen des Königlich Preußischen Meteorologischen Instituts, no.* 215. Abhandlungen Bd. III. no. 3. Berlin: Behrend & Co.

Hendricks, S. J. & Cain, J. C. 1963 *NASA Goddard Space Flight Center. Tech. Rep. August.* Washington, D.C.: NASA.

Herbert, W. H. & McKnight, J. H. 1924 Magnetic Results in Western Canada. *Topographical Survey of Canada, Bull. 52.* Ottawa: Dept. of Interior.

Hide, R. 1966 *Phil. Trans. R. Soc. Lond.* A**259**, 615–647.

Hide, R. 1967 *Science, Wash.* **157**, 55–56.

Hide, R. & Malin, S. R. C. 1979 *Nature, Lond.* **280**, 42–43.

Hide, R. & Malin, S. R. C. 1981 *Proc. R. Soc. Lond.* A**374**, 15–33.

Hide, R. & Stewartson, K. 1972 *Rev. Geophys. Space Phys.* **10**, 579–598.

Hoerl, A. E. & Kennard, R. W. 1970 *Technometrics* **12**, 55–67.

Hydrographischen Amt des Reich-Marine-Amts 1888–90 *Die Forschungsreise SMS Gazelle in den Jahren 1874–1876 unter Kommando des Kapitans zur See Freiherrn von Schleinitz*, 2 vols. Vol. II (*Physik und Chemie*). Berlin.

Jackson, D. D. 1979 *Geophys. Jl R. astr. Soc.* **57**, 137–157.

Keeling, B. F. E. 1907 Magnetic Observations in Egypt 1895–1905, with a summary of previous magnetic work in Northern Africa. *Ministry of Finance, Egypt. Survey Department paper, no. 6.* Cairo: National Printing Department.

Knittle, E. & Jeanloz, R. 1986 *Geophys. Res. Lett.* **13**, 1541–1544.

Knott, C. G. & Tanakadate, A. 1888 A Magnetic Survey of all of Japan by Order of the President of the Imperial University. *The Journal of the College of Science, Imperial University, Japan*, vol. II, part III. Japan: Tokyo.

Koldewey, K. 1874 *Die Zweite Deutsche Nordpolarfahrt 1869–70.* Band 2. Leipzig: F. A. Brockhaus.

LaBrecque, J. L. & Raymond, C. A. 1985 *J. geophys. Res.* **90**, 2565–2575.

Langel, R. A. 1987 In *Geomagnetism*, vol. 1, ch. 4 (ed. J. A. Jacobs). London: Academic Press.

Langel, R. A. & Estes, R. H. 1982 *Geophys. Res. Lett.* **9**, 250–253.

Langel, R. A. & Estes, R. H. 1985 *J. geophys. Res.* **90**, 2487–2494.

Langel, R. A., Estes, R. H. & Mead, G. D. 1982 *J. Geomagn. Geoelect., Kyoto* **34**, 327–349.

Langel, R. A., Kerridge, D. J., Barraclough, D. R. & Malin, S. R. C. 1986 *J. Geomag. Geoelect., Kyoto* **38**, 573–597.

LeMouël, J-L. 1984 *Nature, Lond.* **311**, 734–735.

LeMouël, J-L., Gire, C. & Madden, T. 1985 *Phys. Earth Planet. Inter.* **39**, 270–287.

Leroux, E. (ed.) 1894 *Voyage de 'La Manche' à l'Ile Jan Mayen et au Spitzberg.* Paris.

Levere, T. H. 1986 *Ann. Sci.* **43**, 57–76.

Linklater, E. R. R. 1972 *The voyage of the Challenger.* London: John Murray.

Littlehales, G. W. 1897 *Contributions to terrestrial magnetism, the magnetic dip or inclination. As observed at thirty important maritime stations, together with an investigation of the secular change in the direction of a freely suspended magnetic needle at twenty-nine of the stations. U.S. Hydrographic Office, Pub. no.* 114. Washington, D.C.: Government Printing Office.

Lloyd, D. L. & Gubbins, D. 1989 *Geophys. Jl R. astr. Soc.* (Submitted.)

Lowes, F. J. 1974 *Geophys. Jl R. astr. Soc.* **36**, 717–730.

Lowes, F. J. 1975 *Geophys. Jl R. astr. Soc.* **42**, 637–651.

Lowes, F. J. 1985 *Phys. Earth Planet. Inter.* **37**, 25–34.

Lowes, F. J. 1987 *Geophys. Jl R. astr. Soc.* **89**, 472.

Lowes, F. J. & Martin, J. E. 1987 *Phys. Earth planet. Inter.* **48**, 183–192.

Lundquist, K. Z. 1957 Magnetic observations in Svalbard 1596–1953. *Norsk Polarinstitutt, Det Kongelige Departement for Industri og Håndverk, Skrifter no.* 110. Oslo: Fabritius & Sønners.

Malin, S. R. C. & Bullard, E. C. 1981 *Phil. Trans. R. Soc. Lond.* A**299**, 357–423.

Malin, S. R. C., Hodder, B. M. & Barraclough, D. R. 1983 In *Publicado en volumen conmemorativo 75 aniversario del Observatorio del Ebro.* Roquetes.

McConnell, A. 1980 *Geomagnetic instruments before 1900; an illustrated account of their construction and use.* London: Harriet Wynter.

Menke, W. 1984 *Geophysical data analysis: discrete inverse theory.* London: Academic Press.

Merrill, R. T. & McElhinny, M. W. 1983 *The Earth's magnetic field.* London: Academic Press.

Meyer, J., Hufen, J.-H., Sievert, M. & Hahn, A. 1983 *J. Geophys.* **52**, 71–84.

Morelli, A. & Dziewonski, A. M. 1987 *Nature, Lond.* **325**, 678–683.

Musschenbroek, P. van 1729 *Physicæexperimentales et geometricæde magnete, tuborum capillarium vitreorumque speculorum attractione, magnitudine terrae, cohærenta corporum firmorum. Dissertationes ut et epheremides meteorologie ultrajectinæ.* Leiden: Samuelem Luchtmans.

Nares, G. S. 1882 *Report on the Scientific Results of the Voyage of HMS Challenger during the years 1873–76, under the command of Captain George S. Nares RN FRS and Captain Frank Tourle Thomson RN. Prepared under the superintendence of the late Sir C. Wyville Thomson and of John Murray.* London.

Neumayer, G. 1869 *Results of the magnetic survey of the colony of Victoria, executed during the years 1858–64.* Mannheim: J. Schneider.

Neumayer, G. 1889 Über das gegenwärtig vorliegende Material für erd- und welt-magnetische Forschung. *Verhandl. d. VII. Deutschen Geographentages zu Berlin.*

Neumayer, G. 1891 Vorbemerkungen. In *Physikalische Atlas, pt. IV: Atlas des Erdmagnetismus* (ed. H. Berghaus). Gotha: Justus Perthes.

Parker, R. L. 1977 *Rev. Geophys. Space Phys.* **15**, 446–456.

Pasal'ski, P. T. 1901 *On the study of the distribution of the Earth's magnetism.* Odessa.

Perry, S. J. 1878 *Proc. R. Soc. Lond.* **27**, 1–11.

Proctor, M. R. E. & Gubbins, D. 1989 *J. Geomagn. Geoelect., Kyoto.* (Submitted.)

Roberts, P. H. & Scott, S. 1965 *J. Geomagn. Geoelect., Kyoto* **17**, 137–151.

Rucker, A. W. & Thorpe, T. E. 1890 *Phil. Trans. R. Soc. Lond.* **181**, 53–328.

Rucker, A. W. & Thorpe, T. E. 1896 *Phil. Trans. R. Soc. Lond.* **188**, 1–661.

Ryckevorsel, Dr Van 1880 *Verslag aan Zijne Excellentie den Minister van Kolonien over eene Magnetische Opneming van den Indischen Archipel, in de jaren 1874–1877 gedaan.* (*Report to his excellency the minister for the colonies on a Magnetic Survey of the Indian Archipelago, made in the years 1874–1877.*) Amsterdam: Johannes Muller (for the Royal Academy of Sciences, Amsterdam).

Ryckevorsel, Dr Van & Engelenburg, C. E. 1890 *Magnetic survey of the eastern part of Brazil.* Amsterdam: Johannes Muller (for the Royal Academy of Sciences, Amsterdam).

Ryder, C. 1895 *Meddelelser om Grønland, Den Ostgrønlandske Expedition 1891–92.* Kjøbenhavn.

Sabine, E. 1868 *Phil. Trans. R. Soc. Lond.* **158**, 371–416.

Sabine, E. 1870 *Phil. Trans. R. Soc. Lond.* **160**, 265–275.

Sabine, E. 1872 *Phil. Trans. R. Soc. Lond.* **162**, 353–433.

Sabine, E. 1875 *Phil. Trans. R. Soc. Lond.* **165**, 161–203.

Sabine, E. 1877 *Phil. Trans. R. Soc. Lond.* **167**, 461–508.

Schering, K. 1889 *Geogr. Jb.* **13**, 171–220.

Schering, K. 1891 *Geogr. Jb.* **15**, 141–164.

Schering, K. 1894 *Geogr. Jb.* **17**, 1–40.

Schering, K. 1897 *Geogr. Jb.* **20**, 3–36.

Schering, K. 1900 *Geogr. Jb.* **23**, 3–62.

Scott-Hansen 1901 Determination of Magnetic Declination by Compass. In *The Norwegian North Poland Expedition 1893–1896. Scientific results, vol. II, no. 6* (*Geelmuyden. Astronomical Observations, Part D*) (ed. Fridtjof Nansen). London: Longmans, Green & Co. (for the Fridtjof Nansen Fund for the Advancement of Science).

Shadwell, C. 1877 *Phil. Trans. R. Soc. Lond.* **167**, 138–143.

Shure, L. & Parker, R. L. 1981 *J. geophys. Res.* **86**, 11600–11608.

Shure, L., Parker, R. L. & Backus, G. E. 1982 *Phys. Earth Planet. Inter.* **28**, 215–229.

Steen, Aksel S. 1901 In *The Norwegian North Polar expedition 1893–1896. Scientific results, vol. II, no. 7. Terrestrial magnetism, general results* (ed. F. Nansen). London: Longmans, Green & Co. (for the Fridtjof Nansen Fund for the Advancement of Science).

Tanakadate, A. 1904 A Magnetic Survey of Japan reduced to the epoch 1895 and the sea level carried out by order of the Earthquake Investigation Committee. *The Journal of the College of Science, Imperial University, Japan,* vol. XIV. Japan: Tokyo.

Tarantola, A. & Valette, B. 1982 *Rev. Geophys. Space Phys.* **20**, 219–232.

Thomson, C. J. & Gubbins, D. 1982 *Geophys. Jl R. astr. Soc.* **71**, 1–36.

Tillo, A. von 1881 Ueber die geographische Vertheilung und säculäre Aenderung der Declination und Inclination im europäischen Russland. *Repertorium Für Meteorologie,* vol. 8, no. 2, pp. 1–82. St Petersburg.

Tillo, A. von 1885 Ueber die geographische Vertheilung und säculäre Aenderung der erdmagnetischen Kraft im europäischen Russland. *Repertorium Für Meteorologie,* vol. 9, no. 5, pp. 1–78. St Petersburg.

U.S. Bureau of Navigation 1886 *The variation of the compass, as determined in various parts of the World (chiefly at sea), by officers of the United States Navy, while navigators of ships, between the years 1881 and 1885.* (Naval Professional Papers: no. 19.) Washington: Government Printing Office.

U.S. Hydrographic Office 1894 *Contributions to terrestrial magnetism, the variation of the compass. From observations made in the United States Naval Service during the period from 1891 to 1894.* (Publ. no. 109.) Washington: Government Printing Office.

U.S. Hydrographic Office 1895 *Contributions to terrestrial magnetism, the variation of the compass. As observed at fifty of the principal maritime stations from the earliest times to the present, together with equations for each station, from which values may be predicted and annual rates of change found.* (Publ. no. 109a.) Washington: Government Printing Office.

Vacquier, V. 1972 *Geomagnetism in marine geology.* New York: Elsevier.

Veinberg, B. P. 1929–33 *Catalogue of Magnetic Determinations in USSR and in Adjacent Countries from 1556 to 1926,* vols I & II (1929), vol. III (1933). Leningrad: Central Geophysical Observatory.

Veinberg, B. P. 1933 *Catalogue of magnetic determinations in the polar regions* (sections I & II). Moscow: The Central Administration of the Hydro-Meteorological service of the USSR.

Veinberg, B. P. & Shibaev, V. P. 1969 *Catalogue. The results of magnetic determinations at equidistant points and epochs, 1500–1940* (ed. A. N. Pushkov). Moscow: IZMIRAN. (Canadian Department of the Secretary of State, Translation Bureau, translation no. 0031.)

Voorhies, C. V. 1986*a* *J. geophys. Res.* **91**, 12444–12466.

Voorhies, C. V. 1986*b* *Geophys. Res. Lett.* **13**, 1537–1540.

Voorhies, C. V. & Backus, G. E. 1985 *Geophys. Astrophys. Fluid Dyn.* **32**, 162–173.

Voorhies, C. V. & Benton, E. R. 1982 *Geophys. Res. Lett.* **9**, 258–261.

Wahr, J. 1987 *Geophys. Jl R. astr. Soc.* **88**, 265–276.

Weyprecht, C. 1878 *Die Magnetische Beobachtungen der Østereichisch-Ungarischen Arctischen Expedition 1872–1874. Denkschriften der Kaiserlichen Academie der Wissenschaften. Mathematische-naturwissenschaftliche Classe. Wien.* **35**, 69–292.

Whaler, K. A. 1980 *Nature, Lond.* **287**, 528–530.

Whaler, K. A. & Clarke, S. O. 1989 *Geophys. Jl R. astr. Soc.* (In the press.)

Whaler, K. A. & Gubbins, D. 1981 *Geophys. Jl R. astr. Soc.* **65**, 645–693.

Wijkander, A. 1876 Observations Magnétiques faites pendant l'expédition Arctique Suédoise en 1872–1873. *Kongl. Svenska Vetenskaps-Akademiens Handligar* **13**, no. 15, Stockholm.

Wijkander, A. 1883 Observations Magnétiques, faites pendant l'expédition de la Vega 1878–80. *Vega Expeditions Vetenskapliga Iakttagelser,* Bd II. Stockholm.

Wilhjelm, J. 1971 Ground-based geomagnetic measurements in Greenland with an account of a survey in 1965 and a general summary of observations performed since 1587. *Danish Met. Inst. Geophys.* paper R-15.

Wille, C. & Mohn, H. 1882 *Den Norske Nordhavs-Expedition 1876–1878. 2. Magnetiske Observationer* (C. Wille) vol. V. Christiania.

Yukutake, T. & Tachinaka, H. 1969 *Bull. Earthquake Res. Inst.* **47**, 65–97.

References contained in Annales Hydrographiques, 2^e série, listed chronologically

Favereau, M. 1886 Déterminations Magnétiques faites dans l'océan Indien en 1884–85, par M. Favereau, Lieutenant de Vaisseau. **8**, 445–449.

Aubry, M. 1888 Note sur les observations magnétiques faites à bord de la Minerve (1886–88) par M. Aubry, Lieutenant de Vaisseau. **10**, 290–303.

Arethuse 1888 *Arethuse* 1887–88. Resultats des mesures magnétiques effectuées. **10**, 600–625.

Pond, C. F. 1888 Océan Pacifique Nord. Californie. Observations de déclinaison magnétique, d'inclinaison et d'intensité, faites par le Lieutenant Charles F. Pond, du steamer hydrographe des États-Unis, Commander F. A. Cooke, en 1887–88. **10**, 626.

Mizon, L. 1889 Observations magnétiques recueillies à la côte Occidentale d'Afrique par M. L. Mizon, Lieutenant de Vaisseau. **11**, 36–47.

Lephay, J. 1889 Extrait des Observations magnétiques faites dans le Levant en 1885–86 par M. J. Lephay, Lieutenant de Vaisseau à bord de La Venus. **11**, 49.

Pond, C. F. 1889 Déterminations magnétiques faites sur les côtes ouest de la basse Californie par le Lieutenant Charles F. Pond, de la marine des États-Unis, à bord du navire hydrographe Ranger. (Extrait de la Notice to Mariners No. 47 de Washington, D.C. 1889.) **11**, 233.

Le Cannellier, M. 1890 Observations magnétiques faites dans différents mouillages de la Méditerranée Orientale, par M. Le Cannellier, Lieutenant de Vaisseau à bord du Cuirasse d'escadre Amiral-Baudin. **12**, 240–245.

Astromes 1890 Déterminations magnétiques effectuées en 1889 dans diverses localités du Chili par les Astronomes de l'observatoire National de Santiago. (Extrait de la Noticias hidrograficas No. 12, Santiago, 1890.) **12**, 247.

Pond, C. F. 1890 Océan Pacifique Nord. Basse Californie (côte ouest). Déterminations magnétiques faites dans la baie Ballenas et sur l'Ile Ascuncion, par le Lieutenant Charles F. Pond, à bord du navire hydrographe Ranger. (Notice to Mariners No. 50 Washington 1890.) **13**, 86.

Franz Loschober 1891 Déterminations magnétiques faites en 1889–1890, et ramenés au commencement de 1890, sur les côtes de la mer Adriatique, par le capitaine de corvette *Franz Loschober*, Directeur de l'observatoire impérial et royal de Pola. (Hydrographische Nachricht, No. 28, Pola, 1891.) **13**, 266–267.

Preston, E. D. 1891 Océan Atlantique. Déterminations magnétiques faites par M. E. D. Preston, Assistant du Coast & Geodetic Survey, pendant un voyage du navire Pensacola dans l'océan Atlantique, 1890–1891. (U.S.C. & G.S., Bull. no. 22, Washington Fevrier 1891.) **13**, 268.

Schwerer, A. 1892 Étude sur le magnétisme terrestre a Terre-Neuve, par M. A. Schwerer, Lieutenant de Vaisseau. **14**, 88–111.

de Roujou, L. 1892 Déterminations magnétiques en extreme-Orient par M. Leconte de Roujou, Lieutenant de Vaisseau à bord de la Tromphante. **14**, 112–155.

Courmes, L. 1892 Observations magnétiques faites pendant la campagne du croiseur Le Dubordieu (1889–1891), par M. L. Courmes, Lieutenant de Vaisseau. **14**, 302–349.

Mion, M. 1893 Déterminations magnétiques à la côte Ouest de Madagascar, et aux Comores, par M. Mion, Ingenieur hydrographe de la Marine. 1888–1890. **15**, 205–207.

Mottez, L. 1893 Déterminations magnétiques faites sur la côte ouest d'Amérique pendant une campagne dans l'océan Pacifique à bord du croiseur Le Dubordieu (1892–93) par M. Luis Mottez, Lieutenant de Vaisseau. **15**, 408–431.

Lancelin, G. 1894 Observations de déclinaison magnétique dans la Méditerranée orientale (Fevrier-Mai 1894) par M. G. Lancelin, Enseigne de Vaisseau à bord du Croiseur le Cosmao. **16**, 141–143.

Norvège 1895 Resultats des observations de déclinaison magnétique faites en 1893 et en 1894 sur la côte de Norvège, entre Christiania et Skolver. (Efterretninger for Sjofarende, No. 3/139, Christiania, mars 1895.) **17**, 95.

Houette, M. & Morache, M. 1896 Mission magnétique en Islande et en Scandinavie, de l'Aviso-transport la Manche, par M. Houette, Capitaine de Frégate, Commandant, et M. Morache, Lieutenant de Vaisseau à bord de ce bâtiment. **18**, 49–68.

Schwerer, A. 1896 Observations à la mer de M. Schwerer, Lieutenant de Vaisseau à bord du Dubordieu. **18**, 177–187.

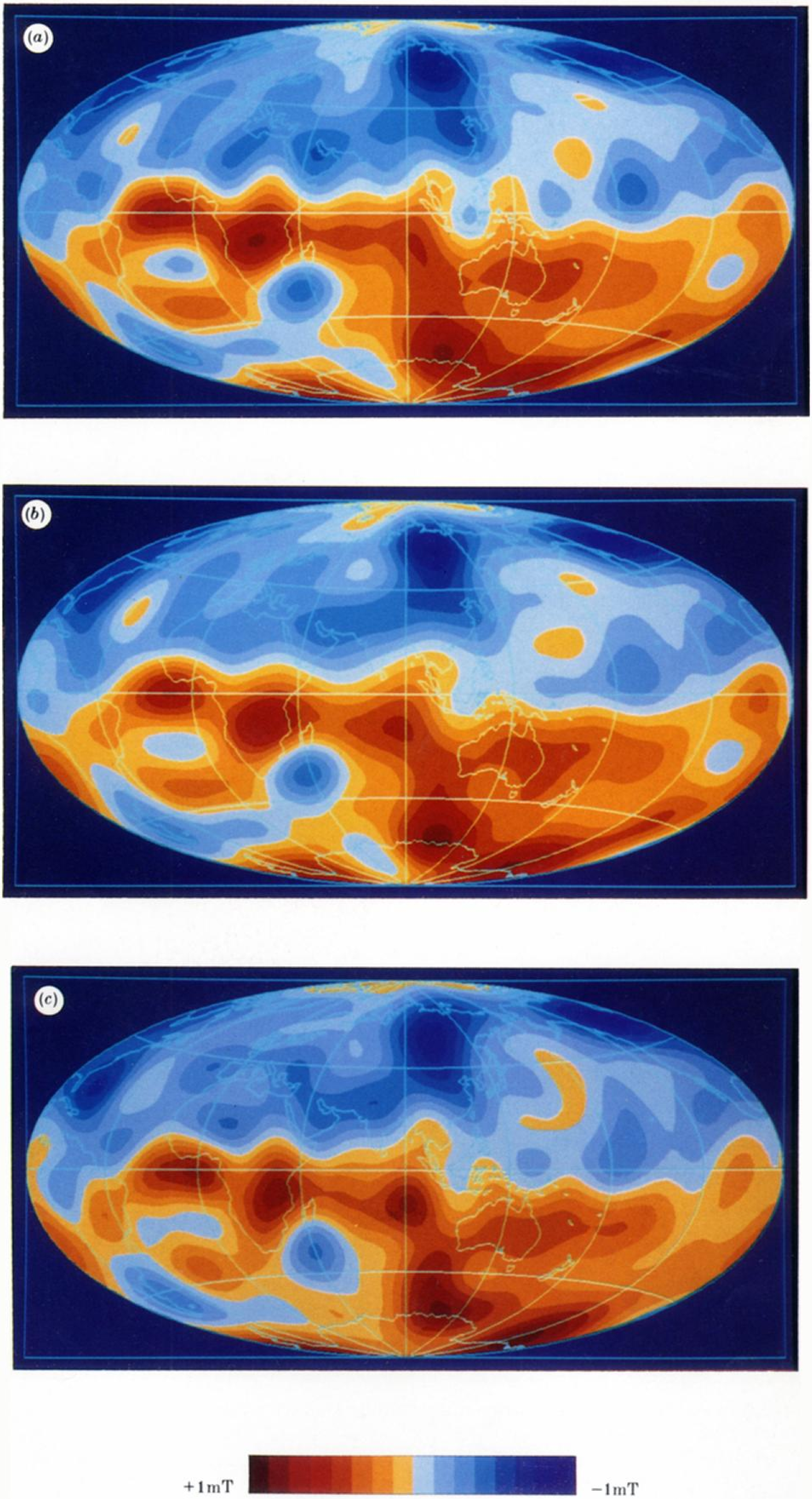

FIGURE 19. Maps of the radial component of the magnetic field at the core–mantle boundary. The orange shades represent intensity of flux out of the core, the blue shades intensity into the core. The map projection is Aitoff equal-area. (*a*) 1980.0; (*b*) 1966.0; (*c*) 1955.5; (*d*) 1945.5; (*e*) 1935.5; (*f*) 1925.5; (*g*) 1915.5; (*h*) 1905.5; (*i*) 1882.5; (*j*) 1842.5; (*k*) 1777.5; and (*l*) 1715.0.

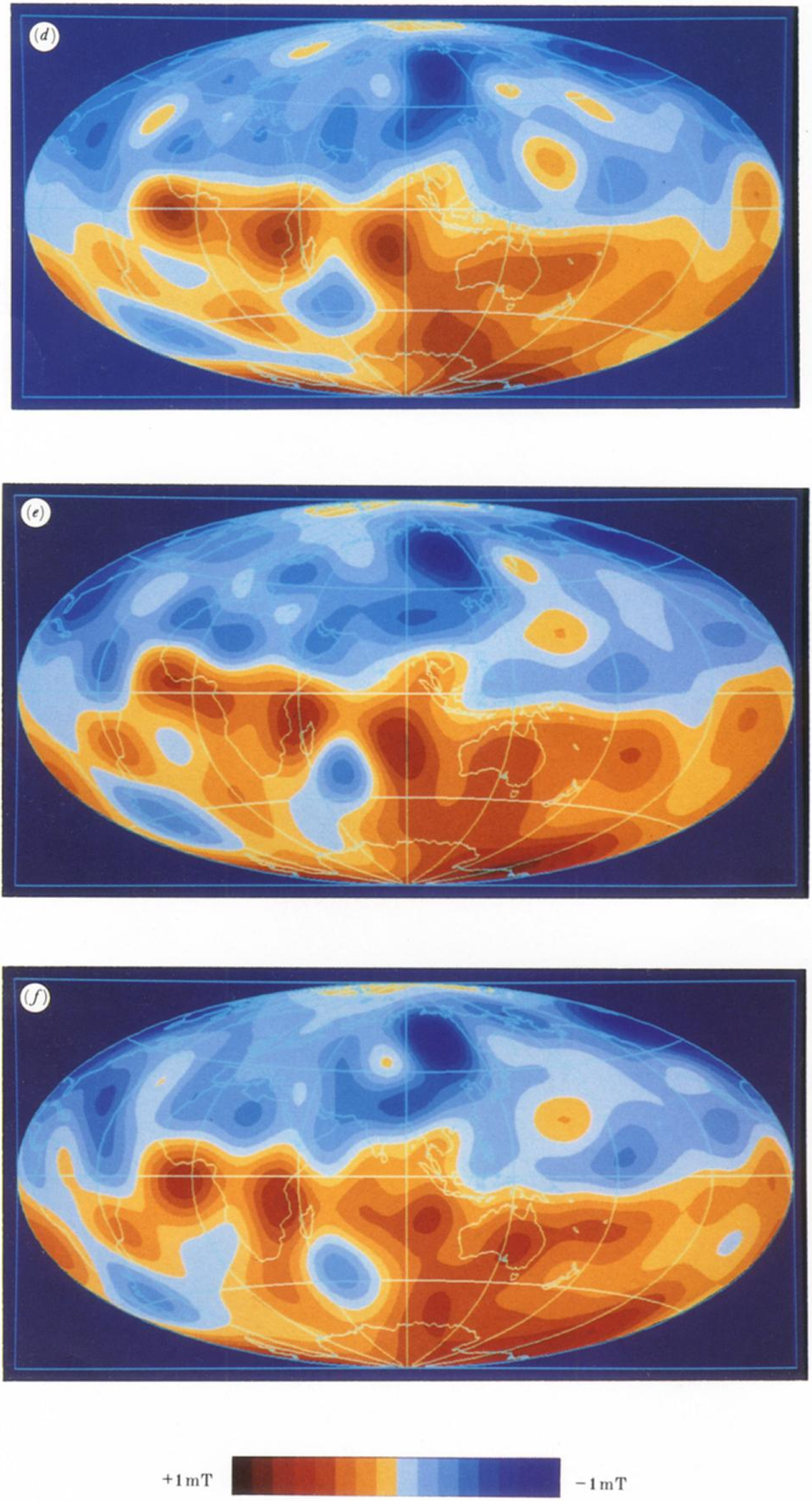
(d)
(e)
(f)
+1 mT
−1 mT

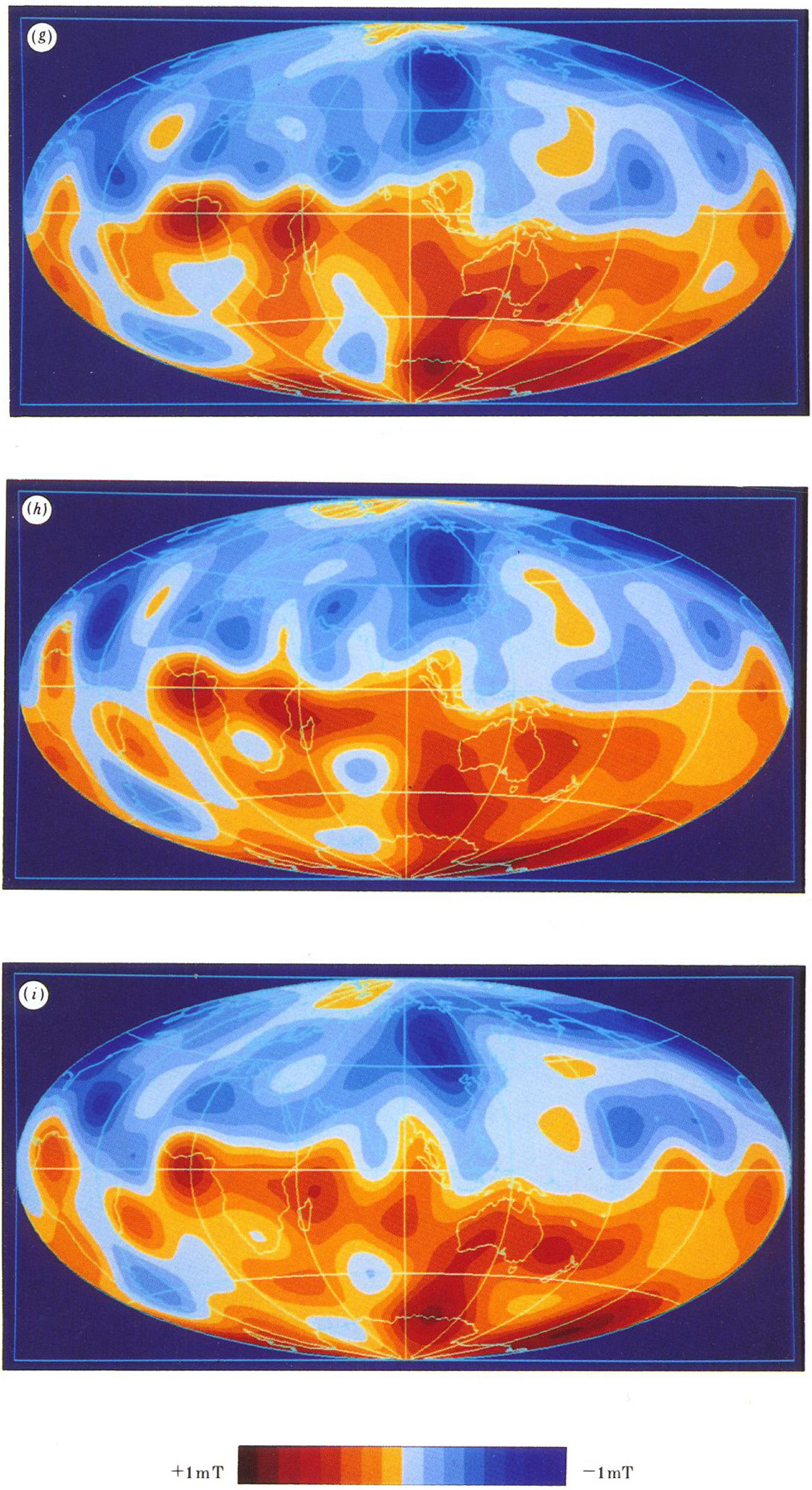

FIGURE 19 *g*, *h*, *i*. For description see facing plate 1.

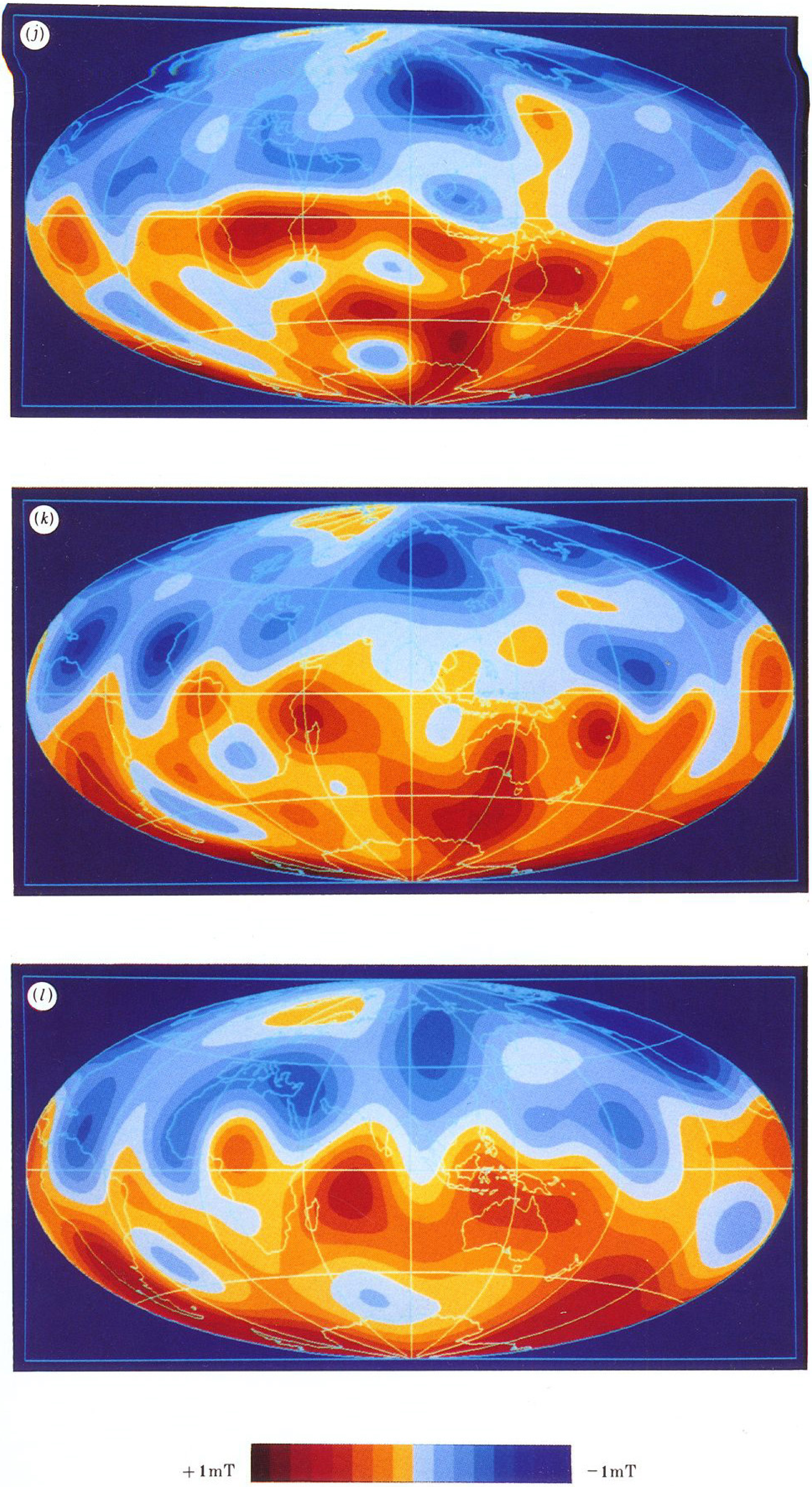

FIGURE 19 *j*, *k*, *l*. For description see facing plate 1.